



HAL
open science

Monitoring and statistical modelling of permafrost in steep slopes of Norway

Florence Magnin, Bernd Etzelmüller, Sebastian Westermann, Paula Hilger, Cristian Lussana, Ketil Isaksen, Reginald Hermanns

► **To cite this version:**

Florence Magnin, Bernd Etzelmüller, Sebastian Westermann, Paula Hilger, Cristian Lussana, et al.. Monitoring and statistical modelling of permafrost in steep slopes of Norway. 5th European Conference on Permafrost, Jun 2018, Chamonix, France. pp.172 - 182, <10.1002/ppp.1884>. <hal-03337531>

HAL Id: hal-03337531

<https://hal.science/hal-03337531v1>

Submitted on 8 Sep 2021

HAL is a multi-disciplinary open access archive for the deposit and dissemination of scientific research documents, whether they are published or not. The documents may come from teaching and research institutions in France or abroad, or from public or private research centers.

L'archive ouverte pluridisciplinaire **HAL**, est destinée au dépôt et à la diffusion de documents scientifiques de niveau recherche, publiés ou non, émanant des établissements d'enseignement et de recherche français ou étrangers, des laboratoires publics ou privés.



HAL Authorization



Monitoring and statistical modelling of permafrost in steep slopes of Norway

Florence Magnin¹
 Bernd Etzelmüller¹
 Sebastian Westermann¹
 Paula Hilger^{1,2}
 Cristian Lussana³
 Ketil Isaksen³
 Reginald Hermanns^{2,4}

¹ Department of Geosciences, University of Oslo, P.O. Box 1047, Blindern, 0316 Oslo, Norway, florence.magnin@geo.uio.no

² Geohazard and Earth Observation Group, Geological Survey of Norway, 7491 Trondheim, Norway

³ Norwegian Meteorological Institute, 0313 Oslo, Oslo, Norway

⁴ Norwegian University of Science and Technology, Trondheim, Norway

Abstract

Permafrost can become a crucial factor of steep slope stability, and knowing the distribution of permafrost in steep terrain is a prerequisite when evaluating slope stability in such areas. However, permafrost distribution in such terrain is poorly known. In this study, we present a very first effort in modelling steep slopes permafrost at the nation-scale of Norway. This study is based on a multi-years dataset of 26 rock-surface temperature measurement points covering various aspects, elevations and latitudes. These measurements allow for statistical modelling of rock surface temperature that is then used to map permafrost probability. In this presentation, we present the measurement settings, the rock surface temperature data, the modelling approach and first results of the permafrost mapping.

Keywords: Permafrost; steep slopes; Norway; statistical modelling; mapping.

Introduction

The Norwegian fjords and valleys are characterized by steep mountain flanks lying above human settlements and infrastructures, the sea or lakes. These settings are a main source of risk. The destabilizations of steep slopes endanger the human lives and activities because they can (i) directly hit houses and infrastructures, (ii) dam the valley bottom, disturbing human activities and transports, which also provokes (iii) modifications in the water streams creating new lakes susceptible to outburst, and can also (iv) hit existing water bodies and trigger displacement waves. Such mass movements and their secondary effects have caused hundreds of fatalities in the Norwegian history (Hermanns *et al.*, 2012). While geological and paraglacial processes have been extensively studied to understand steep slope destabilizations in Norway, the possible influence of permafrost has been less emphasized. However, recent studies in various mountain ranges, especially in the European Alps, have pinpointed that permafrost degradation is a major factor of steep slope stability (Gruber & Haeberli, 2007). Many unstable steep slopes lie in a possible permafrost range in Norway and an

estimation of its distribution is required as a first step to better understand its role in these destabilizations. A first map of rock wall permafrost distribution in Norway has been proposed by Steiger *et al.* (2015) based on general assumptions on the link between permafrost and air temperature. In this presentation, we present a preliminary estimation of permafrost distribution based on a statistical model fitted with 24 rock surface temperature (RST) times series and a preliminary estimation of permafrost distribution.

Methods and preliminary results

Rock surface temperature measurements

During summers 2015, 2016 and 2017, 22 RST loggers were installed along a latitudinal profile from 60°50'N to 69°46'N. They complete 4 loggers installed in 2010 in Jotunheimen (Hipp *et al.*, 2014). Measurements points cover all aspects and range from 215 to 2320 m asl.

Statistical modelling approach

In fall 2017, the available time series yield 54 mean annual rock surface temperature (MARS'T) points available for statistical modelling. Possible predictors of

MARST are determined based on multi-collinearity tests and by analyzing their statistical significance. As evidenced in other mountain ranges, mean annual air temperature (MAAT) and the potential incoming solar radiation (PISR) are the most important predictors of MARST. The statistical model is then implemented in a GIS to map permafrost probability on a 10-m-resolution DEM (released by the Norwegian Mapping Authority).

Permafrost probability mapping

Permafrost is mapped based on the 1961-1990 MAAT data released by the Norwegian Meteorological Institute (SeNorge v2; Lussana *et al.*, 2017), downscaled from 1 km to 10 m resolution using a regional lapse rate. PISR is mapped using GIS tools and assuming an atmospheric transmissivity of 100%. MARST is then mapped using the parameters of the statistical model and the permafrost probability is expressed as a probability of the MARST to be $\leq 0^{\circ}\text{C}$. The permafrost probability is classified based on standard classification with isolated (0 to 10%), sporadic (10 to 50%), discontinuous (50 to 90%) and continuous ($>90\%$) permafrost (Fig. 1).

Preliminary results

Continuous permafrost (MARST $\leq 0^{\circ}\text{C}$) is likely above 1200 m a.s.l. in North faces and above 1600 m a.s.l. in the South faces of the South-Western Norway. In Northern Norway, the lower limit of continuous permafrost rather lies at around 600 m in North faces and 900 m in South faces. This preliminary estimation already shows that many of the unstable steep slopes of Norway lie within the range of discontinuous-continuous permafrost, such as the Mannen (1294 m a.s.l.) rock slide (up to 30Mm³, depending on the scenario) in SW Norway (Fig.1).

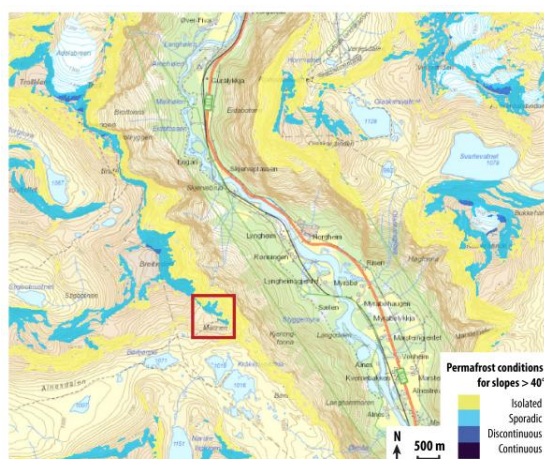


Figure 1. Example of the permafrost distribution map in the steep slopes of Romsdalen. The Mannen rock slide (red square) lies in the sporadic permafrost zone.

Outlooks

Using the 1961-1990 normal MAAT results in permafrost overestimation. The model will be also implemented with the MAAT of 1981-2010 to better represent current conditions.

The resulting MARST map can be used to setup a transient numerical model such as those from Myhra *et al.* (2015). In the frame of this project, transient models of steep slope thermal regime are coupled with mechanical models to better assess the role of permafrost in steep slope destabilization.

Acknowledgments

This study was mainly funded by the Research Council of Norway (CryoWALL - 243784/CLE), in addition to the Geological Survey of Norway (NGU) and the Department of Geosciences, University of Oslo.

References

- Gruber S. & Haeberli W., 2007. Permafrost in steep bedrock slopes and its temperature-related destabilization following climate change. *Journal of Geophysical Research: Earth Surface*, 112: F02S18.
- Hermanns, R., Hansen, L., Sletten, K., Böhme, M., Bunkholt, H.S.S., Dehls, J.F., Eilertsen, R.S., Fisher, L., L'Heureux, J.-S., Høgaas, F., Nordahl, B., Oppikofer, T., Rubensdotter, L., Solberg, I.-L., Stalsberg, K., & Yugi Molina, F.X., 2012. Systematic geological mapping for landslide understanding in the Norwegian context. In E. Eberhardt, C. Froese, A.K. Turner & S. Leroueil (eds.), *Landslide and Engineered Slopes: Protecting Society through Improved Understanding*, Taylor & Francis Group: London, 265-271.
- Hipp, T., Etzelmüller, B. & Westermann, S., 2014. Permafrost in Alpine Rock Faces from Jotunheimen and Hurrungane, Southern Norway', *Permafrost and Periglacial Processes*, 25(1): 1-13.
- Lussana, C., Tveito, O. E. & Uboldi, F. 2017. "Three-dimensional spatial interpolation of two-meter temperature over Norway", accepted for publication on the Quarterly Journal of the Royal Meteorological Society
- Myhra, K.S., Westermann, S., & Etzelmüller, B., 2015. Modelled Distribution and Temporal Evolution of Permafrost in Steep Rock Walls Along a Latitudinal Transect in Norway by CryoGrid 2D. *Permafrost and Periglacial Processes*, 28: 172-182, doi:10.1002/ppp.1884,
- Steiger, C., Etzelmüller, B., Westermann, S., & Myhra, K.S., Modelling the permafrost distribution in steep rock walls in Norway, *Norwegian Journal of Geology*, 96(4): 329-341.



Rock glaciers of the Balkan Peninsula

Brigitte Magori¹

Petru Urdea¹

¹West University of Timisoara, brigitte.magori@gmail.com

Abstract

Being one of the defining alpine features, rock glaciers are spread and studied in high mountains around the world, but the scale and level at which they are analyzed differs greatly across the continents. In the Balkan region, the research of the permafrost relates landform is at its beginnings, with a limited number of studies being conducted until now. We present an overview of the main characteristics of rock glaciers in the Balkan Peninsula based on their morphometric features and basic statistical analysis. Our results show a relation between the latitude of rock glaciers and their size and altitude, especially interesting being the fact that rock glaciers size tends to increase at lower latitudes.

Keywords: rock glaciers; permafrost; morphometric characteristics; Late Glacial; Balkan Peninsula.

Introduction

Rock glaciers (RG) are rock-mantled ice bodies widespread in the alpine environment of the Balkan Peninsula and elsewhere. Because they transport both rock and ice down-valley due to the deformation of the ice within (Haerberli, 2000) they are characterized by a distinct surface microrelief of longitudinal or transversal ridges and furrows (Barsch, 1996). These features are morphological indicators for mountain permafrost occurrence and for periglacial conditions. In the current study, we present an overview of the rock glaciers from the Balkan Peninsula by analyzing their geomorphometric characteristics and their geographic location

Until now the presence of rock glaciers has been inventoried, at a local scale, for the Rila (Gikov & Dimitrov, 2010), Pirin (Dimitrov & Gikov, 2011), Pindus (Hughes *et al.*, 2003; Palmentola & Stamatopoulos, 2006) or Dinaric Mountains (Milivojević *et al.*, 2008; Palmentola *et al.*, 1995) and has just been suggested for the Parnassus mountain range (Pechoux, 1970).

Methodology and Results

We analyzed 196 rock glaciers located in six different high mountains of the Peninsula (Table 1) spread over about three degrees of latitude. The morphometric parameters were extracted using ArcGIS from a 30m resolution DEM and the statistical analysis (correlations, t test) were performed using the software R.

Out of the total number of RGs, 149 (76%) are tongue shaped and the rest are lobate. The tongue shaped are also located at higher altitudes ($t=4.98$, $p<0.05$) and have a greater area ($t=5.05$, $p<0.05$) than the lobate RGs.

Table 1. Rock glaciers in the Balkan Peninsula

Mountains	Coordinates	Nr. of RG	Mean elevation of the RG front (m)
Prokletije	42°26'30"N 19°48'45"E	42	1992
Rila	42°06'00"N 23°33'00"E	39	2348
Korab	41°47'28"N 20°32'52"E	8	2233
Pirin	41°45'49"N 23°23'58"E	83	2339
Tymphi	39°58'54"N 20°48'54"E	8	1932
Tzoumerka	39°29'00"N 21°12'00"E	16	1748
Parnassus	38°32'09"N 22°37'27"E	1	1890

The results show that 70% of rock glaciers have a northern aspect and they are spread at altitudes between 1748-2447 m, with the highest rock glaciers situated in the Rila Mountains, Bulgaria and the lowest in Tzoumerka Mountains, Greece. The rock glaciers slope ranges from 9° to 28°, with a mean of around 17° for all the mountain ranges.

The average area is 12.4ha, with the biggest RG being in the Prokletije mountains with an area of 89.7ha.

Conclusions

The analysis of the rock glacier characteristics reveals the following conclusions:

The Tzoumerka are the southernmost mountains with a significant number of rock glaciers and have the lowest most altitude at which they form.

The results show that the size of the rock glaciers increases with the decrease of the latitude.

This overview is a necessary first step in our propose to reconstruct the permafrost conditions from the Late Glacial and Holocene in the Balkan Peninsula.

References

- Barsch, D., 1996. *Rockglaciers. Indicators for the present and former geoecology in high mountain environments*. Springer, Berlin.
- Dimitrov, P. & Gikov, A., 2011. Relict rock glaciers identification and mapping in Pirin Mountain using aerial and satellite images. *Proceeding of the Seventh Scientific Conference SPACE, ECOLOGY, SAFETY*.
- Gikov, A. & Dimitrov, P., 2010. Identification and mapping of the relict rock glaciers in the Rila Mountain using aerial and satellite images. *Proceeding of the Sixth Scientific Conference SPACE, ECOLOGY, SAFETY*.
- Haeberli, W., 2000. Modern research perspectives relating to permafrost creep and rock glaciers: a discussion. *Permafrost Periglacial Process.*, 11(4), 290-293.
- Hughes, P., Gibbard, P., Woodward, J., 2003. Relict rock glaciers as indicators of Mediterranean palaeoclimate during the Last Glacial Maximum(Late Wuermian) in northwest Greece. *J. Quat. Sci.*, 18(5), 431-440.
- Milivojević, M., Menković, L., Čalić, J., 2008. Pleistocene glacial relief of the central part of Mt. Prokletije (Albanian Alps). *Quat. Int.*, 190(1), 112-122.
- Palmentola, G., Baboci, K., Gruda, G., Zito, G., 1995. A note on rock glaciers in the Albanian Alps. *Permafrost Periglacial Process.*, 6(3), 251-257.
- Palmentola, G. & Stamatopoulos, L., 2006. Preliminary data about sporadic permafrost on Peristeri and Tzoumerka massifs (Pindos chain, Northwestern Greece). *Revista de Geomorfologie*, 8, 17-23.
- Pechoux, P., 1970. Traces of glacial action in the Mountains of Central Greece. *Revue de Géographie Alpine*, 58, 211-224.

Modelling of Ground Penetrating Radar in alpine Permafrost at Hoher Sonnblick Summit

Theresa Maierhofer¹
Matthias Steiner¹
Werner Chwatal^{1,2}
Wolfgang Schöner³
Adrian Flores-Orozco¹

¹TU Wien, Department of Geodesy and Geoinformation, Research Group Geophysics, Vienna, Austria, tm@as-m.at

²Pöyry-Infra GmbH, Salzburg, Austria

³University of Graz, Department of Geography and Regional Science, Graz, Austria

Abstract

In frame of the ATMOperm project, we conducted a series of Ground Penetrating Radar (GPR) surveys at Hoher Sonnblick Summit. The objective was to determine the internal structures and distribution of mountain permafrost and associated changes due to seasonal variations in temperature. To achieve this, 3D GPR surveys were repeated between 2015 and 2017 at different times. Besides the processing of the raw data, modelling of electrical properties for the computation of synthetic radargrams was carried out to permit a better interpretation of the observed changes in GPR results.

Keywords: Ground Penetrating Radar, synthetic modelling, monitoring

Introduction

Current permafrost research focuses on understanding the effect of atmospheric events, such as climate change in the degradation of alpine permafrost.

To better understand subsurface processes, here we present geophysical imaging results for data collected at the Hoher Sonnblick Summit. This is located in the Austrian Central Alps, 3106 m above sea level, where a permanently installed monitoring array (Fig. 1) permits the collection of electrical resistivity tomography (ERT) being a standard method in permafrost investigations (Krautblatter et al., 2008). However, ERT measurements might be limited in winter due to the low current injections taking place in surfaces covered by snow and ice. To overcome such limitation, we performed monitoring measurements with GPR, a contactless method based on the propagation of electromagnetic waves, which has been successfully applied in previous studies in permafrost environments (Hauck & Kneisel, 2008; Moorman *et al.*, 2007).

The final objective of our investigations is to obtain a 3D subsurface model of the electrical properties at the Hoher Sonnblick Summit for an improved characterization of the active layer and lithological

contacts and discontinuities (e.g., fractures). Aiming at improving the quantitative interpretation, the synthetic response was numerically modelled taking into account the resistivity distribution in the subsurface as derived from ERT monitoring data and information from supplementary geophysical surveys.

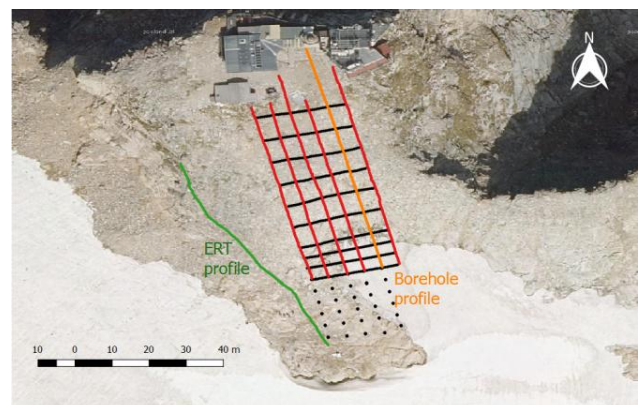


Figure 1: Orientation of the GPR profiles defined by six long profiles (red), 13 transverse profiles (black) and ERT monitoring profile (green).

Field Work

A total of eight GPR campaigns were organized between August 2015 and September 2017. In those campaigns GPR datasets were collected using a SIR 3000 unit in a common offset configuration, mainly with 200 and 400 MHz antennas. Results presented here refer to a campaign in winter 2017 collected along 6 long profiles and 13 perpendicular shorter profiles (Fig. 1) covering an area of ca. 25 x 100 m using a 200 MHz antenna.

Results

GPR raw data were analyzed using REFLEXW software, based on the application of standard filter routines and topographic correction. Results obtained for an exemplary dataset clearly reveal interfaces between materials with different electrical properties (Fig. 2). The first interpretation of the radargrams took into account amplitude information and the propagation velocity of the radar waves derived by hyperbola analysis. To validate such interpretation, we perform numerical modelling after assigning electrical values to the different materials based on GPR- and ERT-measurements and those reported in literature (Hauck & Kneisel, 2008; Moorman *et al*, 2007).

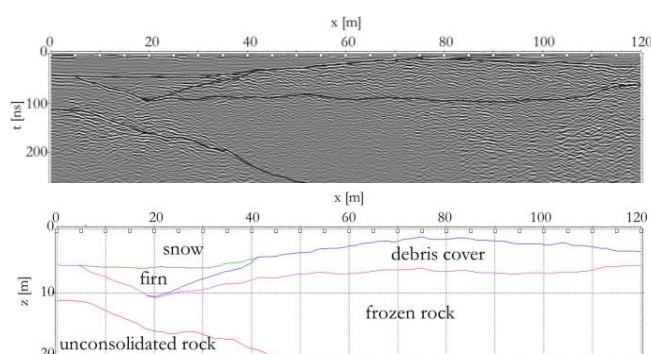


Figure 2: Radargram of borehole profile using a 200 MHz antenna (top) and corresponding interpreted model (bottom).

Since the reflection of GPR signals is related to variations in both the electrical permittivity (ϵ) and conductivity (σ) of the medium, our modelling included variations in the contrasts between those parameters and the geometry of the interfaces. Hence, the analysis of different numerical models permits us to adjust the synthetic radargram to approximate the actual measured data (Fig. 3). Fractures were added representing the debris cover to reconstruct the patterns observed in the measured data. Moreover, further structural information in the models has been obtained through results from seismic P-wave velocity information and transient electromagnetic soundings.

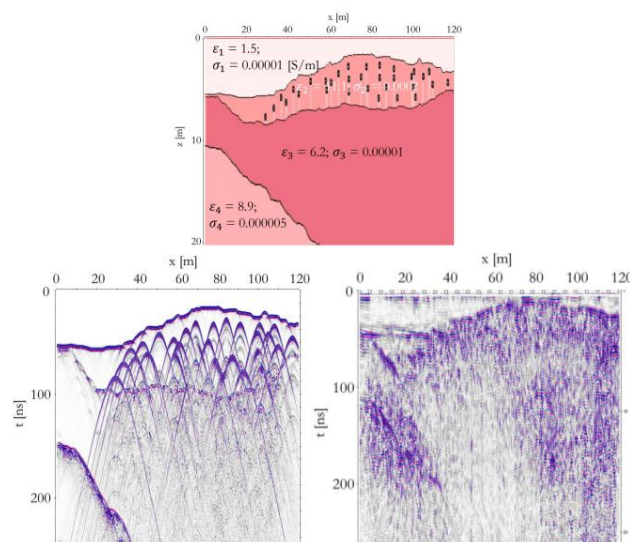


Figure 3. Comparison of synthetic (left) and measured (right) radargram representing the heterogeneous debris-covered mountain environment at the Hoher Sonnblick.

As expected due to the complexity of alpine permafrost soils, the models need to take into account the large number of discontinuities observed in the GPR data. Thus, careful data processing is required to permit the identification of the active layer and improve the quantitative meaning of the deviated electrical models. Future research will focus on the integration of borehole temperature data for the improved modelling of GPR.

Acknowledgments

The ATMOperm project is funded by the Austrian Academy of Sciences (ÖAW). We thank the team at the Sonnblick observatory for supporting this project and Stefan Reisenhofer, Martin Mayr and Jakob Gallistl for their help in the field surveys.

References

- Hauck, C., & Kneisel, C. (2008). *Applied geophysics in periglacial environments* (Vol. 240). Cambridge: Cambridge University Press.
- Krautblatter, M., Verleysdonk, S., Flores-Orozco, A., & Kemna, A. (2010). Temperature-calibrated imaging of seasonal changes in permafrost rock walls by quantitative electrical resistivity tomography (Zugspitze, German/Austrian Alps). *Journal of Geophysical Research: Earth Surface*, 115(F2).
- Moorman, B., Robinson, S., & Burgess, M. (2007). Imaging near-surface permafrost structure and characteristics with Ground-Penetrating Radar. *CSEG Recorder J*, 32(2), 23-30.

Monitoring rock glacier by optical stereoscopic “time-lapse” device

Guilhem Marsy^{1, 2, 3}

Xavier Bodin, Emmanuel Malet²

William Castaings³

Flavien Vernier, H la Hadri, Emmanuel Trouv ¹

¹ LISTIC Polytech Annecy-Chamb ry, Univ. Savoie Mont Blanc, guilhem.marsy@univ-smb.fr

² Univ. Grenoble Alpes, CNRS, Univ. Savoie Mont-Blanc, Environment Dynamics and Territories of Mountains (EDYTEM), 73000 Chamb ry, France

³ TENEVIA 38240 Meylan, France

Abstract

Classical methods to monitor rock glacier’s dynamics rely on repeated *in situ* field campaigns to evaluate the evolution of the glacier surface. Methods such as photogrammetry (structure from motion) with drone or from a set of images allow to get a dense spatial resolution, up to the pixel size, but are limited in terms of time repeatability. On the other hand, continuous GPS measurement on the glacier surface can capture seasonal changes but with a poor spatial resolution. To get both spatial and time resolution we developed an optical stereoscopic time lapse device. The system, made with two fixed reflex cameras, placed at different viewpoints and taking several images per day, is able to acquire the 3D surface of the glacier over time and thus producing time series of spatial data at high resolution in space and time (4D).

Keywords: Rock glacier kinematics; Surface displacement monitoring; Time-lapse stereo-photogrammetry.

Introduction

Rock glacier, mainly situated in dry mountains and area of discontinuous permafrost, are creeping mixtures of ice and debris (Haeberli, 1985). Due to the high thermal inertia of permafrost, the monitoring of rock glacier flow can highlight climatic trends. The Laurichard rock glacier, situated in the southern French Alps, has been studied for several decades, with the use of different methods : LiDAR surveys, repeated GPS surveys of marked blocks, geoelectric campaigns and continuous ground temperature measurements (Bodin et al, 2009). Regarding velocity surface monitoring, these methods lack of time repeatability and/or spatial resolution. On the other hand (Hadhri et al, 2017) have proposed a solution based on monoscopic time lapse imagery, to compute dense velocity surface field of slow moving surfaces, such as glacier, with high temporal resolution. We propose to extend this work by using a second camera to get velocity field in meters and not only in pixels coordinates and apply it in the Laurichard rock glacier context.

Methods

Study site

The Laurichard rock glacier is situated at an altitude between 2400 and 2700-m asl, surrounded by high rock

faces, and is 500-m long and between 80 and 200-m wide. The typical mean velocity is around 25-cm/year at the glacier roots and front, and can reach more than one meter on the median steepest part.

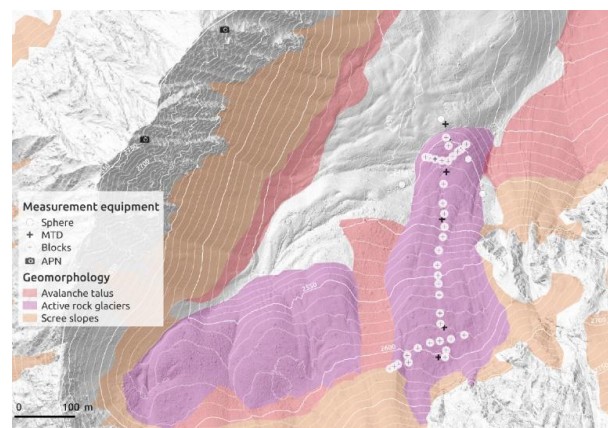


Figure 1 Field installations on the Laurichard rock glacier: cameras, spheres, marked blocks, temperature sensors.

Two Nikon D800 with a 85mm focal lens are situated 300-m away from the glacier and the baseline between the camera is 200-m. Five spheres, with a diameters of 35-cm are situated around the glacier and are used as fixed ground control points (one sphere located on the

tongue of the rock glacier). Figure 1 gives an overview of the field installations.

Data processing

The outdoor conditions are really challenging for photogrammetric measurements: fog, snow cover, cast shadows, illuminations changes, lens flare, can affect the quality of the output velocity vector field. That is why several images are taken per day to maximize the probability to have a pair of stereo images that can be further processed. The first step is to identify the best images of the day and discard the images that cannot be processed.

Even though the cameras are fixed to solid rock, unwanted shifts of the images often occur, related to the thermally-controlled differential dilatation/retraction of the various parts of the device (camera itself, lens, case...). The second step is to register all the images such that fixed ground stays still in the images, this is done estimating an homography transformation from extracted corresponding points on stable areas of the scene.

Then sparse correspondences between images taken at different dates are extracted to get velocity vector field in pixels. Figure 2 shows the extracted displacement between October 2013 and October 2016.

To convert velocities from pixels to meters vectors, the cameras need to be calibrated. The calibration is done by identifying feature points in the images with known 3D coordinates, then a nonlinear optimization algorithm estimates the intrinsic and extrinsic parameters of the cameras (Hartley and Zisserman 2003).

From this calibration, it is possible to convert a velocity vector in pixels to a vector in meter if the vector can be identified in the two stereo pair of images (Hartley and Zisserman 2003).

Further processing can be done to improve the results, such as snow detection to restrict correspondences extraction in time to snow free area.



Figure 2 Surface vector velocity field in pixels of the Laurichard rock glacier between September 2013 and September 2016.

References

- Bodin X., Thibert E., Fabre D., Ribolini A., Schoeneich P., Francou B., Reynaud L., Fort M., 2009. Two Decades of Responses (1986–2006) to Climate by the Laurichard Rock Glacier, French Alps. *Permafrost and Periglacial Processes* 20, 331–344.
- Haerberli, W., 1985. Creep of Mountain Permafrost: Internal Structure and Flow of Alpine Rock Glaciers. *Mitteilungen der VAW, ETH: Zürich*; 142 pp.
- Hadhri, H., Vernier, F., Atto, A., & Trouvé, E. (2017, June). Inverse Formulation of Temporal Closure and Proposed Solutions for Offset Tracking of Natural Scenes. In *MultiTemp 2017*.
- Hartley, Richard, and Andrew Zisserman. *Multiple view geometry in computer vision*. Cambridge university press, 2003.



Reconstruction of mean annual ground surface temperature in discontinuous permafrost region, northern Mongolia

Munkhdavaa Munkhjargal¹

Gansukh Yadamsuren²

Jambaljav Yamkin²

Lucas Menzel¹

¹ Department of Geography, Heidelberg University, Heidelberg, Germany, munkhjargal@uni-heidelberg.de

² Institute of Geography and Geoecology, Mongolian Academy of Science, Ulaanbaatar, Mongolia

Abstract

Mean annual ground surface temperature (MAGST) for 2016-2017, including complete thawing and freezing periods, has been estimated with 30m resolution to determine the spatial distribution of permafrost presence over Sugnugur valley, northern Mongolia. The key findings were; i) a north-south surface temperature difference of 3-4°C and the relationship between surface and lower air temperature decreased as elevation increased; ii) smaller surface offsets existed on rock and bare ground surfaces relative to vegetated surface types, and consistent snow-induced freezing and distinct thawing n-factors were observed; iii) MAGST was estimated with a RMSE of $\pm 1.4^\circ\text{C}$ and r^2 of 0.68 with greater errors on steep slopes; iv) wildfire severity affected the intensity of active layer lowering and altered the hydrological regime; v) micro-climate, topographic factors and surface characteristic influenced the presence of permafrost. These findings suggest that the stability of permafrost in this region is very vulnerable to global warming and fire-induced effects.

Keywords: discontinuous permafrost, surface temperature, air temperature, potential radiation, wildfire

Introduction

The study area is located in a semi-arid Siberian discontinuous permafrost region with -1°C of mean annual air temperature (MAAT) and has rough topography. The seasonal relations between air (T_a) and surface (T_s) temperatures based on in situ measurements and empirically projected MAAT from potential solar radiation (PSR) were considered as the driving parameters for the estimation. The results indicate that the approximation of MAAT might be derived from PSR using least linear regression analyses (with $R^2=0.98$) after several adjustments (Fig. 1). Relative consistent snow-insulated freezing n-factor n_F of about 0.5 at different altitudes including mountain top was observed, while thawing n-factor n_T notably varies, ranging from 0.8-1.2 depending on surface characteristics (Table 1).

Table 1. The observed surface offset and n-factors

Sites	SO	n_F	n_T	SD (cm)	Surface characteristic
Xoxoo	4	0.52	1.2	24	Short grassland
Eislager	3.5	0.6	1.05	20	Poorly vegetated
Bärental	4	0.53	1.16	25	Short grassland
Mtn. top	1.5	0.52	0.8	NA	Rock surface

SO, n_F , n_T and SD denote surface offset, freezing n-factor, thawing n-factor and snow depth, respectively

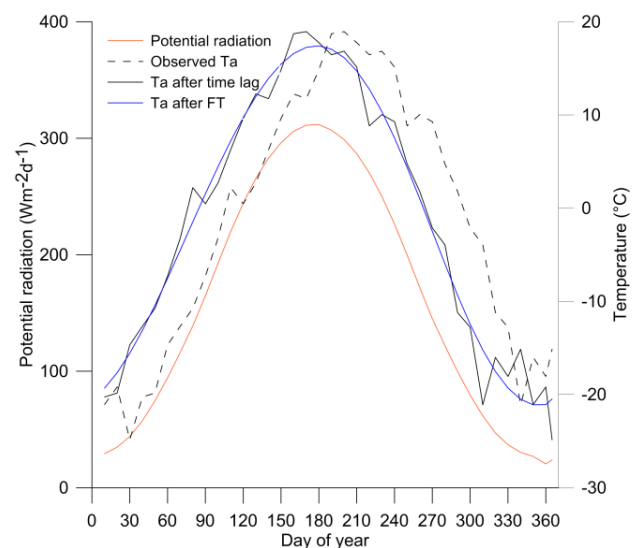


Figure 1. The distribution curves of daily mean PSR, observed and adjusted air temperatures at Bärental site on 10 day running averages. Fourier transform (FT) and 30-day time lag adjustments were applied to remove time variances

The vegetation and snow covers were observed using remote sensing images and during field campaigns. South-facing slopes were observed to be 3-4°C warmer than north-facing slopes on annual average and were mostly snow free due to high sublimation and

prevailing winds. No winter precipitation gradient has been observed and the depth of snow cover on north-facing slopes and the valley bottom were similar except for the relative thin snow cover under dense forest. The winter freezing degree-days (FDD) in surface temperature were similar on both slopes, showing rapid decrease and increase on snow-free south-facing slopes compared to north-facing slopes and bottom of the valley with thick snow cover as well. In contrast, thawing degree-days (TDD) correlated to the impact of vegetation cover and ambient air temperature during summer months play a notable role in the spatial distribution of MAGST. The correlation coefficient between T_a and T_s decreased as elevation increased, which could be explained by extended snow cover. The MAGST is initially warmer than MAAT, with surface offsets ranging from +1.5°C on rock surface to +4°C on short grasslands. Surface temperature at 5cm depth and snow depth measurements at our permanent meteorological station (since 2012) in the lower part of the valley reveal that MAGST in 2016-2017 was about 2°C warmer than the average value of previous years (Table 2).

Table 2. Mean and max snow depth (cm) with air and surface temperatures (T_a and T_s , °C) and incoming solar radiation (ISR, Wm^{-2}) in winters since 2012.

	2012/13	2013/14	2014/15	2015/16	2016/17
Mean	0.25	0.19	0.12	0.15	0.19
Max	0.41	0.26	0.25	0.26	0.29
T_s	-12.3	-10.9	-12.3	-11	-9.8
T_a	-23.7	-19.7	-18.5	-21.2	-18.7
ISR	78.8	88.8	83.5	79.6	86.9

It was caused by the occurrence of hot and dry summer 2017 (not shown here) and relative thick snow cover during winter 2016/17, leading to warmer mean surface temperature.

This may have led to 1-2°C warmer MAGST in the study region during the investigated period. The RMSE of the estimated MAGST (Fig. 3) was $\pm 1.4^\circ C$, with greater anomaly on north-facing slopes due to low PSR allocation. Additionally, the impacts of wildfire in the active layer were discussed based on soil temperature and moisture data recorded in three boreholes under severely burned, partly burned and unburned forests. The preliminary analysis indicate that the recent wildfire has altered both the hydrological and

temperature regimes (Fig. 2) of the active layer significantly, leading to increase in active layer thickness and potential permafrost degradation in this semi-arid climate.

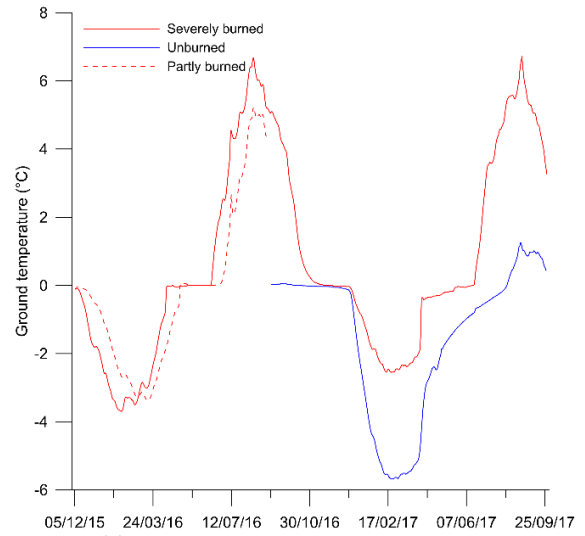


Figure 2. Temperature variabilities at 100cm depth in severely burned, partly burned and unburned forests. The fire intensity affects the magnitude of seasonal thaw depth.

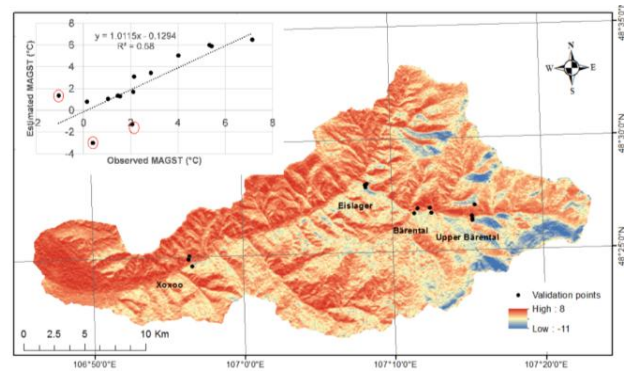


Figure 3. Estimated surface temperature in Sugnugur valley for 2016-2017. Red circles in the upper-left figure show the outliers with greater standard error. Black dots represent the locations of the validation site.

The further investigations will focus on the relationship between air and surface temperatures on different slopes including various exposures and below forest canopy to improve the accuracy of the estimation.



Seasonal and inter-annual variability of soil moisture in permafrost terrains

Cécile Pellet¹
Coline Mollaret¹
Christian Hauck¹

¹Department of Geosciences, University of Fribourg, Switzerland, cecile.pellet@unifr.ch

Abstract

Soil moisture is a key factor controlling the energy and mass exchange processes at the soil-atmosphere interface. In permanently frozen ground it strongly affects the thermal behavior of the ground by influencing its physical properties such as ice content, thermal conductivity and heat capacity. Using a unique combination of long-term borehole temperatures, meteorological data and geophysical datasets, we characterize the seasonal and inter-annual variability of soil moisture at three alpine permafrost sites. Seasonally, the evolution of soil moisture can be distinguished into three stages consistent with temperature and electrical resistivity.

Keywords: Soil moisture; Mountain permafrost, Geophysics

Introduction

Soil moisture is a key factor influencing the energy and mass exchange processes at the soil-atmosphere interface. In frost-affected terrains, soil moisture is of particular relevance given its impact on the physical properties of the subsurface such as the thermal and hydraulic conductivity as well as the ice content, the heat capacity or the electrical conductivity. Several modelling studies confirmed the influence of soil moisture on the thermal regime of frozen ground (e.g. Boike *et al.*, 2008; Hinkel *et al.*, 2001; Scherler *et al.*, 2010). However, measurement-based studies are lacking due to the scarcity of operational soil moisture monitoring stations at high elevation.

In a first attempt to assess the role of water content on the thermal regime of the ground in mountainous terrains, a soil moisture monitoring network has been established in 2013 along an altitudinal gradient spanning from middle to high elevation in Switzerland (SOMOMOUNT network see Pellet & Hauck, 2017). Two stations have been installed in collaboration with the Swiss permafrost monitoring network PERMOS in the vicinity of well-established long-term permafrost monitoring sites: Schilthorn (Hilbich *et al.*, 2011) and Stockhorn (Gruber *et al.*, 2004). Similar datasets are also available in the Italian Alps at the Cime Bianche monitoring site (Pogliotti *et al.*, 2015).

Using this unique combination of data, this contribution aims at 1) quantifying and characterizing the seasonal and inter-annual variations of soil moisture in mountain permafrost terrain and 2) comparing these

variations with measured in-situ ground temperatures, meteorological data and geophysical datasets.

Table 1. Summary of all the data available at each site.

	Schilthorn	Cervinia	Stockhorn
Soil moisture	2007-2017	2007-2017	2014-2017
Borehole temperature	1999-2017	2006-2017	2000-2017
Meteorological data	1999-2017	2006-2017	2002-2017
Geophysics (ERT)	1999-2017	2013-2017	2005-2017

Methodology and Results

The datasets available at Schilthorn, Stockhorn and Cervinia (see Tab.1) constitute state of the art measurements in mountain permafrost areas and have been used to analyze the thermal state and evolution of permafrost in several studies (e.g. Hilbich *et al.*, 2011; PERMOS, 2016; Pogliotti *et al.*, 2015). In addition, operational soil moisture measurements have been initiated at Schilthorn and Cervinia in 2007 and at Stockhorn in 2014.

Seasonally, liquid soil moisture (LSM) exhibits variations consistent with the measured temperatures and resistivity at comparable depth (Fig.1). Three typical stages can be identified: the frozen stage (lowest LSM and temperatures, smallest variability), the zero-curtain period (temperatures constant near the freezing point and marked LSM increase as well as resistivity decrease) and the unfrozen stage (high LSM and temperature variability controlled by meteorological forcing). This evolution is observed at the three field sites with

differences in onsets and duration of the stages due to site specific factors.

In addition to being spatially highly variable, the LSM evolution is also temporally variable. Thus, the inter-annual variation of LSM during the summer was analyzed and related to the meteorological conditions, ground temperature and resistivity. The two contrasting years 2014 (wet) and 2015 (warm-dry) have been especially analyzed to understand LSM behavior under very different atmospheric forcing.

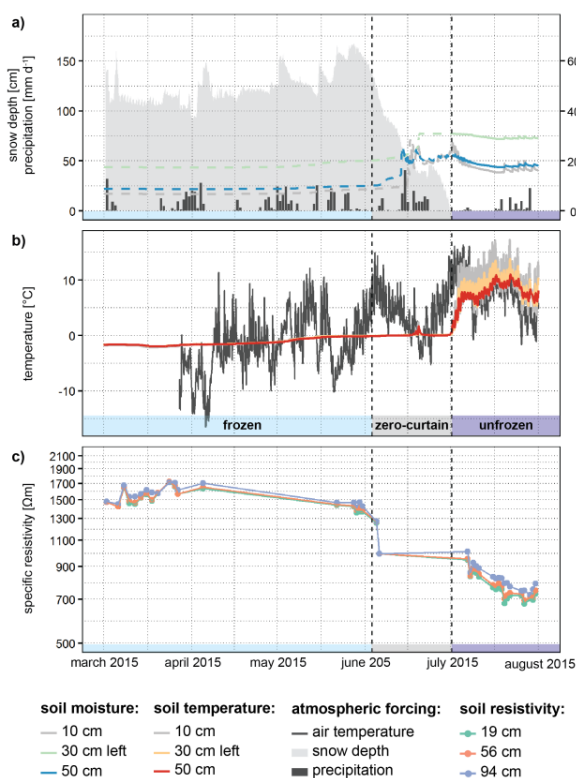


Figure 1. Temporal evolution of near surface liquid soil moisture (a), soil temperature (b) and soil resistivity (c) at Schilthorn. Air temperature, precipitation sum and snow depth are also displayed as well as the thermal state of the ground. (Figure adapted from Pellet & Hauck, 2017)

Acknowledgments

The soil moisture data at Schilthorn and Stockhorn have been collected within the SOMOMOUNT project funded by the Swiss National Science Foundation (project no. 143325). The geophysical data at Cervinia are the fruit of the collaboration between the University of Fribourg and the regional environmental protection agency of Val d'Aosta (ARPA). We also thank our colleagues from ARPA for providing the monitoring data from the Cervinia field site and the PERMOS

network for the data collected within this network at Schilthorn and Stockhorn.

References

- Boike, J., Wille, C. & Abnizova, A., 2008. Climatology and Summer Energy and Water Balance of Polygonal Tundra in the Lena River Delta, Siberia *Journal of Geophysical Research-Biogeosciences* 113:G03025.
- Gruber, S., King, L., Kohl, T., Herz, T., Haeberli, W. & Hoelzle, M., 2004. Interpretation of Geothermal Profiles Perturbed by Topography: The Alpine Permafrost Boreholes at Stockhorn Plateau, Switzerland *Permafrost and Periglacial Processes* 15:349–57.
- Hilbich, C., Fuss, C. & Hauck, C., 2011. Automated Time-Lapse ERT for Improved Process Analysis and Monitoring of Frozen Ground *Permafrost and Periglacial Processes* 22:306–19.
- Hinkel, K. M., Paetzold, F., Nelson, F. E. & Bockheim, J. G., 2001. Patterns of Soil Temperature and Moisture in the Active Layer and Upper Permafrost at Barrow, Alaska: 1993-1999 *Global and Planetary Change* 29: 293–309.
- Scherler, M., Hauck, C., Hoelzle, M., Staehli, M. & Voelzsch, I., 2010. Meltwater Infiltration into the Frozen Active Layer at an Alpine Permafrost Site *Permafrost and Periglacial Processes* 21:325–34.
- Pellet, C. & Hauck, C., 2017. Monitoring Soil Moisture from Middle to High Elevation in Switzerland: Set-up and First Results from the SOMOMOUNT Network *Hydrology and Earth System Sciences* 21:3199–3220.
- PERMOS, 2016. Permafrost in Switzerland 2010/2011 to 2013/2014 *Glaciological Report (Permafrost) of the Cryospheric Commission of the Swiss Academy of Sciences* 12-15.
- Pogliotti, P., Guglielmin, M., Cremonese, E., Morra di Cella, U., Filippa, G., Pellet, C. & Hauck, C., 2015. Warming Permafrost and Active Layer Variability at Cime Bianche, Western European Alps *The Cryosphere* 9:647–661.

Preliminary assessment for mountain frozen ground distribution (33°S, 70°W)

Ruiz Pereira, S.¹, Fernandez, H.^{1,2}, Moskalenko, F.³, García, J.L.¹, Marquardt, C.⁴, Lambert, F.¹

¹Geography Institute, Pontifical Catholic University of Chile, spruiz@uc.cl

²Christian Humanism Academy, Santiago de Chile. ³Pontifical Catholic University of Chile

⁴Department of Mining Engineering and Geosciences group, Pontifical Catholic University of Chile

Abstract

Semi-arid (27-32°S) Andean range possesses a wide variety of cryoforms, which are slightly assessed in terms of their impact relative to human access to water. 33°S and southwards, the ratio of covered/uncovered glaciers decreases. Glacierized sub-catchments of the Aconcagua basin, Juncal Norte (terminus at 3000m ASL) and Alto Del Plomo/Monos de Agua (terminus at 3800m ASL), have not been assessed in terms of their recent process dynamic. To approach this gap, sub-catchments were analyzed by remote and direct observations. Relict cryoforms (such as ice-cored moraines) coexist with preserved ones as result of differential ablation and hence the onset of paraglacial dynamic.

Keywords: Mountain frozen ground; glacier; ice-cored moraine; Andes.

Introduction

A knowledge gap where process spatial distribution is crucial to integrate catchment runoff (Pellicciotti et al., 2014) in areas where permafrost types remain present in the most arid conditions (García et al., 2017), difficult to assess because of some varying relative contributions (Rodríguez et al., 2016). Differential landscape evolution between two deglaciated areas might account on paraglacial transition processes therein.

Methods

Study area is Juncal-Norte Glacier (JNG, Fig. 1), calculated ELA at 4,500m ASL (Ayala et al., 2017), and

Monos de Agua (Fig. 2) sub-catchments. Satellite imagery (Landsat 1-8) and field mapping were utilized to assess cryoforms.

Results

The present retreat at JNG does not resemble the paraglacial evolution at Monos de Agua (MAG). Nevertheless, in between them, isolated ice-bodies and covered-glaciers were attested (Fig.1 a & b).

Ice-cored lateral moraines should persist in both settings while facing south/south-west. While moraine at JNG (Fig. 1.a) ranges from clasts to boulders, in MAG has lower sizes, and thermokarst lakes (Fig. 2) on surface.

a

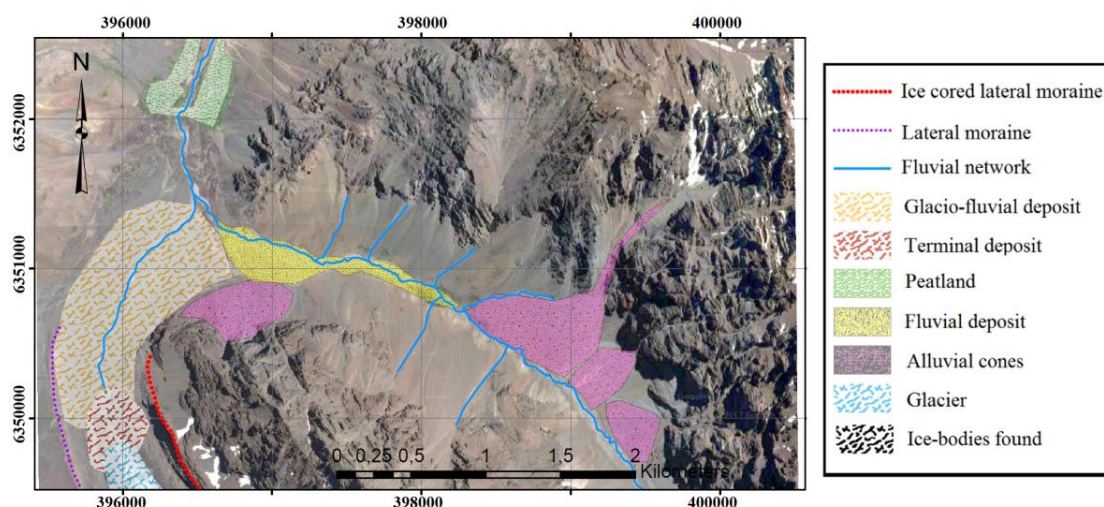


(Figure continues)

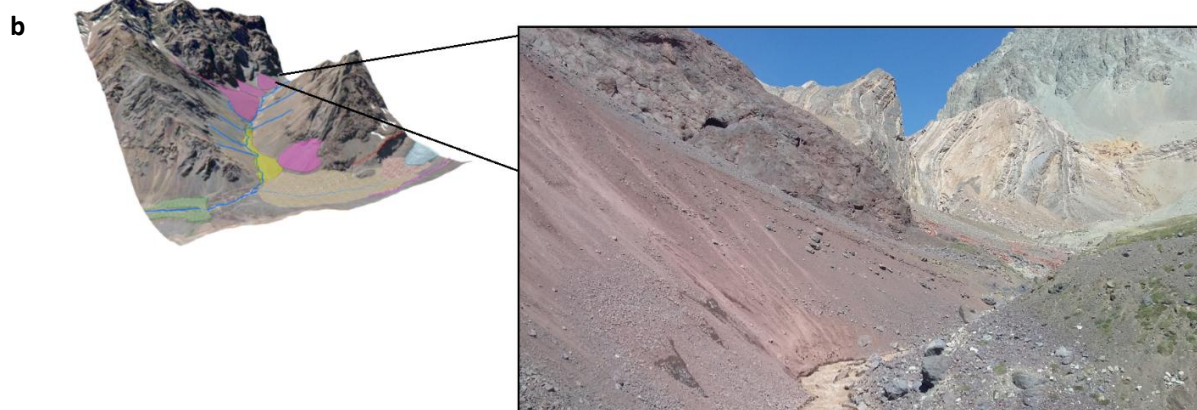


Figure 1. Monos de Agua sub-catchment, 3000-3300m ASL. Altitude in (a) increasing eastwards. Glacier in lower-left corner is Juncal Norte. Zoom in (b) shows ice-containing elements in late warm season 2016.

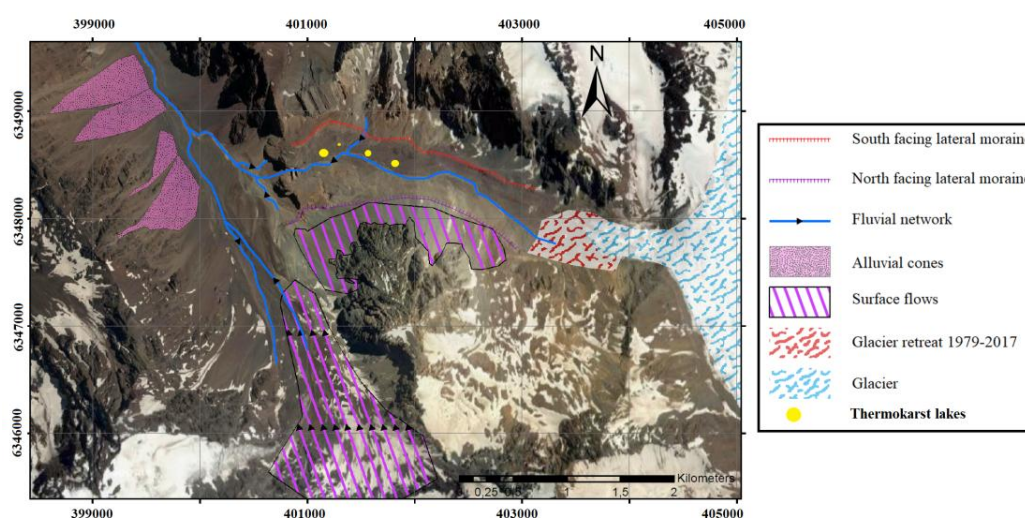


Figure 2. Monos de Agua sub-catchment, 3300-4000m ASL. Easternmost border (with Argentina) at 4000m ASL. Glacier Alto del Plomo's terminus falling westwards & Monos de Agua falling southwards.

In the case of MAG a likely persistent kilometric ice cored lateral moraine, a process assumed to occur between 1979-1989 from L1 & L4 images. Coalescent, now paraglacial taluses on the south-facing lateral moraine (Fig. 2) are considered of protalus-rampart origin and non-embryonal rock-glaciers due their steep slope and southward exposition. Fig. 2 also shows in the lower-center a distinctive gelifluction form with color-differentiated gullies running downslope over 1 mile.

Conclusions

Cryoforms between both catchments outline dominating factors of deglaciation processes and landscape transition at the central Chilean Andes.

Although deglaciation obeys contemporary climate, comparison of sediments cover thicknesses and hydrological processes would allow determining main variables in the proglacial and later paraglacial process.

References

- Ayala, A., Pellicciotti, F., Peleg, N., & Burlando, P. (2017). Melt and surface sublimation across a glacier in a dry environment: distributed energy-balance modelling of Juncal Norte Glacier, Chile. *Journal of Glaciology*, 63(241), 803-822.
- Pellicciotti, F., Ragetti, S., Carenzo, M., & McPhee, J. (2014). Changes of glaciers in the Andes of Chile and priorities for future work. *Science of the Total Environment*, 493, 1197-1210.
- Rodriguez, M., Ohlanders, N., Pellicciotti, F., Williams, M. W., & McPhee, J. (2016). Estimating runoff from a glacierized catchment using natural tracers in the semi-arid Andes cordillera. *Hydrological Processes*, 30(20), 3609-3626.



Quantifying erosion rates of steep bedrock hillslopes in glacial landscapes with cosmogenic nuclides – A case study from the Chhota Shigri Glacier, India

Dirk Scherler¹
David L. Egholm²

¹ GFZ German Research Centre for Geosciences, Telegrafenberg, D-14473 Potsdam, Germany, scherler@gfz-potsdam.de

² Department of Geoscience, Aarhus University, 8000 Aarhus, Denmark, david@geo.au.dk

Abstract

How fast do steep bedrock hillslopes in glacial landscapes erode? And how sensitive are erosion rates in these environments to temperature changes? These are fundamental questions related to past and present climate change, but they are difficult to answer. Here, we present erosion rate estimates from steep bedrock hillslopes above the Chhota Shigri Glacier, Indian Himalaya. Our estimates are based on the ¹⁰Be inventory of debris that is exposed in medial moraines. Results suggest rock wall retreat rates of ~0.6-1.3 mm yr⁻¹. We find a relatively consistent pattern of increasing ¹⁰Be concentrations (decreasing erosion rates) downglacier, which cannot be explained by ice-surface residence alone. We use a numerical ice flow model that includes debris production and transport to assess potential explanations for the observed trend. Preliminary results yield a modeled glacier that reasonably reproduces observed patterns of debris exposure.

Keywords: supraglacial debris, cosmogenic nuclides, erosion rates, frost cracking, debris-covered glaciers

Introduction

Debris-covered glaciers are widespread in the Himalaya and other steep mountain ranges. They testify to active erosion of ice-free bedrock hillslopes that tower above valley glaciers, sometimes more than a kilometer high. It is well known that supraglacial debris cover significantly reduces surface ablation rates and thereby influences glacial mass balances and runoff. However, the dynamic evolution of debris cover, along with climatic and topographic changes, is poorly understood. Here, we present ice-free hillslope erosion rates from the catchment of the Chhota Shigri Glacier, Indian Himalaya. We follow the approach of Ward and Anderson (2010), and use an ablation-dominated medial moraine as a sampler for ¹⁰Be-derived erosion rates of glacier valley walls. We combine our empirical, field-based approach with a numerical model of frost-related sediment production and glacial debris transport to (1) assess patterns of ice-free hillslope erosion that are permissible with observed patterns of debris cover, and (2) explore the coupled response of glaciers and ice-free hillslopes to climatic changes.

Study area

The Chhota Shigri Glacier is located in the North Indian state of Himachal Pradesh, in a small basin that drains into the Chandra River. The northerly oriented glacier has a length of ~9 km, covers an area of 15.7 km², and ranges from ~4200 m to ~6100 m elevation.

The medial moraine currently originates at the base of a bedrock ridge that protrudes above the surrounding ice. Its width increases from ~5 m near the junction of the two main branches of the glacier to several 10s of meters closer to the glacier terminus.

Results

¹⁰Be concentrations and erosion rates

We collected five samples from the medial moraine of the Chhota Shigri Glacier between 4638 m and 4773 m elevation. The sample locations are separated by approximately 500 m along the glacier. All samples consist of an amalgamation of >1000 surface clasts with grain sizes between ~1 and ~30 mm, yielding samples of ~5 kg weight. The clasts were randomly taken from surface patches of approximately 5 m by 5 m, which were centered on the medial moraine. Measured ¹⁰Be

concentrations increase downglacier from $\sim 3 \times 10^4$ to $\sim 6 \times 10^4$ atoms (g quartz)⁻¹ yielding hillslope erosion rates of ~ 1.3 - 0.6 mm yr⁻¹.

Numerical modeling

We used the ¹⁰Be-derived hillslope erosion rates to define a debris supply rate of 1 mm yr⁻¹ from ice-free bedrock hillslopes in the numerical ice and landscape evolution model iSOSIA (Egholm *et al.*, 2011). Based on available mass balance and ice thickness data, the calibrated model reproduces the medial moraine of the Chhota Shogri Glacier quite well, although uncertainties exist due to the transient disequilibrium of the glacier, i.e., the current debris cover was fed into the glacier during the Little Ice Age (LIA), and thus under different boundary conditions.

Discussion & Conclusions

The accumulation of ¹⁰Be during debris residence on the ice surface can only account for a small fraction (<20%) of the downglacier increase. Other potential explanations include heterogeneous source areas with different average production rates and/or erosion rates, and temporally variable erosion rates. We currently perform transient experiments during warming and cooling periods for testing models of frost-related and temperature-sensitive debris production, and for assessing the coupled sensitivity of hillslopes and glaciers to climate change.

Acknowledgments

We thank J. Mey for help during fieldwork and P. Eugster for helping in the lab.

References

Egholm, D.L., Knudsen, M.F., Clark, C.D., Lesemann, J. E., 2011. Modeling the flow of glaciers in steep terrains: The integrated second-order shallow ice approximation (iSOSIA). *J. Geophys. Res.* 116: F02012, doi: 10.1029/2010JF001900, 2011

Ward, D.J. & Anderson, R.S., 2010. The use of ablation-dominated medial moraines as samplers for ¹⁰Be-derived erosion rates of glacier valley walls, Kichatna Mountains, AK. *Earth Surface Processes and Landforms* 36: 495-512, doi: 10.1002/esp.2068.



Present and future runoff regimes at Murtèl-Corvatsch rockglacier

Martin Scherler ¹
 Martin Hoelzle ¹
 Matthias Huss ^{1,2}
 Christian Hauck ¹

¹*Department of Geosciences, University of Fribourg, Fribourg, Switzerland, martin.scherler@unifr.ch*

²*Laboratory of Hydraulics, Hydrology and Glaciology (VAW), ETH Zurich, Zurich, Switzerland*

Abstract

As glaciers are expected to continue to retreat during the 21st century due to climate change, an important source of water will be diminishing, especially during the summer months. Hence, other sources of water, such as meltwater from permafrost, will become more important to the runoff regime and the total runoff. This study aims at modelling the melt of ground ice in permafrost bodies with regard to total runoff from a small hydrological basin. We compare the results of two different models for simulating the hydrologic behavior of Murtèl-Corvatsch rockglacier from 1991 to 2100. One model is a physically based 1D heat and mass transfer model (COUP), the other a spatially distributed glacio-hydrological model (GERM). We present the simulated runoff regimes of both models for the periods 1991-2020 and 2061-2090. Significant differences of the contributions of the different reservoirs to runoff are identified and discussed.

Keywords: rockglaciers, runoff, modelling, permafrost evolution.

Introduction

As glaciers are expected to retreat substantially during the 21st century due to a warming climate, an important source of water will be diminishing, especially during the summer months. In turn, water from other sources such as permafrost will become more important in the runoff regime. This water might serve as a valuable fresh water source for agricultural needs, hydropower production or direct human consumption in mountain areas. Therefore, it is of great interest to know the origin and the amount of runoff coming from rockglaciers and slopes underlain by permafrost.

This study investigates the amount of fresh water available on a sustainable basis from such regions. In case of a disequilibrium of summer melt and winter refreezing there will be a constant or even accelerated loss of ice volume stored in permafrost and a peak in runoff. Two different models are used to gain insight into these processes. The models are applied to the well-studied site of the Murtèl-Corvatsch rockglacier in the Upper Engadin, Switzerland. The ice-rich rockglacier reaches from 2850 to 2620 m a.s.l. and is 400 m long and 200 m wide, facing north-northwest. The Murtèl study site has been the subject of numerous studies including borehole logging, energy balance measurements, geophysical surveys and numerical modelling in the past (Mittaz *et al.*, 2000, Vonder Mühll

& Haerberli, 1990). It is also part of the PERMOS monitoring network (PERMOS, 2016).

Methodology and Results

Methods

We compare the results of two different models for simulating the hydrological behavior of Murtèl-Corvatsch rockglacier from 1991 to 2100. On the one hand, we use a physically based 1D heat and mass transfer model (Coup Model; Jansson & Karlberg, 2011), on the other hand a spatially distributed highly parameterized glacio-hydrological model (GERM; Huss *et al.*, 2011). Both models account for the conductive and latent heat exchange between the atmosphere and the sub-surface and are able to resolve the mass balance of ground ice. We present the simulated runoff regimes of both models for the periods 1991-2020 and 2061-2090. The contributions of the different runoff components are presented for both models. The models are driven by climate scenario data (ENSEMBLES; MPI).

Results

The results of the models are shown in Figures 1 and 2. In the case of GERM, the runoff components are derived directly from the different water reservoirs in the model. In COUP, the components have to be calculated from the model results of all model layers.

Comparing the water fluxes computed by the two models it can be noted that the total runoff according to COUP is significantly higher during spring for both the present and the future periods. The runoff regimes in the period 1991-2020 are characterized by a snowmelt-induced peak a constant decrease until December. In the future period (2061-2090), a period of lower constant runoff is projected by both models lasting from July through to October. The contribution of permafrost storage change is significantly higher than in the present-day situation in both models. Following GERM mass gain can be expected in spring and a continuous mass release in late summer and autumn. COUP projects ice mass losses in all months except in April and September.

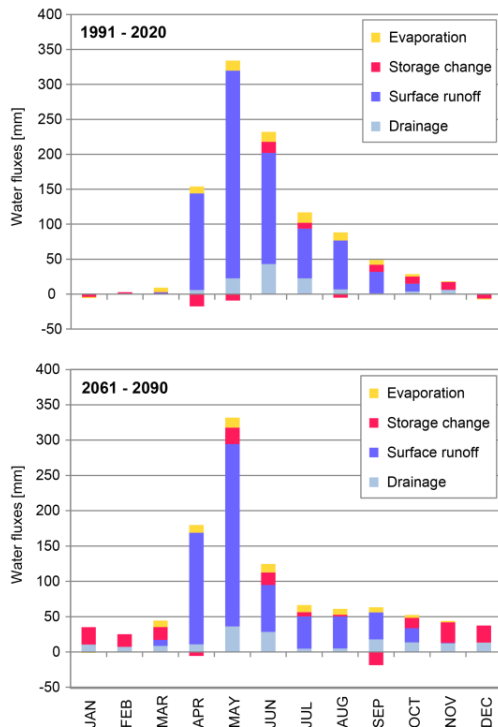


Figure 1. Mean monthly water fluxes in COUP for the time periods 1991 - 2020 and 2061 - 2090.

Conclusions

Although the model structures and complexities are quite different, similar annual runoff regimes are simulated for both the present-day situation and the future. An increase in the contribution of permafrost ice melt to runoff can be seen in both models.

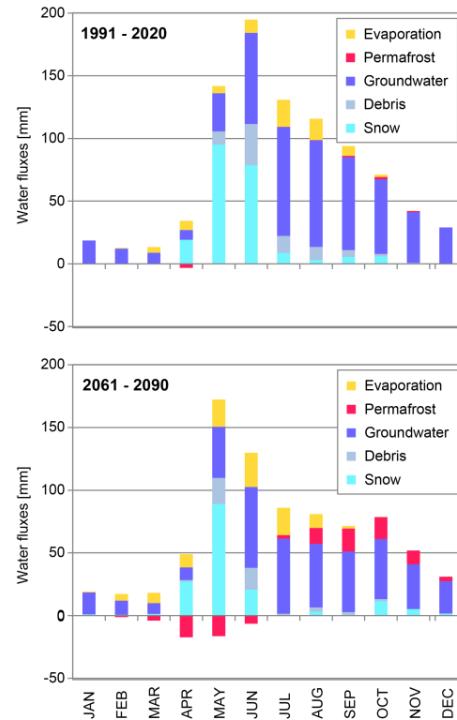


Figure 2. Mean monthly water fluxes in GERM for the time periods 1991 - 2020 and 2061 - 2090.

References

- Huss, M., Scherler, M., Schneider, S., Hoelzle, M. & Hauck, C. 2011. Future water yield from melting mountain permafrost: A fully distributed modeling approach. *Geophysical Research Abstracts*, EGU2011-11466.
- Jansson, P.-E. & Karlberg, L., 2011. Coup manual. Coupled heat and mass transfer model for soil-plant-atmosphere systems. *Royal Institute of Technology: Stockholm*, 435.
- Mittaz, C., Hoelzle, M. & Haeberli, W. 2000. First results and interpretation of energy-flux measurements of Alpine permafrost. *Annals of Glaciology* 31:275-280.
- Scherler, M., Hauck, C., Hoelzle, M., & Salzmann, N. 2013. Modeled sensitivity of two alpine permafrost sites to RCM- based climate scenarios. *Journal of Geophysical Research: Earth Surface*, 118(2), 780-794.
- PERMOS., 2016. Permafrost in Switzerland 2010/2011 to 2013/2014. Noetzli, J., Luethi, R., and Staub, B. (eds.), *Glaciological Report (Permafrost) No. 12-15 of the Cryospheric Commission of the Swiss Academy of Sciences*, 85 pp.
- Vonder Mühl, D. & Haeberli, W., 1990. Thermal characteristics of the permafrost within an active rock glacier (Murtèl/Corvatsch, Grisons, Swiss Alps). *Journal of Glaciology*, 36(123):151-158



Frozen ground, periglacial processes and mountain permafrost in the Monte Perdido-Tucarroya massif (The Pyrenees)

Enrique Serrano¹

Juan Ignacio López Moreno²

Raúl Martín-Moreno³

Manuel Gómez-Lende⁴

Alfonso Pisabarro¹

María González-García¹

Ibai Rico⁵

Esteban Alonso-González²

¹*Dpto. Geography, Universidad de Valladolid, Spain., email. serrano@fyl.uva.es*

²*Instituto Pirenaico de Ecología (CSIC), Spain.*

³*Dpto. Didácticas Específicas, Universidad Autónoma de Madrid, Spain.*

⁴*PANGEA, Universidad de Valladolid, Spain*

⁵*Dpto. Geography, Universidad del País Vasco, Spain.*

Abstract

The work studies the distribution of periglacial landform, seasonal frozen ground and permafrost in the high mountain of the Monte Perdido massif, Ordesa-Monte Perdido National Park. The ground thermal regimen, BTS, and geomorphological mapping of periglacial landforms and processes permit to know the distribution and activity of the ice in the ground. In the Tucarroya Cirque and Monte Perdido massif between 2500 and 2800 m the ground can remain free of ice whole year round. Between 2650 and 2780 are found seasonal frozen ground and landforms as gelifluction lobes and patterned ground, the most common periglacial feature in the studied area. Above 2760 permafrost possible appear in the North slope alternating with seasonal frozen grounds, where frost mounds are present. Finally, above 2885 the permafrost probable is developed.

Keywords: Mountain permafrost, seasonal frozen ground, periglacial, Pyrenees.

Introduction

The study area is in the Ordesa-Monte Perdido National park, in the Monte Perdido massif (3335 m) and the Tucarroya glacial cirque. It is a high valley placed between 2450 and 2800 m, a glacial area, where today exist the Monte Perdido glacier, of 37,7 Ha, the second one by extension of the Pyrenees, and moraine complexes of the Younger Dryas and the Little Ice Age. The main goal is to know the distribution of seasonal frozen grounds, mountain permafrost and current periglacial processes.

Methods

The method is based in four techniques. The mapping of periglacial shapes and processes at 1: 10,000 scale permits to know the presence and distribution of landforms and processes linked to ground ice. BTS measurements show the winter thermal conditions. 18 data-loggers (i-buttons models DS1922L and DS1921G)

installed in the study area during the period 2014-2016 have permits us to know the ground thermal regime. The annual average ground temperature, the average winter ground temperature, the freeze index and the thaw index have been also calculated. Solar Radiation Rate have been modelled in whole study area.

Results

The geomorphological indicators of the possible presence of frozen grounds, permanent or seasonal, and the thermal indicators allow to establish an altitudinal zonation of seasonal frozen ground or permafrost (Figure 1). Landforms associated with permafrost are very scarce and reduced in both surface and altitudinal extension. There are no rocky glaciers or protalud lobes, as they do exist in other cirques in the Pyrenees at the same altitudes. The presence of frozen bodies of metric to decametric sizes, gelifluction lobes and frost mounds, have been detected above 2770 m, and up to 3020, always in North slopes, indicating the possible existence

of permafrost. These altitudes and orientations are adjusted to those obtained from the thermal regime. BTS measures denote possible permafrost above 2765 m. In Tucarroya, three types of thermal regimes have been detected, showing the variation of temperatures and the possible presence of frozen ground.

1. Ground thermal regimes linked to atmospheric temperature. The ground remains free of ice whole year round, or can be developed seasonal frozen grounds.

2. Ground thermal regimes linked to the snow cover. It clearly indicates the absence of seasonal frozen grounds and permafrost in a wide altitudinal range between 2585 and 2970 m.

3. Thermal regimes with frozen grounds, where the ground temperature remains below 0°C, between 2650 and 3020 m. This regime denotes the existence of seasonal frozen grounds or permafrost. From 2980 m the ground thermal conditions indicate likely permafrost, interrupted in walls and hills, where topoclimatic conditions prevent their presence. The thermal conditions for the mountain permafrost development, sporadic or discontinuous, show up from 2760 m in Tucarroya and surroundings of Monte Perdido.

In the studied area, three geomorphological environments have been mapped: without ice in the ground; seasonal frozen grounds; and possible or likely permafrost. The presence of permafrost in Tucarroya is determined by the shading factors and, to a lesser degree, the altitude, so that it develops mainly on the northern slope. The largest extension of frozen grounds is represented by the seasonal frozen grounds, characterized by their annual freezing and thawing. They are kept frozen between 1 and more than 4 months and constitute the most effective geomorphological action. Gelifraction and gelifluction processes and patterned grounds are linked to the seasonal frozen grounds and scattered between 2650 and 3000 m. Patterned grounds are the most widespread periglacial landforms, join the gelifluction lobes, the last one located mainly at low altitudes. Between 2650 and 2780 are found seasonal frozen ground and landforms as gelifluction lobes and patterned ground, the most common periglacial feature in the studied area. Above 2760 permafrost possible appear in the North slope alternating with seasonal frozen grounds, where frost mounds are present, and above 2885 m the permafrost probable is developed. Finally, there are ice-free areas up to 2800 m, from this altitude the ice is always present in the ground.

Altitude	Ground temperature or landforms	Orientation	Indicador			
3075	-7,5	--	Seasonal frozen ground			
3030	Gelifluction lobes	N	Permafrost			
3020	-5,9	N	Permafrost probable	Probable permafrost		
3000	-3,4	S	Permafrost probable			
2967	0,5	--	No permafrost*			
2960	L.G.	N	Permafrost			
2920	L.G.	N	Permafrost			
2896	-3,9	S	Permafrost Probable			
2886	Gelifluction lobe	N	Permafrost			
2878	-1,0	S	Seasonal frozen ground	?		
2865	-1,4	S	Seasonal frozen ground			
2853	L.G.	N	Permafrost			
2850	Frost mounds	N	Permafrost			
2849	-1,4	SE	Seasonal frozen ground	Possible permafrost	Seasonal frozen ground	No ice in the ground
2849	-2,0	S	Possible Permafrost			
2818	-0,9	S	Seasonal frozen ground			
2810	L.G.	N	Permafrost			
2800	4,5	--	No permafrost			
2796	-0,9	N	Seasonal frozen ground			
2788	-2,3	S	Possible Permafrost			
2785	-1,5	S	Seasonal frozen ground			
2780	Gelifluction lobes	N	Permafrost			
2773	4,9	--	No permafrost			
2772	-2,5	N	Possible Permafrost			
2770	-2,6	N	Possible Permafrost			
2764	-2,1	N	Possible Permafrost			
2761	-0,3	N	Seasonal frozen ground			
2760	M.H.	N	Permafrost			
2760	-1,5	N	Seasonal frozen ground			
2757	-0,9	S	Seasonal frozen ground			
2755	0	S	No permafrost			
2753	0,3	N	No permafrost			
2748	-0,9	N	Seasonal frozen ground			
2739	-0,6	S	No permafrost			
2737	-0,8	N	No permafrost			
2730	-0,7	N	Seasonal frozen ground			
2717	-1,2	SE	Seasonal frozen ground			
2711	-1,7	S	Seasonal frozen ground			
2699	-0,4	S	No permafrost			
2692	-1,7	N	Seasonal frozen ground			
2688	-1,9	N	Seasonal frozen ground			
2676	-1,9	N	Seasonal frozen ground			
2650	-0,1	N	Seasonal frozen ground			
2620	0	N	No permafrost			
2585	2,8	S	No permafrost			

Figure 1. Indicators of frozen ground distribution in the Tucarroya and Monte Perdido.



Permafrost probability model for debris surfaces in the Central Andes (29° to 33° SL, Argentina).

Carla Tapia Baldis¹
Dario Trombotto Liaudat¹
Christian Halla²

¹*Ianigla (Argentine Institute of Snow Research, Glaciology and Environmental Sciences), CCT Conicet, Mendoza, Argentina, ctapia@mendoza-conicet.gob.ar*

²*Department of Geography, University of Bonn, Germany*

Abstract

A regional-extension permafrost distribution model was achieved, including locally adjusted data. It discriminates between permafrost in debris or loose sediments from rock permafrost and ice bodies. The final model is a combination of two separate occurrence probability models: a) mean annual air temperature-terrain ruggedness model and, b) mean annual air temperature-potential incoming solar radiation model. Possible permafrost, in coarse debris, is expected between 4200 to 5700 m asl (MAAT from -3° to -18°C) and covers a surface of aprox. 1200 km² in the Andes.

Keywords: Central Andes, mountain permafrost, probability model, debris surfaces.

Introduction

In the Central Andes of Argentina (28° to 33° SL/71° to 69° WL) different permafrost occurrence models were applied in the last years but only over reduced areas. On the other hand, Gruber's PZI global model (2012), locally displays biased data and due to its coarse resolution. Our approach aims to obtain a regional permafrost distribution model, including locally adjusted data that discriminates between permafrost below debris or loose sediments from rock permafrost and surface ice.

Study area

The study area comprises high altitude mountain ranges (Mercedario peak: 6770 masl), low precipitation rates (ca. 200-300 mm/yr from 30° to 33° SL and aprox. 100-150 mm/yr from 28° to 30° SL) with high solar radiation rates. Precipitation occurs mostly during the austral cold-season and the snow layer does not remain yearly outside protected niches. From a geomorphological point of view, Andean landscape is the result of different glacial, periglacial, paraglacial, alluvial and fluvial systems. Quaternary glacial stages modeled the landscape however; periglacial features dominate over the former ones today. The periglacial environment is expected above 3500 to 3800 m asl, while both active and inactive rock glaciers are located

approximately the same limit. At 3500 m asl, mean annual air temperature (MAAT) is about 1.3°C.

Methodology

An empiric-static model was used to estimate regional mountain permafrost distribution, using a logistic regression method. A similar approach was previously used by Brenning and Trombotto (2006) and Azócar *et al.* (2017). Predictive variables include mean annual air temperature (MAAT, °C), terrain ruggedness index (TRI) and potential incoming solar radiation (PISR, W/m²). The final model is a combination of two separate occurrence probability models: a) MAAT-TRI model and, b) MAAT-PISR model. As both models are independent, wholesome probability is equal to Model "A" Probability * Model "B" Probability.

The MAAT was previously modeled using the period from 1979 to 2010 gridded data from NCEP-CSFR reanalysis series, compared to the available, yet scarce, data from meteorological stations. As heat-transfer processes differ from coarse or blocky surfaces compared to cohesive rock outcrops, both should be discriminated as suggested by Boeckli *et al.* (2012). TRI values, obtained using the homonymous algorithm in SAGA GIS® with an ASTER-GDEM base are suitable for this task. PISR was calculated in SAGA GIS® using a time-lapse of 1 hour each 5 days during one year;

yearly values were then averaged for the period 1979-2010

The complete geomorphological characterization of the Bramadero river basin, chosen as calibration area, and the geomorphometric data from every single kind of landform (2344 units over 150 km²), were used to set the permafrost predictive categories. The first category (presence) includes geoforms that certainly indicate permafrost, such as; active rock glaciers, inactive rock glaciers, protalus ramparts, cryoplanation surfaces and perennial snow patches. The second category (absence) includes geoforms without permafrost (relict or fossil rock glaciers, bedrock, glacial abrasion surfaces, debris/mud flows and Andean peatlands). It includes as well geoforms where the presence of permafrost could not be certainly assessed such as, frozen and unfrozen talus slopes, glaciers and covered glaciers, moraines and morainic complexes, drift deposits, debris/snow avalanches, rock avalanches and rock slides and thermokarst depressions.

Results

MAAT-TRI model correctly displays the differences between coarse debris surfaces and bedrock while the MAAT-PISR model reflects more precisely temperature ranges for permafrost occurrence in the area, even though it overestimates its extension. Combining both models, realistic results in terms of permafrost distribution-patterns and temperature trends were achieved. Statistics of each model are displayed in Table 1. Results were cross-validated with the Argentine rock glacier inventory and with field work inspections.

Table 1. Logistic regression statics for MAAT-PISR and MAAT-TRI models.

	MAAT-PISR model	MAAT-TRI model
Observations	7463	7463
-2 Log	9485	7389
R ² (Cox and Schnell)	0.80	0.85
R ² (Nagelkerke)	0.85	0.9
AIK	9491	7395
AUROC	0.68	0.84

Possible permafrost, in coarse debris, is expected between 4200 to 5700 m asl (MAAT from -3° to -18°C) and covers a surface of approx. 1200 km² in the Andes. Likely permafrost is expected at 3400 to 4200 m asl (MAAT from 1.5° to -8°C) and cover a surface of ca. 6150 km². Besides, the Precordillera, displays 35 km² of likely permafrost.

Conclusions

The present probability model predict permafrost occurrence in debris surfaces for the study area, with good correlation with former rock glaciers inventories and professional expertise. However, it does not predict ice ground content or permafrost thermal state.

Acknowledgments

This study is part of the PhD thesis of C. Tapia Baldis. Funds come from the project PIP 1222015-0100913 (2015-2017) leader by Dr. Dario Trombotto.

References

- Azócar, G.F., Brenning, A. & Bodin, X., 2017. Permafrost distribution modelling in the semi-arid Chilean Andes. *The Cryosphere* 11: 877-890.
- Boeckli, A., Brenning, A., Noetzli, J. & Gruber, S., 2012. A statistical approach to modelling permafrost distribution in the European Alps or similar mountain ranges. *The Cryosphere* 6(1): 125-140.
- Brenning, A. & Trombotto, D., 2006. Logistic regression modeling of rock glacier and glacier distribution: Topographic and climatic controls in the semi-arid Andes. *Geomorphology* 81: 141-154.
- Gruber, S., 2012. Derivation and analysis of a high-resolution estimate of global permafrost zonation. *The Cryosphere* 6(1): 221-223.



Frozen ground in the cold-arid Himalaya: a case study from upper Ganglass catchment, Leh

John (Mohd) Wani¹

Renoj (J.) Thayyen²

C.S.P. Ojha¹

Stephan Gruber³

Dorothea Stumm⁴

¹Department of Civil Engineering, Indian Institute of Technology, Roorkee, India-247667, johnn.nith@gmail.com

²National Institute of Hydrology, Roorkee, India-247667

³Carleton University, Ottawa, Canada

⁴International Centre for Integrated Mountain Development (ICIMOD), Kathmandu, Nepal

Abstract

Long-term data series of ground temperatures in high elevation cold-arid regions are important to improve understanding of seasonally frozen ground and permafrost. In 2016, the National Institute of Hydrology (NIH), Roorkee, established ground temperature monitoring network in the cold-arid trans-Himalayan region of Ladakh. This network consists of 26 ground temperature (sub-surface) data loggers placed at a depth of 10 cm at elevations of 4700–5600 m a.s.l. recording data every 20 minutes. For installation of data loggers, the selection of plots was done with focus to cover the influence of topographic variables such as slope, aspect and elevation, and finally the ground cover types. In September 2017, one year of data from 24 loggers was retrieved. The database generated will provide an understanding of the near-surface ground thermal regime and potential permafrost occurrence. In this study, first results from the measurement campaign are presented.

Keywords: cold-arid region; data loggers; frozen ground; Himalayas; Ladakh

Introduction

Permafrost is a rarely studied (but likely important) component of high elevation cold-arid mountain systems. An initial assessment estimates the permafrost area in the Hindu Kush Himalaya (HKH) region to be 1 ± 0.5 million km² (Gruber *et al.*, 2017). A remote-sensing study of rock glaciers suggest their occurrence in the region at an elevation of 3500–5500 m a.s.l. (Schmid *et al.*, 2015). Allen *et al.*, (2016) made a spatial simulation of permafrost in the Kullu district of Himachal Pradesh, India. To better understanding ground thermal regimes, permafrost distribution, and their changes, long-term ground-temperature measurements can prove cost effective. So far, however, such data is not available in the Indian Himalayas. We started the first measurement campaign by installing miniature temperature data (MTD) loggers. Their data can provide information about the duration of snow-cover, start of snow melt, zero-curtain period, mean annual ground temperatures (MAGT), and period of ground freezing and thawing, etc. (Hoelzle *et al.*, 2003). These results provide a basis for monitoring of change over time, as well as for further efforts to simulate (*e.g.*, Fiddes *et al.*, 2015) and map permafrost distribution and characteristics. The aim of this study is to investigate ground temperature, seasonal freezing/thawing, and the presence of permafrost in the upper Ganglass catchment.

Methods

Logger installation

In August 2016, we installed 26 MTDs (24 M-Log5W simple in soil/debris and 2 M-Log5W cable in bedrock, manufactured by GeoPrecision) at 10 cm depth in ten different plots as distinguished by ground cover and topography. These were at elevations of 4700–5600 m in the upper Ganglass catchment (34.25–34.29°N 77.55–77.65°E) Leh, Ladakh. The data is available from September 2016 to August 2017.

Data analysis

The variability of MAGT is investigated at two scales by following the approach of Gubler *et al.* (2011):

(a) The coarse scale in which we analyze the inter-plot variability of the mean MAGT (μ_p), which in plot p is defined as the mean of the mean of each time series within that plot:

$$\mu_p = \frac{1}{n_p} \sum_{i=1}^p \mu_{p,i}$$

Where n_p is the number of loggers inside that plot and $\mu_{p,i}$ is the MAGT of each logger within the plot.

(b) Fine scale, in which we analyse the intra-plot variability of MAGT (x_p) and is defined by the range of MAGT inside that plot:

$$\xi_p = \max_{i=1, \dots, n_p} (\mu_{p,i}) - \min_{i=1, \dots, n_p} (\mu_{p,i})$$

The length of zero-curtain period was estimated by following the procedure of Schmid *et al.* (2012).

Results

The instantaneous ground temperatures recorded by all soil/debris loggers during study period are between 20.2 to -22.7°C recorded at an elevation of 4700 and 5600 m a.s.l. respectively. The ground temperatures of the two bedrock loggers at an elevation of 5075 m a.s.l. vary between 29.2 and -21.2°C. The average MAGT for all the sites during the study period was -3.03°C. The typical ground temperature data recorded by a logger located in a fine material stripe is shown in Fig. 1.

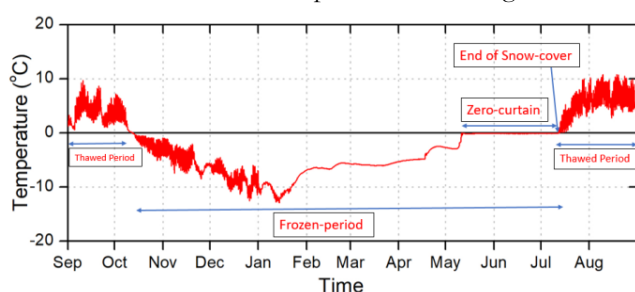


Figure 1. Typical ground temperature data recorded by a miniature data logger from one of the sites in upper Ganglass catchment, Leh during the period Sep-2016 to Aug-2017.

The inter-plot range of MAGT is 10.5°C, ranging from -8.4 to 2.1°C, whereas the intra-plot variability ranges from 0.04 to 3.4°C. The MAGT data recorded were compared with slope, aspect and elevation (not shown). The relationship of MAGT was strong with elevation followed by slope and aspect. The elevation displayed strongest correlation with MAGT ($R^2 = 0.78$). The slope angle exhibits the second highest correlation ($R^2 = 0.70$). Slope aspect exhibits the weakest correlation with MAGT ($R^2 = 0.13$). Future work will analyse the influence of solar radiation.

The mean annual air temperature (MAAT) at all the logger sites ranges from -8.9 to -2.6°C with average MAAT of -5.7°C. The surface offset estimated at all the sites is between -1.1 to 5.1°C, with most sites having values near 2.7°C.

At all the logger sites, the frozen period varies between 131 to 217 days during the study period. The snow cover melt-out dates for all the loggers vary from 12th May 2017 to 8th Aug 2017.

Conclusions

From the MTD data, 21 out of 24 loggers have MAGT below 0°C. The elevation of the highest logger

with positive MAGT is 4727 m a.s.l. and the elevation of the lowest logger with negative MAGT is 4934 m a.s.l. However, there is an exception with MAGT of 0.01°C recorded at 5075 m a.s.l. by one of the loggers installed in bedrock. Even if there are some inter-annual fluctuations, the ground temperatures observed are a reliable indication of having permafrost in this catchment. Hence, these sites will be our focus to further investigate the presence and characteristics of Himalayan permafrost.

Acknowledgments

John Mohd Wani acknowledge the Ministry of Human Resource Development (MHRD) Government of India (GOI) fellowship for carrying out his Ph.D. work. Renoj J. Thayyen thank National Institute of Hydrology (NIH) Roorkee and SERB (Project No. EMR/2015/000887) for funding the instrumentation in the Ganglass catchment. The assistance of ICIMOD is also highly acknowledged.

References

- Allen, S. K., Fiddes, J., Linsbauer, A., Randhawa, S. S., Saklani, B., Salzmann, N. 2016. Permafrost studies in Kullu district, Himachal Pradesh. *Current Science* 11: 257-260.
- Fiddes, J., Endrizzi, S., Gruber, S., 2015. Large-area land surface simulations in heterogeneous terrain driven by global data sets: application to mountain permafrost. *The Cryosphere* 9: 411-426.
- Gruber, S., Fleiner, R., Guegan, E., Panday, P., Schmid, M. O. *et al.*, 2017. Inferring permafrost and permafrost thaw in the mountains of the Hindu Kush Himalaya region. *The Cryosphere* 11: 81-99.
- Gubler, S., Fiddes, J., Keller, M., Gruber, S., 2011. Scale-dependent measurement and analysis of ground surface temperature variability in alpine terrain. *The Cryosphere* 5: 431-443.
- Hoelzle, M., Haeberli, W., Stocker-Mittaz, C., 2003. Miniature ground temperature data logger measurements 2000-2002 in the Murtèl-Corvatsch area, Eastern Swiss Alps, in: *Proceedings of the Eighth International Conference on Permafrost*, Zurich, Switzerland, 20-25 July: 25.
- Schmid, M. O., Gubler, S., Fiddes, J., Gruber, S., 2012. Inferring snowpack ripening and melt-out from distributed measurements of near surface ground temperatures. *The Cryosphere* 6: 1127-1139.
- Schmid, M. O., Baral, P., Gruber, S., Shahi, S., Shrestha, T., Stumm, D., Wester, P., 2015. Assessment of permafrost distribution maps in the Hindu Kush Himalayan region using rock glaciers mapped in Google Earth. *The Cryosphere* 9: 2089-2099.

Convective Heat Transfer in Coarse Permafrost Substrate: A Numerical Model Study in the Swiss Alps

Jonas Wicky¹

Christian Hauck¹

¹University of Fribourg, Department of Geosciences, Alpine Cryosphere and Geomorphology Group (jonas.wicky@unifr.ch)

Abstract

In an Alpine permafrost setting the coarse blocky terrain (talus slopes, rock glaciers etc.) is often very porous. The high permeability of such landforms allows air to circulate within the soil, which influences ground temperature and therefore permafrost conditions. Recently, a numerical model approach realistically simulated this internal air circulation, which takes place under free convection conditions as result of density differences between warm and cold air with no additional forcing. The resulting seasonally reversing (chimney-type-) circulation leads to a substantial cooling in the lower part of a talus slope. The present study shows that the type of convection and therefore the influence on the ground thermal regime strongly depends on the slope angle and the permeability.

Keywords: Mountain permafrost; convection; talus slope; numerical model; heat transfer

Introduction

Thermal modelling is important for a better understanding of the ground thermal regime in Alpine permafrost. The presented modelling approach makes use of common concepts in engineering sciences (FE-modelling) to represent and quantify convective heat transfer in air in coarse permafrost substrate. Many observation-based studies addressed the effect of convective heat transfer in air (e.g., Delaloye *et al.*, 2003). Modelling approaches are still rare and often limited to one dimension (Scherler *et al.*, 2014; Luethi *et al.*, 2017), which neglects lateral heat transfer. Previous results from a 2-D model showed that convective heat transfer leads to a substantial cooling in the lower part of a talus slope (Wicky & Hauck, 2017). We now extend this modelling approach to a parametric sensitivity study on different slope angles and permeabilities.

Model

The model consists of a numerical domain representing a schematical talus slope divided in two subdomains, one for bedrock and another one for porous substrate (Fig. 1). The lower thermal boundary condition is set to 0.6°C (borehole observation) and the upper boundary is the median from a ground surface temperature (GST) logger time series at Lapires talus slope in Valais Alps, Switzerland (Permos, 2016). Slope angle varies from 0° – 40° and permeability from 1e-7 to 8.89e-5 m⁻¹ (Goering & Kumar, 1996; Herz, 2006). The model solves for heat transfer accounting for convection and for air circulation (Darcy's law with Boussinesq

approx.) and is set up within the software package Comsol Multiphysics.

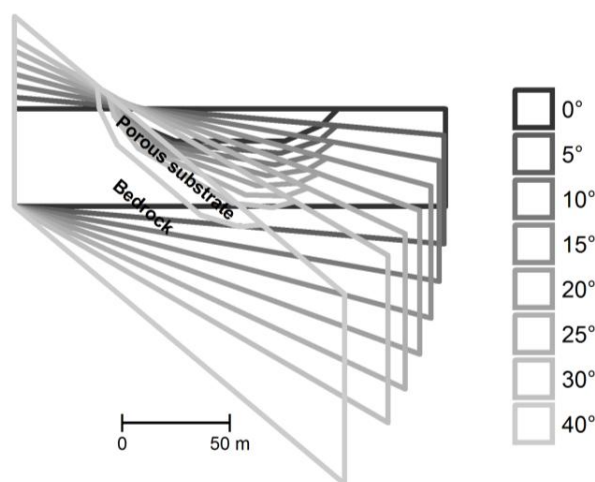


Figure 1. Different geometries used to model different slope angles.

Results

The air velocity within the porous domain increases with increase of slope angle and permeability. Ground temperature (GT) shows a more complex behavior. The different behaviors are explained by different circulation patterns. Depending on the parameter set, three different circulation patterns may take place: Multicellular vertical convection, lateral advection cells and unidirectional downflow (Fig. 2). These circulation patterns have an influence on the GT: Seasonally reversing lateral advection (chimney-type circulation)

leads to a pronounced cooling in the lower part of the domain, multicellular convection leads to uniformly colder GT and unidirectional downflow mainly leads to a fast propagation of the surface boundary temperature into the ground. Lateral advection leads to the coldest GT, multicellular convection to a uniform cooling, whereas unidirectional downflow results in warmer GT compared to a setting without convective heat transfer (conduction only).

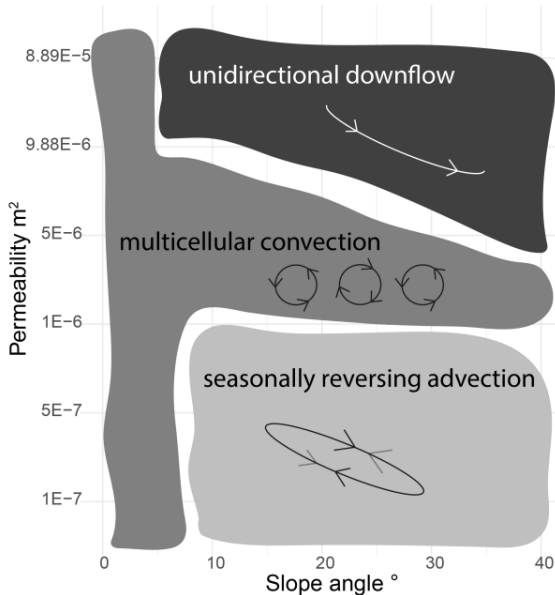


Figure 2. Sketch of different circulation patterns relative to slope angle and permeability.

Conclusion

We modelled successfully convective circulation within porous permafrost substrate and we are able to show the influence of slope angle and permeability on the circulation pattern and thus the ground thermal regime. Our results help to explain isolated permafrost occurrences and thermal anomalies within continuous permafrost. The improved process understanding may be integrated in permafrost mapping or long-term permafrost modelling projects.

Acknowledgments

This study was conducted within the MODAIRCAP project funded by the SNF (n° 200021_169499). We are thankful to PERMOS for the temperature data.

References

Delaloye, R., Reynard, E., Lambiel, C., Marescot, L. & Monnet, R., 2003. Thermal anomaly in a cold scree slope (Creux du Van, Switzerland). *Proceedings of the 8th*

International Conference on Permafrost, Zurich, Switzerland, July 21-25.

Goering, D.J. & Kumar, P., 1996. Winter-time Convection in Open-Graded Embankments. *Cold Regions Science and Technology*, 24: 57–74.

Herz, T., 2006. *Das Mikroklima grobblockiger Schutthalden der alpinen Periglazialstufe und seine Auswirkungen auf Energieaustauschprozesse zwischen Atmosphäre und Lithosphäre*. Giessen: Universitätsbibliothek, 224pp.

Luethi, R., Phillips, M. & Lehning, M., 2017. Estimating Non-Conductive Heat Flow Leading to Intra-Permafrost Talik Formation at the Ritigraben Rock Glacier (Western Swiss Alps). *Permafrost and Periglacial Processes*, 28(1): 183-194.

PERMOS, 2016. PERMOS Database. *Swiss Permafrost Monitoring Network*, Fribourg, Switzerland.

Scherler, M., Schneider, S., Hoelzle, M. & Hauck, C., 2014. A two-sided approach to estimate heat transfer processes within the active layer of the Murtèl–Corvatsch rock glacier. *Earth Surface Dynamics*, 2(1): 141-154.

Wicky, J. & Hauck, C., 2017. Numerical modelling of convective heat transport by air flow in permafrost talus slopes. *The Cryosphere*, 11(3), 1311-1325.

26 - Open session on permafrost hydrology

Session 26

Open session on permafrost hydrology

Conveners:

- **William L. Quinton**, Cold Regions Research Centre, Wilfrid Laurier University, Waterloo, Ontario, Canada
- **Ryan F. Connon**, Wilfrid Laurier University, Yellowknife, NT, Canada (PYRN member)
- **Chris Spence**, Environment and Climate Change Canada, Saskatoon, SK, Canada

Permafrost hydrology seeks to understand the flux and storage of water and energy in earth systems where temperatures are at or below 0°C for at least two consecutive years. The supra-permafrost layer includes the active layer, a zone that freezes and thaws annually, and may also include a perennally thawed (i.e. talik) layer. By impounding and re-directing surface and subsurface water, permafrost influences both the nature of hydrological flowpaths and the partitioning of hydrological input into runoff and storage. Permafrost also promotes high moisture contents in the overlying layers by limiting infiltration, and by providing structural support to the overlying terrain, permafrost strongly influences the nature of the supported ecosystems, including their hydrological characteristics. Most hydrological processes and pathways occur above the permafrost, both within the supra-permafrost layer, and above the ground surface. Permafrost thaw and the resulting ground surface subsidence and ecosystem change has the potential to alter hydrological processes from local to regional scales. Understanding the interdependence of permafrost, hydrology and ecosystems is critical to understanding not just the flux and storage of water in permafrost terrains, but also how such systems might change in response to climate and anthropogenic disturbance.



Characterization of Runoff Within a Periglacial Micro-Watershed of the Andes Containing Rock Glaciers

Lukas U. Arenson¹
Pablo A. Wainstein²
Jordan S. Harrington³
Holly A. Miller⁴

¹BGC Engineering Inc. Vancouver BC, Canada, larenson@bgcengineering.ca

²BGC Engineering Inc., Calgary, AB, Canada

³BGC Engineering Inc., Vancouver, BC, Canada

⁴University of Colorado, Boulder, CO, USA

Abstract

Water chemistry and isotope analysis, together with surface runoff and groundwater level measurements, were conducted in a small watershed containing rock glaciers in the Central Andes of South America. Preliminary results indicated that the temporal and spatial differences in the water chemistry and isotopic signatures are likely related to the thaw front penetrating the active layer, and that there is no discernible contribution from rock glacier ground ice melt to the runoff. However, the results currently available are preliminary and additional data from this ongoing study are required to confirm these initial findings.

Keywords: Rock Glacier; Runoff; Water Chemistry

Introduction

The hydrology of mountain systems in the arid Central Andes of South America is of great interest to the scientific community, but also project developers, regulators, NGOs and local stakeholders, because of the need for fresh, clean water for industrial, domestic and agricultural use in the region (Viviroli & Weingartner, 2004; Viviroli *et al.*, 2007; Arenson & Jakob, 2010). Past research studies on mountain hydrology primarily focused on headwater catchments dominated by snowmelt runoff and glaciated terrain (Duguay *et al.*, 2015; Cowie *et al.*, 2017). However, our understanding of the contributions from and the role of ground ice in mountain permafrost terrain, and specifically from rock glaciers, to the hydrology of these mountain regions is less well known and a quantitative accounting of the hydrologic role of rock glaciers remains mainly unresolved (Duguay *et al.*, 2015; Arenson & Jakob, 2010).

The majority of currently available rock glacier research focuses on their dynamics and morphology (Barsch, 1996; Williams *et al.*, 2006; Arenson *et al.*, 2016). One reason for this focus is the difficulty in collecting hydrologic and geochemical information about rock glaciers due to their location and structure. The higher percentage of rocks in rock glaciers compared to ice in

glaciers presents extra difficulties in collecting ground ice samples through boreholes, and the logistics of collecting melting ground ice water in high alpine regions are challenging (Williams *et al.*, 2006; Leopold *et al.*, 2011; Thies *et al.*, 2013).

Thermal and morphologic properties of rock glaciers are significantly different than those of glaciers (Barsch 1996), which results in radically different hydrologic responses. For example, rock glaciers are slower to respond to long-term (climate) and seasonal changes due to the thermal protection of the thick and coarse-grained active layer (Duguay *et al.*, 2015). In addition, the morphology and dynamics of rock glaciers do not depend on annual mass balances driven by accumulation and ablation, as is the case for glaciers.

We present preliminary results of the first year of analyzing water chemistry and isotopes as indicators for the origin of surface water collected within a micro-watershed containing rock glaciers.

Preliminary Results

Lower proportion of sodium and higher proportion of sulfate were measured at the bottom of the watershed containing the rock glacier compared to nearby stations, producing a unique geochemical signature. These

geochemical differences are caused by interactions of water with the local geology.

Stable naturally occurring water isotopes, $\delta^{18}\text{O}$ and δD , are used to identify the contributions of source waters to the hydrologic system, which is the results of a mixture of groundwater, surface water, snow and ground ice melt. The isotopic signature of the runoff directly downstream of the rock glacier (Station A5 (squares) in Figure 1) shifts from a uniquely enriched signal in February towards a depleted signal in December relative to other waters in the watershed. December is the beginning of summer. The enrichment in the samples in the late melting period may indicate the presence of meltwater coming from the seasonally frozen ground within the active layer from higher bounds of the watershed, where the freezing and thawing cycles are stronger and as such the water's isotopic signature gets enriched as more phase changes occur.

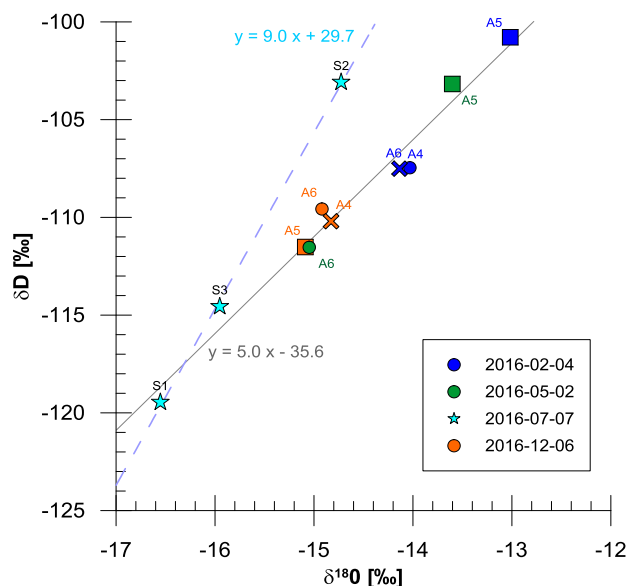


Figure 1. Isotopic composition of samples in the micro-watershed measured at various times. Samples from July 2016 are snow samples.

Preliminary Conclusions

Water chemistry and isotope analysis, together with surface runoff and ground water level measurements show that there are differences in the origin of the water in the watershed containing a rock glacier compared to runoff from non-rock glacier containing areas. The differences are, however, most noted during the summer when the thaw front penetrates the active layer releasing seasonally frozen water. Towards the end of the summer, when the thaw front reaches the permafrost table (~April), no significant differences were noted, which would be indicative of an absence in contribution of rock glacier ground ice melt to the runoff.

The results presented herein are preliminary and are currently being complemented with additional sampling and analysis to help support the aforementioned, initial conclusion.

References

- Arenson, L.U. & Jakob, M., 2010. The significance of rock glaciers in the dry Andes - A discussion of Azócar and Brenning (2010) and Brenning and Azócar (2010). *Permafrost and Periglacial Processes* 21: 282–285.
- Arenson, L.U., Kääh, A., & O'Sullivan, A. 2016. Detection and Analysis of Ground Deformation in Permafrost Environments. *Permafrost and Periglacial Processes* 27: 339–351.
- Barsch, D. 1996. *Rockglaciers: Indicators for the Present and Former Geocology in High Mountain Environments*. In Springer Series in Physical Environment. Springer-Verlag, Berlin Heidelberg.
- Cowie, R.M., Knowles, J.F., Dailey, K.R., Williams, M.W., Mills, T.J. & Molotch, N.P., 2017. Sources of streamflow along a headwater catchment elevational gradient. *Journal of Hydrology* 549: 163–178.
- Duguay, M.A., Edmunds, A. & Arenson, L.U., 2015. Quantifying the significance of the hydrological contribution of a rock glacier – A review. *Proceedings of GEOQuébec 2015. 68th Canadian Geotechnical Conference and 7th Canadian Permafrost Conference*: 8 p.
- Leopold, M., Williams, M.W., Caine, N., Völkel, J. & Dethier, D., 2011. Internal structure of the Green Lake 5 rock glacier, Colorado Front Range, USA. *Permafrost and Periglacial Processes* 22: 107–119.
- Thies, H., Nickus, U., Tolotti, M., Tessadri, R., & Krainer, K. 2013. Evidence of rock glacier melt impacts on water chemistry and diatoms in high mountain streams. *Cold Regions Science and Technology* 96: 77–85.
- Viviroli, D., Dürr, H.H., Messerli, B., Meybeck, M. & Weingartner, R., 2007. Mountains of the world, water towers for humanity: Typology, mapping, and global significance. *Water Resources Research* 43: W07447.
- Viviroli, D. & Weingartner, R., 2004. The hydrological significance of mountains: from regional to global scale. *Hydrology and Earth System Sciences* 8: 1016–1029.
- Williams, M.W., Knauf, M., Caine, N., Liu, F., Verplanck, P.L., 2006. Geochemistry and source waters of rock glacier outflow, Colorado Front Range. *Permafrost and Periglacial Processes* 17: 13–33.

High Arctic Sediment Yield Responses to Geomorphic and Permafrost Change in a Transitioning Climate

Casey R Beel¹
Scott F Lamoureux¹
John F Orwin^{1,2}

¹*Department of Geography and Planning, Queen's University, Kingston ON Canada K7L 3N6, 15cb29@queensu.ca*

²*Environmental Monitoring and Science Division, Alberta Environment and Parks, Calgary AB Canada T3L 1S4*

Abstract

That the Arctic is changing is no longer in question. How much it will change and how that change is propagated through geomorphic systems are important questions as surface air temperatures and precipitation patterns continue to change in the foreseeable future. In the first long-term High Arctic sediment investigation we demonstrate the response of a fluvial system to an episode of permafrost disturbance.

Keywords: High Arctic, Permafrost, Geomorphic Change, Suspended Sediment Transfer, Connectivity, Cape Bounty Arctic Watershed Observatory

Introduction

Enhanced climatic warming in the High Arctic has led to an increase in the occurrence of landscape disturbances in recent decades. Landscape disturbances that connect with channel networks may have a substantial impact on suspended sediment transfer dynamics. However, the impact and recovery of disturbance on the fluvial geomorphic system is poorly understood due to a dearth of long-term monitoring sites in these settings. Similarly, the linkages between climatic drivers, discharge generation and suspended sediment transfer remains poorly understood for much of the Arctic because of this lack of available data.

Long-term records of suspended sediment transfer are important for understanding how landscapes are responding to enhanced climatic warming and permafrost change. This is because suspended sediment transfer is a sensitive indicator of landscape change, since it is broadly supply controlled. Channel suspended sediment flux has been monitored in paired watersheds at the Cape Bounty Arctic Watershed Observatory (CBAWO), Melville Island, Nunavut (Figure 1) since 2003 (excluding the years 2011, 2013, and 2015 due to logistical constraints) and represents the longest High Arctic record in existence. In 2007, both watersheds were impacted by extensive permafrost disturbances on slopes and along the channels. Disturbances on slopes resulted in the formation of new slope tributary streams and significantly increased slope erosion. As a result, our records provide us with a unique dataset that allow us to

investigate the long-term geomorphic responses to landscape disturbances. The objectives of this research was to (i) identify the main controls on discharge generation and suspended sediment transfer, (ii) investigate the long-term geomorphic responses to landscape disturbances, and (iii) to consider the stability and evolution of High Arctic landscapes in a transitioning climate.

Our long-term results indicate prominent decoupling between climatic drivers and geomorphic energy in the fluvial system. Annually, discharge generation and suspended sediment transfer are not a function of summer climate, but driven by snow availability for melt and by geomorphic controls. Short-term geomorphic disturbances, coupled with hydroclimatic change, should increase the intensity of downstream sediment flux. However, our results show a significant decrease in downstream sediment flux post-2007 landscape disturbances. These results suggest that short-term geomorphological disturbances compete with hydroclimatic change in these watersheds. We hypothesize that this is also largely a result of weak landscape connectivity, and that fluvio-geomorphic connectivity is the tipping point to Arctic landscape change.

An experimental study of permafrost restoration under the seismic line in the wetland-dominated zone of discontinuous permafrost, Northwest Territories, Canada

Michael Braverman^{1,2}

William Quinton¹

¹Cold Regions Research Centre, Wilfrid Laurier University, Waterloo, ON

²GHD Canada, Waterloo, ON

Abstract

Thermosyphons are closed-system heat extraction devices. They extract heat from the ground, contributing to cooling of frozen ground and maintaining temperature below zero and as such are useful for preserving permafrost. Two types of thermosyphons are used: passive and hybrid systems. Passive one does not require any external power to operate. The hybrid installation combines the passive system with a refrigeration compressor so that negative soil temperatures are maintained during summer. The most common type of thermosyphon uses a carbon dioxide filled vessel under a pressure varying from about 2100 to 4800 kPa. Thermosyphon technology is successfully used for stabilizing building foundations, dams and pipelines. While passive thermosyphons do not require extensive maintenance they do require specially trained personal for installation. Also the high cost of thermosyphons limit their extensive use below linear infrastructure. Liquid based thermosyphons were developed and tested as an inexpensive alternative to carbon dioxide system. This paper presents and discussed the technical aspects of liquid-filled thermosyphons and demonstrates their application in a region of degrading permafrost at Scotty creek, NW, Canada.

Keywords: Seismic line, permafrost, thermosyphons.

Introduction

Surface disturbance of ice rich soils in permafrost regions results in permafrost degradation, reduction of ground bearing capacity and slope stability problems. Preventing permafrost thaw is a serious concern for the construction industry. One of the most popular methods of maintaining permafrost in its natural state is the use of thermosyphons. Thermosyphons have been used for stabilizing foundations in continuous and discontinuous permafrost areas since 1960 Richardson, (1979). There are two types of thermosyphons: passive and hybrid Johnston, (1981). Passive thermosyphons contain no moving parts. These sealed pipes are usually filled with carbon dioxide at a high pressure of 2-5 MPa. Pipe pressure should be adjusted during installation to ensure that carbon dioxide located below ground is maintained in liquid form. Vaporization of the liquid carbon dioxide results in a heat transfer from the lower part, the evaporator, of the thermosyphon to the upper part, the condenser, where it condenses in winter time and trickles back down to the evaporator. Passive thermosyphons work only in the winter time and remain dormant while the air temperature is higher than the ground temperature. Hybrid thermosyphons are designed to keep the ground frozen in the summer as well as the winter time, but this process involves an active refrigeration system.. While ground freezing with

thermosyphons can be considered as a “last line of defence” when any other methods for foundation stabilization are not available or are not feasible due to geotechnical conditions or high costs, this technology is nonetheless very expensive. According to the Government of the Northwest Territories, Department of Transportation, climate change may affect the quality of Highway 3, the main highway of the NWT, which is already under extensive maintenance every summer. However, thermosyphon technology is not applied in this case because of associated costs, among other factors. The complex installation process of thermosyphons is another factor which limits their use. Heuer, (1979) noted that installation of heat pipes affects construction timing, as it requires special knowledge and skills, which are often not available within general drilling contractor crews.

Thermosyphons are an effective, but expensive technology for the prevention of permafrost thaw. The cost of this technology limits its application under linear structures such as roads. In some cases, it is more prudent to invest in road maintenance, rather than the prevention of permafrost thaw. The proposed thermosyphon system can easily overcome the above mentioned problems due to the simplicity of its design and its low cost. This system does not require any special training or licencing for its operation, although

the need for some maintenance may limit use in remote, regions.

Site location

The Scotty Creek basin is located approximately 50 km SE of Fort Simpson, NT. (Figure 1)

The average annual temperature in the region is -3.20 C. (1964-2013). The average temperatures for July and January are 17.10 C and -25.90 C, respectively. This area belongs to the continental climate zone and is situated in the region of discontinuous permafrost. The soil layer of interest is 100% saturated peat with a porosity of ~ 80%. The testing of performance was done during the winter of 2016-2017. The test site was equipped with temperature monitoring stations in August 2014.

Description and Principals of Operation

Liquid based thermosyphons were developed and tested as an inexpensive alternative to carbon dioxide system.

The proposed thermosyphon consists of two coaxial pipes. The external is aluminum pipe and had a length of 3 m and a diameter of 75 mm. The maximum snow thickness for the experiment was ~50 cm. Thus, only 50 cm of the thermosyphon was exposed to open air. The thermosyphon was equipped with a low power consumption (0.8 W) submersible pump to circulate the coolant. The outflow from the submersible pump was directed through 12.5 mm internal pipe to the bottom of the thermosyphon. The operational rate of the pump was between 40 and 120 L hr⁻¹, depending on the performance of the solar panel. The power line was equipped with a mechanical thermal switch, which connected the power supply to the pump when air temperatures dropped below zero. Four thermistors were placed around the thermosyphon at various distances and depths. An additional thermistor was placed close to the bottom of the thermosyphon at a depth of 199 cm. Figure 1 demonstrates test results for Case B.

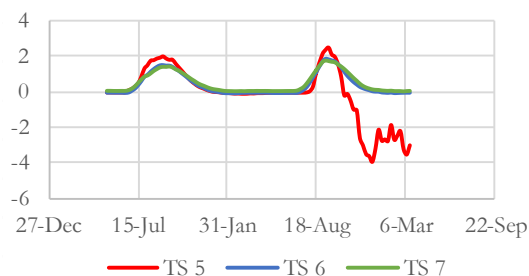


Figure 1. Temperature distribution around thermosyphon #5 recorded by thermistors # 5,6 and 7

As shown in Figure 1, the soil in close proximity of the thermosyphon was frozen to an average temperature of ~ -30C. Radius of freezing reached ~ 20 cm with average temperature ~-0.5°C.

Conclusions

This paper presents the results of an experimental study of liquid filled thermosyphons with forced circulation. With recent developments in energy-conserving technologies and renewable energy sources, the system presented here is an economically feasible alternative to traditional two phase passive thermosyphons. According to data obtained from the field experiment, the proposed thermosyphon can transfer sufficient thermal energy to freeze the saturated peat layer within a diameter of at least 50 cm around, even with a relatively short above-ground section. The low power consumption submersible pump can maintain a below 0oC temperature in the frozen layer throughout the cold season, while operating exclusively on a renewable energy source, such as a solar panel or a small wind turbine generator.

Data obtained from field experiments shows that even with a relatively short above-ground section, which is exposed to cold air, the proposed thermosyphon can transfer sufficient thermal energy to freeze the saturated peat layer at a diameter of at least 0.4 m around a 3 inch thermosyphon. It should be noted that only one thermosyphon was tested in this experiment. A cluster of thermosyphons can be expected to yield much better result.

The content of this paper has patent pending status

References

- Heuer, C. E. 1979. The application of heat pipes on the Trans-Alaska Pipeline. Directorate of Military Programs Office, Chief of Engineers. Hanover, NH: US Army Cold Regions Research and Engineering Laboratory.
- Holubec, I. 2008. Flat loop thermosyphon foundations in warm permafrost. Government of the Northwest Territories Asset Management Division of Public Works and Services and the Climate Change Vulnerability Assessment of the Canadian Council of Professional Engineers.
- Richardson, P., 1979. Tough Alaska conditions prove new pile design's versatility. Alaska Construction and Oil, February: 20–28.

Government of the Northwest Territories, Department of Transportation Engineers, Canada Public Infrastructure, Engineering Vulnerability Committee,

Climate Change Vulnerability Assessment for NWT
Highway 3, Final Report, Project No: 0836-002, August
10, 2011



Rock glacier outflows: a distinct alpine stream type?

Stefano Brighenti^{1,3}
Michael Engel²
Monica Tolotti³
Maria Cristina Bruno³
Francesco Comiti²
Walter Bertoldi¹

¹Department of Civil, Mechanical and Environmental engineer University of Trento, Italy, stefano.brighenti@unitn.it

²Faculty of Science and Technology, Free University of Bolzano (BZ, Italy)

³ Research and Innovation Centre, Edmund Mach Foundation, S. Michele all'Adige, Italy

Abstract

Alpine glaciers are predicted to significantly decrease their water contribution to European Alps ecohydrology, while rock glaciers may become increasingly important due to their slower ice loss. Different alpine stream habitat types can be distinguished according to water source. However, despite the large amount of literature available for glacier-, groundwater- and snowmelt/precipitation-fed habitats, very little is known on rockglacier-fed streams. We describe the habitat parameters of two rockglacier outflows during summer 2017, compared to streams with different water origin (two groundwater-fed, two glacier-fed, one mixed origin) in the upper Solda Valley (Eastern Italian Alps). The Solda rockglacier stream is characterized by high channel stability, low turbidity, high electrical conductivities and high Ca, Mg, PO₄, Sr, As and Ba concentrations. The water chemistry of the Zay rock-glacial stream resembles the stream of mixed origin. Results suggest a potential hydroecological role of rockglacier-fed streams in the context of Alpine deglaciation.

Keywords: Deglaciation, rock glacial streams, Alpine hydroecology, habitat conditions

Introduction

Rockglaciers are one of the most evident forms of permafrost in mountain areas such as in the European Alps, where they often feed streams or lakes (e.g Mair *et al.*, 2015). Since deglaciation proceeds at quicker rates for glaciers than for permafrost (Haerberli *et al.*, 2016), valley glaciers are expected to lose their key role of hydrological drivers in Alpine catchments over the next decades. Rock glacier outflows might become increasingly important in deglaciating Alpine areas, especially in the forecasted enhanced precipitation stochasticity (Milner *et al.*, 2009) and earlier summer snowmelt (Stewart, 2009). Water origin is fundamental for shaping the hydroecology of Alpine streams, since it determines the geomorphological, physical and chemical conditions that influence biotic communities (Ward, 1994; Brown *et al.*, 2003). Even if little studied so far, rockglacier-fed streams are characterized by distinctive habitat conditions (Mair *et al.*, 2015; Colombo *et al.*, 2017), and thus they can potentially host peculiar biotic communities.

This study aims at identifying key habitat characteristics of rock glacial streams. The study area is located in the Solda valley (Ortles-Cevedale massif, Italian Alps), with sampling stations in the upper Solda and Zay subcatchments (2105-2833 m a.s.l.) draining metamorphic gneiss bedrocks (Province of Bolzano, 2017). We compared the physical and chemical features (Table 1) of 7 streams with different water source (2 fed by rockglacier, 2 by groundwater, 2 by glacier, 1 with mixed source), sampled in June, August, and September 2017.

Table 1. List of habitat variables used in the analysis

Habitat feature	Variables
Water origin	$\delta^2\text{H}$, $\delta^{18}\text{O}$ stable isotopes
Channel instability	Pfankuch index (Bottom component)
Physical parameters	Turbidity, Temperature
Anions and cations	Electrical conductivity, Ca, Mg, SO ₄ , SiO ₂
Nutrients	NO ₃ , PO ₄ , DOC
Trace elements	Al, As, Ba, Pb, Cd, Fe, Mn, Sr, U, Zn

Research aims and methods

Water origin was verified by analyzing $\delta^2\text{H}$ and $\delta^{18}\text{O}$ in stream waters using mixing models with snowmelt, precipitation, and glacier ice melt as potential end-members. A Principal Component Analysis (PCA) was applied to the environmental variables of all samples collected in summer 2017. The same method was applied only to trace elements.

Results and discussion

Temperature profiles (measured with dataloggers) showed only very small diel oscillations for both rock glacial streams, compared to the other stream types.

The Solda rock glacial stream (SRG) was separated from all the other stations (Fig. 1) based on its clear waters ($\text{NTU}<3$), low temperatures ($<1.2^\circ\text{C}$), stable channel ($\text{PFAN}=19$), higher electrical conductivity ($376\text{--}630\ \mu\text{S cm}^{-1}$) and Ca ($47.5\text{--}73.5\ \text{mg L}^{-1}$), Mg ($12.5\text{--}15\ \text{mg L}^{-1}$), PO_4 ($3.8\text{--}5\ \mu\text{g L}^{-1}$) and SO_4 ($107.3\text{--}170\ \text{mg L}^{-1}$) concentrations, which increased over summer. The Zay rock glacial stream (ZRG) resembles the mixed origin station (Fig. 1). This is likely due to the infiltration of glacial waters into the upstream rock glacier margin (personal observation), thus smoothing the permafrost signal. Glacier-fed streams are characterized by high seasonality, with higher turbidity ($\text{NTU}=43\text{--}132$) and lower conductivity ($\text{EC}=9\text{--}72\ \mu\text{S cm}^{-1}$) in June and August than in September ($\text{EC}=79\text{--}270\ \mu\text{S cm}^{-1}$, $\text{NTU}=32\text{--}60$), when flow was almost exclusively subglacial, due to the low air temperatures.

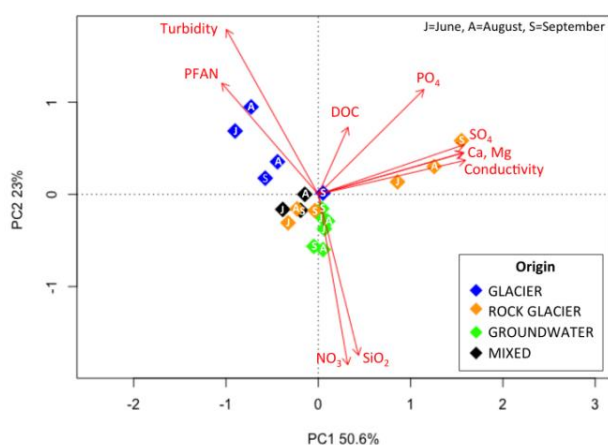


Figure 1. PCA biplot of habitat variables of the streams sampled in summer 2017.

Temperature profiles along with results for trace elements, and $\delta^2\text{H}$ and $\delta^{18}\text{O}$ isotopes, currently under analysis, will be shown in the presentation.

Conclusions

Our results show that rockglacial streams, in agreement with information in literature, represent peculiar habitats, according to a set of physical and chemical parameters. However, the similarity of Zay rock glacial stream with non-glacial streams underscores that hydrological complexity must be taken in consideration when assessing the hydroecological peculiarity of rock glacier fed headwaters. These results confirm that rockglacier fed streams deserve more attention in relations to effects of global warming on Alpine hydrology.

Acknowledgments

This work was carried out within the Erasmus Mundus Joint Doctorate Program SMART (Science for the Management of Rivers and their Tidal Systems) funded with the support of the EACEA of the European Union. We thank Werner Tirlir and Giulio Voto at EcoResearch I.t.d. (Bolzano) for trace element analyses.

References

- Brown, L. E., Hannah, D. M. & Milner, A. M., 2003. Alpine stream habitat classification: an alternative approach incorporating the role of dynamic water source contributions. *Arctic, Antarctic and Alpine Research*, 35(3): 313-322.
- Colombo, N., Salerno, F., Gruber, S., Freppaz, M., Williams, M., Fratianni, S. & Giardino, M., 2017. Impacts of permafrost degradation on inorganic chemistry of surface fresh water. *Global and Planetary change*, accepted
- Haeberli, W., Schaub, Y. & Huggel, C., 2016. Increasing risks related to landslides from degrading permafrost into new lakes in de-glaciating mountain ranges. *Geomorphology*, 293: 405-417.
- Mair V., Lang K., Tonindandel D., Thaler B., Alber R., Lösch B., ... Tolotti M., 2015. *Progetto Permaqua – Permafrost e il suo effetto sul bilancio idrico e sull'ecologia delle acque di alta montagna*. Provincia Autonoma di Bolzano, Bolzano, Italy: Ufficio geologia e prove dei materiali.
- Milner, A. M., Brown, L. E. & Hannah, D. M., 2009. Hydroecological response of river systems to shrinking glaciers. *Hydrological Processes*, 23 (1): 62–77
- Provincia di Bolzano, 2017. Carta Geologica d'Italia 1:100000 layer. Online Geobrowser
- Stewart, I. T. (2009). Changes in snowpack and snowmelt runoff for key mountain regions. *Hydrological Processes*, 23 (1): 78–94.
- Ward, J. V. (1994). Ecology of alpine streams. *Freshwater Biology*, 32(2): 277–294.



High frequency data reveals new insights into hydrological and biogeochemical processes in a discontinuous permafrost watershed

Sean K. Carey¹
Nadine J. Shatilla¹
Weigang Tang¹

¹*School of Geography and Earth Sciences, McMaster University, Hamilton, ON, Canada, careysk@mcmaster.ca*

Abstract

Conceptual models of alpine watersheds underlain with permafrost have developed over the last 50 years based on careful field measurements and observations. Furthermore, the importance of permafrost soils in catchment biogeochemistry has more recently received scrutiny. In recent years, new water quality sensors (fluorimeters, multi-parameter sondes) provide an opportunity to both test and enhance our understanding of coupled water and biogeochemical cycling in headwater systems. In this paper, multi-year multi-parameter high frequency data sets from the Wolf Creek Research Basin, Yukon, Canada, will be utilized to assess the influence of active layer development, permafrost and seasonality on runoff generation processes and catchment connectivity. We utilize 15-minute salinity and coloured dissolved organic matter (CDOM) measurements to generate seasonal and event-based hysteresis loops with discharge. The magnitude and direction of these loops reflects flow pathways and wetness-induced catchment connectivity.

Keywords: Hydrology; alpine environments; discontinuous permafrost; runoff generation; high-frequency data.

Introduction

The influence of permafrost, active layer development and frozen ground on runoff hydrology has been well characterized with decades of research (Woo, 2012). Permafrost acts as an aquitard, whereas the seasonal development of the active layer is an important control on runoff pathways (Carey & Woo, 2001). As the active layer develops, relatively deeper and slower runoff pathways predominate, affecting both the rate and volume of runoff along with stream chemical signatures. In areas with discontinuous permafrost, there is considerable variability in hydrological processes due to the partitioning between relatively rapid near-surface runoff processes and deeper drainage.

Over the past decade, there has been an advancement of in-stream instrumentation that allow high-frequency measure of water quality parameters (e.g. temperature, salinity, pH, coloured dissolved organic matter (CDOM)). Considering that stream chemistry in headwater alpine watersheds is largely a reflection of terrestrial hydrological processes and water-soil-rock interaction, an opportunity exists to advance our understanding of these systems through new data.

The objective of this paper is to utilize high frequency (15-minute) discharge (Q), salinity (SpC) and CDOM data to assess whether water quality information can

provide additional insights into runoff generation processes. This will be completed by examining hysteresis in Q-SpC and Q-CDOM at seasonal and event time scales.

Study Site and Methods

Study site

Granger Basin (60°31'N, 135°18'W) is a 7.6 km² headwater catchment located within the long-term Wolf Creek Research Basin, Yukon Territory, Canada. Granger Basin ranges in elevation from 1,310 to 2,250 masl and has a continental subarctic climate with mean annual precipitation ~400 mm (40% snow) and a mean annual temperature of -3°C. The geology is primarily sedimentary overlain by a glacial till and ~70% of the basin is underlain with permafrost (Lewkowicz & Ednie, 2004), with low-elevation southerly exposures permafrost-free. Vegetation consists of low-lying grasses, herbs and shrubs such as dwarf birch and willow (McCartney *et al.*, 2006).

Field methods

For this paper, 15-minute data from 2016 is analyzed throughout the ice-free season. Discharge was calculated using a stage-discharge relationship. Salinity was measured using a Hobo U24 conductivity logger and corrected for temperature. CDOM was collected using a Turner C3 submersible fluorimeter.

Analysis

The HydRun toolkit (Tang & Carey, 2017) was used to extract rainfall-runoff events from the annual hydrograph and match them with the salinity and CDOM data. Hysteresis indices were calculated after Lloyd et al. (2016).

Results

Seasonal patterns in 2016

Discharge began in early May in response to snowmelt, with two main temperature-driven events, and peaked in mid-June following a large rain event when the active layer was relatively shallow. There is a general seasonal recession with precipitation event responses and an increase in flows beginning in late August when conditions were very wet (Figure 1). SpC in general declined when flows increased, yet as the season progressed, there is an overall decline in SpC for any given Q (Figure 2). CDOM was greatest in early spring and declined throughout the season, yet increased when flows rose in response to precipitation. There were periods when both SpC and CDOM were not measured because of instrument problems.

Figure 1. Runoff, specific conductance and CDOM for Granger Basin, 2016

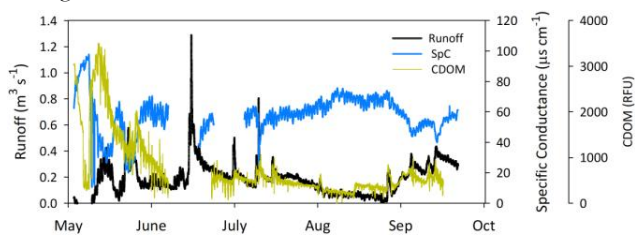


Figure 2. Runoff versus specific conductance at 15 minute intervals for Granger Basin in 2016.

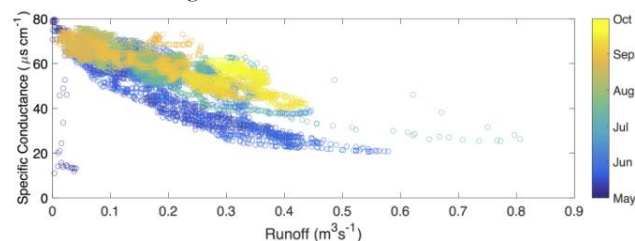
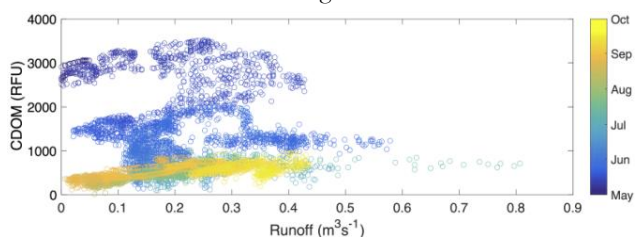


Figure 3. Runoff versus CDOM (relative fluorescence units) at 15 minute intervals for Granger Basin in 2016.



Event delineation and hysteresis Loops

The HydRun toolkit extracted 16 distinct runoff events in 2016 that had Q-SpC pairs. Of the Q-SpC events, 12 were clockwise (CW), 3 were counter-

clockwise (CCW) and 1 was unresolvable. For the Q-CDOM events, 4 were CW, 10 were CCW and 2 were unresolvable. There were no distinct seasonal patterns to the direction and the openness of the loops.

Discussion

High frequency water quality data provides new insight into runoff generation processes in Granger Basin. There is a strong seasonal increase in conductivity for given flows superimposed on the high-frequency hysteresis (Figure 2). This seasonal increase in SpC is a result of deeper runoff pathways later in the season as the active layer thickens connecting to the stream and greater opportunity for water-soil contact. The general clockwise hysteresis for Q-SpC curves indicates lower salinity on the falling limb of the hydrograph and some dilution, however it is more likely that this reflects water reporting from more dilute near-surface horizons later in the event. Q-CDOM shows a strong seasonal clockwise pattern with distinct CCW event patterns. As a proxy for dissolved organic matter, this represents a general flushing throughout the year. However, on event time scales, CDOM CCW loops indicate a rise after the peak Q, which at event scales does not suggest a flushing but a mobilization mechanism. It is important to note that the loops for Q-CDOM are less well defined than the Q-SpC loops highlighting the complexity of DOM dynamics.

Acknowledgments

We wish to acknowledge funding through the Natural Sciences and Engineering Research Program, the Changing Cold Regions Research Network, and Yukon Environment, Water Resources for logistical support.

References

- Carey, S.K. & Woo, M-K., 2001. Slope runoff processes and flow generation in a subarctic, subalpine catchment. *Journal of Hydrology* 253: 110-119.
- Lewkowitz, A.G. & Ednie, M., 2004. Probability mapping of mountain permafrost using the BTS method, Wolf Creek, Yukon Territory, Canada. *Permafrost and Periglacial Processes* 15: 67-80.
- McCartney, S., Carey, S.K., & Pomeroy, J.W., 2006. Intra-basin variability of snowmelt water balance calculations in a subarctic catchment. *Hydrological Processes* 20: 1001-1016.
- Tang, W. & Carey, S.K., 2017. HydRun: A MATLAB toolbox for rainfall-runoff analysis. *Hydrological Processes* 31: 2670-2682.
- Woo, M-K., 2012. *Permafrost Hydrology*. Springer 563 pp.



Monitoring the Hydrogeochemical Evolution of Groundwater in a Small Watershed in a Discontinuous Permafrost Zone, Québec, Canada

Marion Cochand¹
John Molson²
Johannes A.C. Barth³
Robert van Geldern³
Jean-Michel Lemieux²
Richard Fortier²
René Therrien²

¹ *Département de géologie et de génie géologique et Centre d'études Nordiques, Université Laval, Québec, QC, Canada, marion.cochand.1@ulaval.ca*

² *Département de géologie et de génie géologique et Centre d'études nordiques, Université Laval, Québec, QC, Canada*

³ *GeoZentrum Nordbayern, Friedrich-Alexander-Universität Erlangen-Nürnberg, Germany*

Abstract

In northern regions such as Nunavik, Québec, Canada, the impacts of climate change are already apparent. However, the impacts of climate warming and permafrost degradation on groundwater dynamics and quality are still not well understood. This study aims to improve our understanding of hydrogeological interactions in degrading permafrost environments using hydrogeochemical characterization of groundwater. A small 2-km² catchment in a discontinuous permafrost zone close to the Inuit community of Umiujaq, on the eastern shore of Hudson Bay in northern Québec, Canada, was studied using hydrogeochemical tracers. Major ions, water stable isotopes, dissolved and particulate carbon, their stable carbon isotopes, and dating tracers were analyzed in order to characterize groundwater in this changing environment. The results have provided a better understanding of groundwater origin, evolution and residence time in the catchment. Linking this hydrogeochemical characterization to numerical modelling of groundwater flow and heat transfer at the watershed and permafrost mound scales is improving our knowledge on hydrogeological interactions in degrading permafrost environments.

Keywords: Groundwater hydrogeochemistry; permafrost; climate change; cold regions hydrogeology.

Introduction

One consequence of global warming already being felt in northern Québec (Canada) is permafrost degradation. Although its influence on groundwater resources is still largely unknown, it will probably lead to increased groundwater recharge and changing flow dynamics (Michel & Van Everdingen, 1994; Quinton & Baltzer 2013). This study aims to improve knowledge on changing hydrogeological conditions in degrading permafrost environments using hydrogeochemical characterization of groundwater.

Study site

This study is being conducted in a small 2-km² watershed, located close to Umiujaq, on the eastern shore of Hudson Bay in northern Québec, Canada, in the discontinuous permafrost zone.

Two aquifers are currently being investigated using monitoring wells: 1) an unconfined shallow sandy

aquifer located in the upper part of the watershed, and 2) a deeper confined aquifer in sands and gravels located below silty sediments invaded in part by permafrost (Fig. 1) (Lemieux et al., 2016).

Results and Interpretation

Groundwater, precipitation, stream and surface water as well as ice-rich permafrost were sampled during field investigations from 2013 to 2016 and were analyzed for major ions, water and carbon stable isotopes, carbon phases and tritium.

Results indicate that groundwater has a Ca-HCO₃ composition with a low total dissolved solids content, typical for young and poorly-evolved water, and tritium values are close to 8.5 TU. Groundwater evolution can be explained by short residence times (evidence of modern recharge with tritium data), slow reaction rates due to the cold environment as well as low levels of dissolved CO₂ (low organic soils with PCO₂= 10^{-2.5} atm

(Clark & Fritz, 1997)). Dissolved inorganic carbon (DIC) Dissolved organic carbon concentrations are very low in groundwater and have a $\delta^{13}\text{C}$ signature typical of C3-type vegetation.

Stream chemical composition is influenced by groundwater exfiltration at the base of permafrost mounds in the lower part of the watershed. DIC and its $\delta^{13}\text{C}$ signature provide evidence of CO_2 degassing along the stream.

Ice lenses in permafrost have a water stable isotope composition close to modern precipitation and groundwater. This could indicate that the groundwater feeding the ground ice formation during permafrost aggradation was similar to modern groundwater and/or that permafrost warming-cooling cycles have drawn modern water into the permafrost mounds.

Conclusions

This study has allowed delineating groundwater evolution in a catchment containing discontinuous permafrost in Nunavik, Québec, Canada. Using various hydrogeochemical tracers, groundwater appears to be young and relatively poorly evolved. Tracers also highlight that the stream is fed by groundwater discharge at the base of permafrost mounds. Isotopic signatures of ice-rich permafrost lenses down to five meters deep are close to modern groundwater, which suggests influence of modern water. Linking this hydrogeochemical characterization to groundwater and thermal modelling

can help to improve our knowledge on hydrogeological interactions in degrading permafrost environments

Acknowledgments

The authors acknowledge funding from a NSERC Strategic Project Grant, the Québec Ministry of Sustainable Development, Environment and Fight against Climate Change (MDDELCC) and the Québec Research Fund – Nature and Technology (FRQNT). We also thank the local community of Umiujaq for their help and collaboration on this project.

References

- Clark, I. D. & Fritz, P., 1997. *Environmental Isotopes in Hydrogeology*. CRC Press.
- Lemieux, J.-M., Fortier, R., Talbot-Poulin, M.-C., Molson, J., Therrien, R., Ouellet, M., Banville, D., Cochand, M. and Murray, R., 2016. Groundwater occurrence in cold environments: examples from Nunavik, Canada. *Hydrogeology Journal* 24, 1497-1513.
- Michel, F. A. & Van Everdingen, R. O., 1994. Changes in hydrogeologic regimes in permafrost regions due to climatic change. *Permafrost and Periglacial Processes*, 5(3), 191–195.
- Quinton, W. L. & Baltzer, J. L., 2013. The active-layer hydrology of a peat plateau with thawing permafrost (Scotty Creek, Canada). *Hydrogeology Journal*, 21, 201–220.

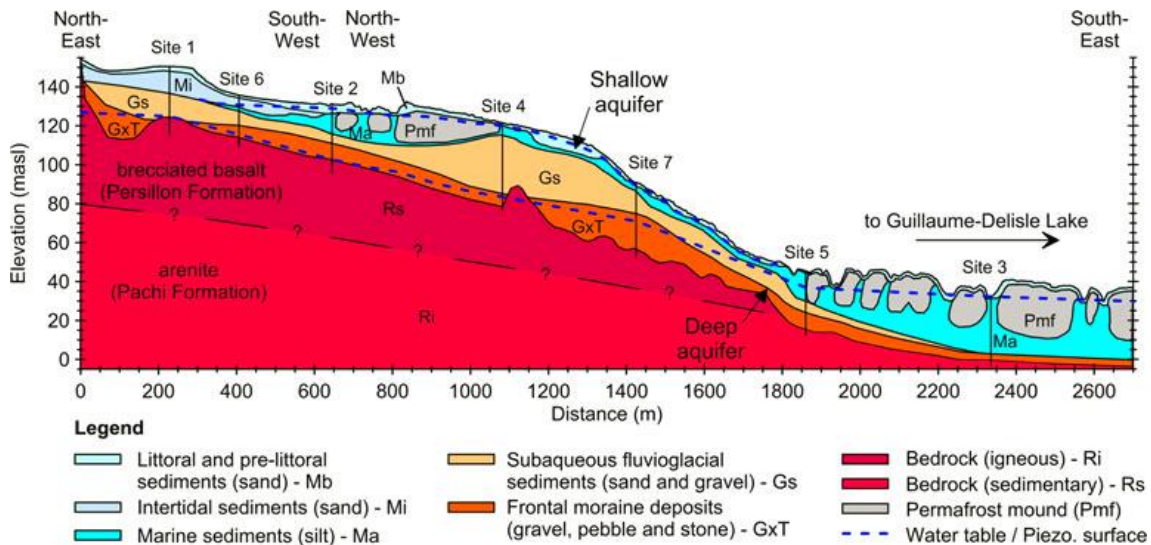


Figure 1: Cross-section of the study site showing the sampling sites, deep and shallow aquifers, the Quaternary sediments and the geology (Lemieux et al., 2016)

New insights into snowfall and snow accumulation trends and patterns across the Northwest Territories

Connon, R.F.¹, Coles, A.E.¹, Kokelj, S.A.², and Quinton, W.L.¹

¹Wilfrid Laurier University, Yellowknife, NT, rfconnon@gmail.com

²Environment and Natural Resources, Government of the Northwest Territories, Yellowknife, NT

Abstract

It is unclear whether snow water equivalent (SWE) in the Northwest Territories of Canada has changed in the past several decades in response to climate warming. This is in part due to the paucity of continuous, long-term snow water equivalent (SWE) datasets in the region. Further, there appear to be inconsistent long-term precipitation trends, depending on the use of adjusted SWE data, non-adjusted SWE data, or snowpack accumulation data. Accurate snowfall and snow cover data are important for parameterizing hydrological and permafrost distribution models. It is suggested that errors in snow depth calculations are artificially inflating adjusted SWE values, such as shown here for Fort Simpson, NWT - one of the few long-term climate stations in the territory. On the ground historical (1980 – present) snow survey data are used to demonstrate the spatial distribution of SWE across the NWT.

Keywords: Snow, SWE, Permafrost

Introduction

Climate warming in northwestern Canada is occurring at one of the fastest rates on Earth. There is significant uncertainty as to how climate warming may affect snow accumulation, redistribution and melt patterns in this region (Shi *et al.*, 2015). Quantifying total end-of-winter snow-water equivalent (SWE) is important for anticipating spring water level conditions and annual water balance computations in this area dominated by nival regime hydrology. Understanding how (and if) snowfall is changing is also necessary to parameterize hydrological models to predict future streamflow under different warming scenarios. Furthermore, given that snowfall is an effective insulator of permafrost, understanding and predicting the timing and magnitude of snow accumulation is essential to anticipate future permafrost conditions. In the Northwest Territories (NWT), there is a lack of long term, spatially distributed snow measurements. As a result, there is often a reliance on adjusted and/or gridded data when trying to forecast future conditions. Widely used adjusted datasets may show poor agreement with ground-based measurements (*i.e.* snow surveys), in part arising from the small number of measurement stations. The objectives of this study are to: 1) synthesize and assess various sources of snowfall data and trends from across the NWT; and 2) to compare the findings to a comprehensive analysis of end-of-season SWE based on historic ground survey data.

Methodology

Where available, the Environment and Climate Change Canada (ECCC) Adjusted and Homogenized SWE datasets (Mekis and Vincent, 2011) were compared to gauged precipitation data and ground-based snow measurements across the NWT to assess if this dataset is a valid representation of field conditions. These trends were also compared against trends from GlobSnow, a satellite-based daily SWE product from which end-of-season SWE was derived.

To facilitate trend analysis of long-term datasets, the ECCC adjusted SWE data is calculated by:

$$SWE = D \times \rho_{\text{fresh}} \times \rho_{\text{swe}}$$

where: SWE (m); D is snow depth (m); ρ_{fresh} is the assumed density of fresh snow (100 kg m⁻³); and ρ_{swe} is the spatially-variable SWE adjustment factor. This calculation is dependent on snow depth data and uses a constant snow density. However, beginning in the mid-1960s, weighing precipitation gauges were implemented at ECCC climate stations, providing a direct measure of SWE. Here, we use the non-parametric Mann-Kendall test to compare the Adjusted SWE dataset against gauged SWE data in the NWT.

This study also analyses long-term, historical on the ground snow survey data collected by academic and government institutions. Typically, the snow survey data were obtained by measuring snow depth with a wooden ruler and/or a depth-integrated snow density using a snow tube and calibrated SWE scale.

Results

The data presented here are from Fort Simpson, NWT, located on the southern edge of discontinuous permafrost. Fort Simpson climate records span over 100 years (1898 – present). Over the available 114-year record, the adjusted dataset indicates that SWE is significantly increasing ($p < 0.001$) at a rate of 12 mm/decade, however the non-adjusted dataset increases at a significant ($p = 0.03$) rate of only 3.5 mm/decade (Figure 1).

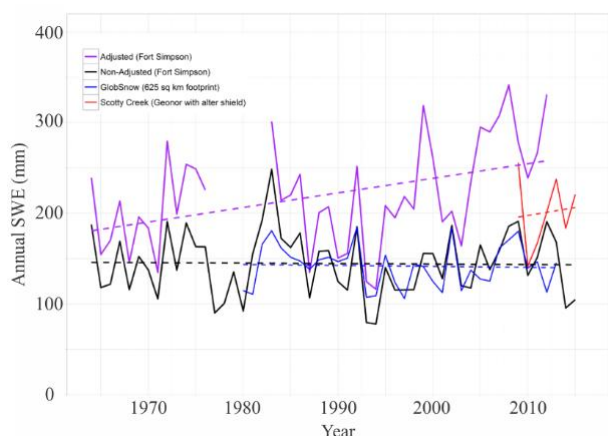


Figure 1. Differences between annual SWE measured near Fort Simpson, NWT.

The station was re-located in 1964, after which the adjusted dataset shows significant increases ($p < 0.001$) of 17.9 mm/decade, whereas the non-adjusted dataset decreases at a non-significant ($p = 0.356$) rate of 0.5 mm/decade. The GlobSnow dataset (1980 – present) displays similar trends to the non-adjusted data and also has a small, non-significant ($p = 0.339$) decreasing trend of 2.7 mm/decade (Fig 1).

Recent annual SWE values in the adjusted dataset have also been much higher than those measured on the ground. For example, during a high snowfall year in 2008, total adjusted SWE was 342 mm, whereas non-adjusted SWE was 186 mm, GlobSnow SWE was 171 mm and SWE measured on the ground at Scotty Creek was 176 mm.

It is suggested that the large differences in SWE are the result of errors in depth measurements originating after 1995. Prior to 1995, the depth measurements and non-adjusted SWE measurements approximated the 10:1 ratio, where 10 mm of fresh snow equals approximately 1 mm of SWE. However, after 1995, the relationship is no longer clear (Fig 2) and snow depths appear to be exaggerated. It is proposed that this is likely due to the change to an automated snow depth instrument (*i.e.* SR50, *Campbell Scientific*) that is not

recording accurate data. A similar trend was found at the Hay River climate station, where a strong increasing trend in SWE was observed in the adjusted dataset, without a concomitant increase in the non-adjusted or GlobSnow datasets. Ongoing work will be conducted to analyze trends at other stations in the NWT, as well as to use on the ground snow survey data to compile a comprehensive data set for SWE across the territory.

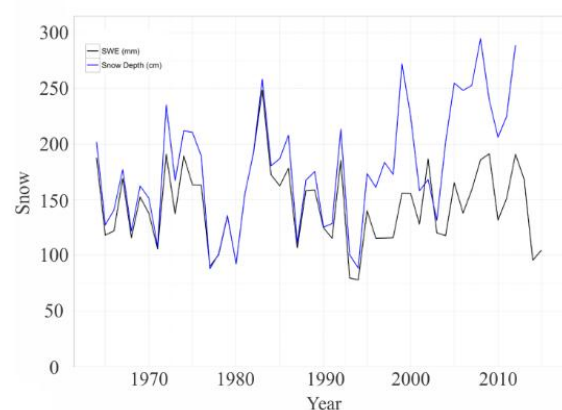


Figure 2. Comparison of snow depth (cm) and SWE (mm) at Fort Simpson A climate station.

Conclusions

It appears that the adjusted and homogenized SWE data for some climate stations in the NWT suggest increasing trends that are not corroborated with on the ground observations. It is important to accurately characterize these trends to:

- 1) Predict how spring runoff events will change under different warming scenarios
- 2) Calculate over-winter energy loss from permafrost systems, given that snow is a very effective insulator.

References

- Mekis, E., and Vincent, L. 2011. An overview of the second generation adjusted daily precipitation dataset for trend analysis in Canada, *Atmos-Ocean*, 49:2, 163-177.
- Shi, X., Marsh, P., and Yang, D. 2015. Warming spring air temperatures, but delayed spring streamflow in an Arctic headwater basin, *Environ. Res. Lett.*, 10, 1-10.



Quantifying the Interactions Between Subsurface Hydro-Thermal Characteristics, Permafrost Distribution, Soil Physical Properties and Landscape Structure in an Arctic Watershed

Baptiste Dafflon¹, Emmanuel Léger², Yves Robert², John Peterson², Craig Ulrich², Sébastien Biraud², Anh Phuong Tran², Bhavna Arora², Haruko Wainwright², Vladimir Romanovsky³, Susan Hubbard²

¹Lawrence Berkeley National Laboratory, Berkeley California, bdafflon@lbl.gov

²Lawrence Berkeley National Laboratory, Berkeley California

³University of Alaska Fairbanks, Fairbanks Alaska

Abstract

Understanding the link between soil physical properties (incl. fraction of soil constituents, bedrock depth, permafrost characteristics), thermal behavior, hydrological conditions and landscape properties is particularly challenging yet is critical for predicting the storage and flux of water, carbon and nutrient in a changing climate in the Arctic permafrost environment. In this study we investigate the characteristics of and controls on deep permafrost processes in a watershed on the Seward Peninsula AK. A variety of ground-based and aerial measurements are integrated together to identify the various subsurface hydro-thermal behavior in the watershed and to evaluate the multi-dimensional relationships between subsurface and surface properties. The various datasets allow us to distinguish shallow permafrost from deep permafrost with overlying talik. In addition, several interactions are identified between the subsurface permafrost/soil characteristics, the topography and the snow thickness and plant distribution. We use numerical models to reproduce some of the identified behavior.

Keywords: Permafrost; Talik, Discontinuous; Geophysics; Hydrology; Co-variability.

Introduction

Improving understanding of Arctic ecosystem functioning and parameterization of process-rich hydro-biogeochemical models require advances in quantifying ecosystem properties, from the bedrock to the top of the canopy (Jorgenson et al., 2010). In Arctic regions having significant subsurface heterogeneity, understanding the link between soil physical properties (incl. fraction of soil constituents, bedrock depth, permafrost characteristics), thermal behavior, hydrological conditions and landscape properties is particularly challenging yet is critical for predicting the storage and flux of water, carbon and nutrient in a changing climate. In this study we investigate the distribution of various hydro-thermal behavior in an Arctic watershed with discontinuous permafrost, and we investigate the relationships between the subsurface soil properties and the landscape structure.

Field Site and Data

This study, which is part of the Next Generation Ecosystem Experiment (NGEE-Arctic), takes place in a

watershed between Nome and Teller AK on the Seward Peninsula. The watershed is characterized by an elevation gradient, shallow bedrock, and discontinuous permafrost. At this site, the top of permafrost cannot be easily identified with a tile probe (due to rocky soil and/or large thaw layer thickness). As such, we developed a technique using vertically resolved thermistor probes to directly sense the temperature regime at multiple depths and locations (Fig. 1). These measurements complement electrical resistivity tomography imaging, seismic refraction and point-scale data for identification of the various thermal behavior and soil characteristics. In addition, we used a Unmanned Aerial Vehicle (UAV)-based aerial imaging platform to measure surface properties including a digital surface model (DSM), the plant distribution and vigor, and the estimation of snow thickness (e.g., Wainwright et al., 2017). The surveys are performed at a 150 x 300 m scale to understand the interactions between a shallow permafrost zone and surrounding deeper permafrost, as well as along long 2 km long transects from the bottom to the top of the watershed to understand watershed-scale permafrost and hydrological characteristics. Finally, we also initiated the monitoring

of the co-variability between surface and subsurface properties along a 130 m long transect using a coincident above/below ground monitoring strategy following the approach developed earlier at another Arctic site (Dafflon et al., 2017).

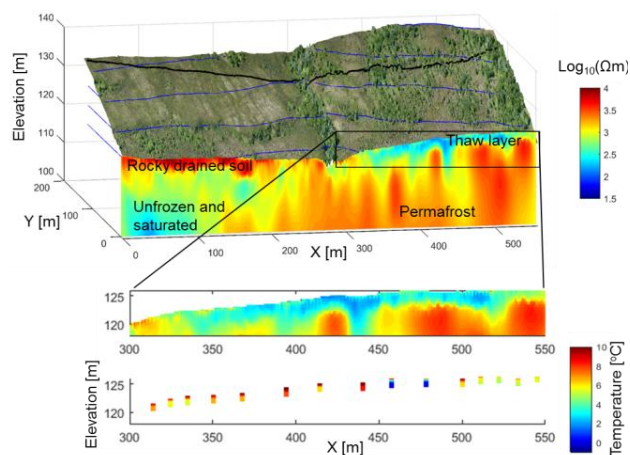


Figure 1. (top) Electrical Resistivity Tomography (ERT) and UAV-inferred mosaic and digital surface elevation model. (bottom) Zoom in of shallow ERT and vertically resolved temperature profiles. Presence of unfrozen channels observed from ERT is confirmed by higher soil temperature values.

Method

A statistical data analysis is performed to understand the multi-dimensional relationships between the various subsurface and surface properties. In particular, we evaluate linkages between the soil physical-thermal properties and the surface hydrological conditions, geomorphic characteristics, snow thickness and vegetation distribution. The data integration and analysis is supported by numerical approaches that simulate hydrological and thermal processes. Various scenarios are simulated to evaluate and explain various hydrological-thermal behavior observed in the field data.

Results and Discussion

Results show significant spatial co-variability between permafrost characteristics, vegetation, and geomorphology (ie, between above-, at- and below-ground characteristics). The permafrost distribution influences the distribution of shallow soil moisture and the geometry of surface and subsurface drainage paths. The transition zones between shallow and deeper or no permafrost zones show sharp changes in thermal behavior involving very distinct trends in vertically resolved soil temperature profiles and strong lateral

variations over a few meters. We observe association between various thermal behaviors and hydrological conditions, as well as soil properties and vegetation types. Potential preferential flow paths in the subsurface have also been identified.

Further, winter subsurface thermal behaviors show the presence of taliks at several locations and potentially year-round flow and transport with highest accumulation of unfrozen water at the bottom of hillslope. Numerical models parameterized based on the field data enable us to investigate various conceptual model and improve the understanding of the present and future of such system.

Overall, this study illuminates the watershed structure and the interactions between various subsurface and landscape properties in a representative Arctic watershed with discontinuous permafrost. These interactions are of significant interest, as they are critical for understanding the evolution of the landscape and the permafrost distribution. The obtained information is expected to be useful for improving predictions of Arctic ecosystem feedbacks to climate.

Acknowledgments

The Next-Generation Ecosystem Experiments (NGEE Arctic) project is supported by the Office of Biological and Environmental Research in the DOE Office of Science. This NGEE-Arctic research is supported through contract number DE-AC0205CH11231 to Lawrence Berkeley National Laboratory. The authors thank Drs. C. Ruecker and T. Guenther for providing 2D complex resistivity imaging codes, and the NGEE PI Dr. S. Wulschleger for his support.

References

- Dafflon, B.; Oktem, R.; Peterson, J.; Ulrich, C.; Tran, A. P.; Romanovsky, V.; Hubbard, S. S., 2017. Coincident aboveground and belowground autonomous monitoring to quantify covariability in permafrost, soil, and vegetation properties in Arctic tundra. *Journal of Geophysical Research: Biogeosciences*, 122 (6), 1321-1342.
- Jorgenson, M. T.; Romanovsky, V.; Harden, J.; Shur, Y.; O'Donnell, J.; Schuur, E. A. G.; Kanevskiy, M.; Marchenko, S., 2010. Resilience and vulnerability of permafrost to climate change. *Canadian Journal of Forest Research-Revue Canadienne De Recherche Forestiere*, 40 (7), 1219-1236.
- Wainwright, H. M.; Liljedahl, A. K.; Dafflon, B.; Ulrich, C.; Peterson, J. E.; Gusmeroli, A.; Hubbard, S. S., 2017. *Mapping snow depth within a tundra ecosystem using multiscale observations and Bayesian methods*. The Cryosphere, 11 (2), 857-875.



Taliks, a tipping point in permafrost degradation

Élise Devoic¹
James R. Craig¹
William L. Quinton²
Ryan F. Connon²
Erfan A. Amiri¹

¹University of Waterloo, Waterloo, ON, egdevoie@uwaterloo.ca

²Wilfrid Laurier University, Waterloo, ON

Abstract

Permafrost thaw is modelled in peatlands in the discontinuous permafrost region in northern Canada using a 1-D thermodynamic model of annual freeze-thaw cycles. The effects of thermal conductivity, soil moisture, advection, and snow cover are considered when modelling overwinter re-freeze depths. Conditions are identified under which insufficient energy is removed from the system to re-freeze the soil column entirely, forming a confined talik between the active layer and the permafrost table. These conditions are found to be very similar to measured soil conditions at Scotty Creek, NWT. The modelled data is compared to field measurements, and is used to determine the relative contribution of various factors to permafrost thaw, as well as quantifying anticipated thaw rates in different parts of the landscape. The model is easily extended to mineral soil systems to make predictions elsewhere.

Keywords: Permafrost; Climate Change; Hydrology; Modelling; Active Layer Evolution.

Introduction

Rapid climate warming in northern Canada is resulting in permafrost loss (Payette *et al.*, 2014). At the southern limit of permafrost, thaw is observed in peatlands as a loss in extent of permafrost-supported peat plateau (Quinton *et al.*, 2011). The precursor to loss of permafrost is proposed to be linked to the formation of confined taliks. Sub-active layer taliks form when the net ground heat flux is positive, i.e. more energy is gained by the soil during the summer than can be lost through the winter. Under these conditions, the entire soil column is unable to refreeze, and a thawed region is left between the base of the active layer and the top of the frozen permafrost table (Connon *et al.*, 2018). The presence of this talik affects the hydrology of the system, especially over winter when the system was historically quiescent. More importantly in this context, the formation of taliks is thought to be a tipping point in permafrost thaw.

Methodology

A one-dimensional thermodynamic model of active layer evolution in saturated porous media including conductive, sensible, and latent heat has been developed. This model is used to simulate soil columns initially with and without a confined talik. Annual freeze-thaw cycles are applied to these hypothetical soil columns for several possible climate scenarios, and soil conditions, to determine the evolution of the soil columns with and

without a talik. Results are compared to representative talik characterization data collected from the Scotty Creek Research Station (SCRS), located in discontinuous permafrost peatlands of the southern Northwest Territories, Canada.

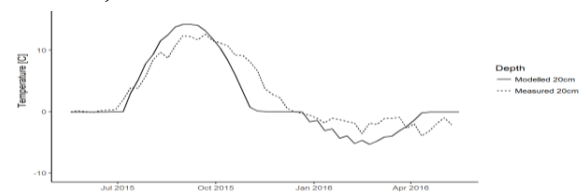


Fig. 1: Measured and modelled soil temperature

Results

Simulated soil temperatures determined by a representative boundary heat flux at the surface are compared to field data collected at SCRS. The stable ground heat flux condition is generally consistent with observed soil temperatures, but deviates in the winter months. A comparison of modelled and measured soil temperatures at a depth of 20cm is shown in Fig. 1. The summer soil temperature is relatively well represented, however the timing of thaw progression through the soil profile as well as the over-winter temperature are not, resulting in an over-estimation of refreeze depths. This is expected since hypothetical net ground heat flux was used to force the simulation instead of measured data.

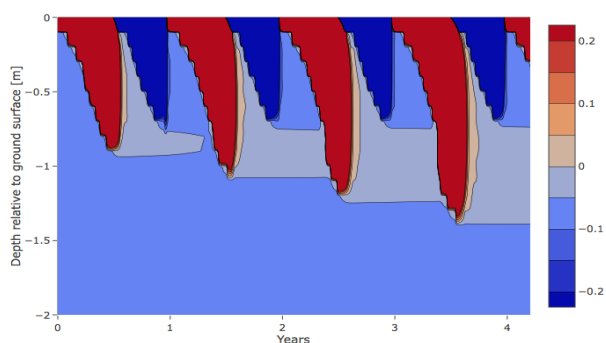


Figure 2: Talik formation under observed ground heat flux

Thermal conductivity, unsaturated soil and changes in snow cover are investigated as factors influencing depth of thaw and refreeze, and are compared to field data for various years and soil columns. Model results are sufficiently close to field data to act as a proxy of the system for sensitivity analysis and hypothesis evaluation. Conditions consistent with recently observed soil temperature data result in talik formation in areas with a sparse canopy (Fig. 2). Under soil heat flux conditions consistent with stable permafrost, a system including a talik does not necessarily recover, in fact slight degradation of permafrost can be observed at the base of the soil profile.

Taliks have many impacts on the hydrology, thermodynamics, ecology and topography of the landscape. Taliks can form a conduit for water when they connect adjacent wetland features. This increases the hydrologic connectivity of the landscape, resulting in smaller non-contributing or isolated areas, higher basin outflow (Fig. 3), and increased winter baseflows.

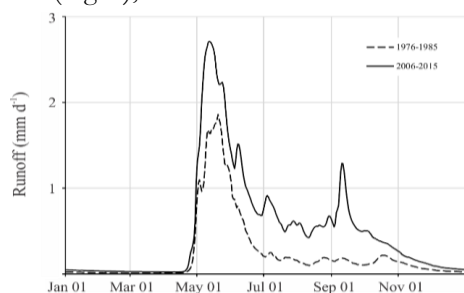


Fig. 3: Increase in streamflow due to increased hydrologic connectivity resulting from permafrost thaw

Water moving through confined talik pathways carries heat energy with it, driving advective thaw, here treated as a heat flux only in the liquid water region. Advective thaw can drastically accelerate permafrost degradation rates, as shown in Fig. 4. These results are used to explain the observed accelerated thaw in field sites with taliks.

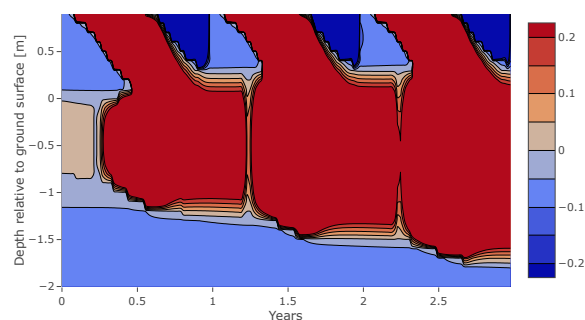


Fig. 4: Accelerated thaw due to advection in connected talik

Taliks are observed in different locations in the field, and serve different functions in each of these locations, as determined by pressure and temperature gradients. Slow-evolving isolated taliks likely act mainly as storage features, and are not subject to advection-driven thaw. Taliks connecting adjacent features can convey water and heat year-round, and may exhibit accelerated thaw. Taliks have been found along the borders of wetland features. Taliks bordering fens can store water throughout the winter, increasing in pressure until thaw occurs, when they drain into the adjacent fen over the course of the summer. Taliks bordering bogs exhibit a gradient reversal over winter, indicating a transition from contributing to receiving storage feature.

Thaw rates adjacent to bogs and fens are estimated from the thermodynamic thaw model using field data. It is found that taliks adjacent to fens are expanding more quickly than those adjacent to bogs. This is validated using historic and current aerial imagery of permafrost extent. Thaw rate data will be used to predict landscape evolution in the discontinuous permafrost peatlands system in future research.

References

- Connon, R.F., Devoie, É., Quinton, W.L., & Hayashi, M., 2018. A thinning active layer in a warming climate. *Journal of Geophysical Research*.
- Payette, S., Delwaide, A., Caccianiga, M., & Beauchemin, M., 2004. Accelerated thawing of subarctic peatland permafrost over the last 50 years. *Geophysical Research Letters*, 31:18.
- Quinton, W. L., Hayashi, M., & Chasmer, L. E., 2011. Permafrost-thaw-induced land-cover change in the Canadian subarctic: Implications for water resources. *Hydrological Processes*, 25:152–158.



Multi-tracer approach for characterizing rock glacier outflow

Michael Engel¹
Stefano Brighenti^{2, 3}
Maria Cristina Bruno³
Monica Tolotti³
Francesco Comiti⁴

¹Free University of Bozen-Bolzano, Italy, Michael.Engel@unibz.it

²University of Trento, Italy

³Fondazione Edmund Mach - Research and Innovation Center, San Michele all'Adige, Italy

⁴Free University of Bozen-Bolzano, Italy

Abstract

The present study used a multi-tracer approach (water stable isotopes, electrical conductivity (EC), and major, minor, and trace elements) to identify the impact of rock glacier outflow on water quality. Springs and streams/creeks fed by rock-glaciers were selected in the Upper Sulden and Zay catchment, South Tyrol (Eastern Italian Alps). Preliminary results indicate that all waters sampled in the study area derived from Atlantic water vapour as water source. Melt waters emerging from rock glaciers showed typical ice melt isotopic signatures ($\delta^2\text{H}$: -91 to -105‰) and relatively high EC (380 to 611 $\mu\text{S cm}^{-1}$). Preliminary results indicate that EC, Sr, and As concentrations could be used to differentiate rock glacier melt waters from stream waters.

Keywords: permafrost thawing; water stable isotopes; heavy metals; ecological communities; alpine rivers; glacierized catchment

Introduction

Current warming in high mountains leads to increased melting of snow, glacier ice and permafrost. In particular rock glaciers, as a common form of mountain permafrost, may release contaminants such as heavy metals into the stream during summer (Thies *et al.*, 2007). Permafrost thawing may have strong impacts on both water quantity and quality of fresh water resources, with potential consequences on alpine stream ecology. However, only few rock glacier studies using multi-tracer approaches were carried out in the Alps. At the regional scale (South Tyrol, Eastern Italian Alps), high concentrations of Ni were found in meltwater from the Lazaun rock glacier in the southern Ötztal Alps (Krainer *et al.*, 2015; Mair *et al.*, 2011) or lake water in contact with Rasass rock glacier in Vinschgau valley (Thies *et al.*, 2007). These observations call for characterizing rock glacier outflows by means of hydrochemical characteristics. For example, Carturan *et al.* (2016) used spring water temperature as significant indicator to identify permafrost distribution.

Material and methods

Study area

The present study was located in the glacierized Sulden catchment (130 km²) in South Tyrol (Italy). The

site ranges in elevation between 1110 and 3905 m a.s.l. and has a glacier extent of about 17.7 km² (14 % of the catchment). Geologically, the study area belongs to the Ortler-Campo-Cristalin (Mair *et al.*, 2007). Permafrost and rock glaciers are most probably present in this region at elevations higher than 2600–2800m a.s.l. (Boeckli *et al.*, 2012). Two active rock glaciers feeding two springs at 2600 m a.s.l. (0.09 km²) were selected in the Upper Sulden in 2015 and one rock glacier at 2718 m a.s.l. (0.08 km²) were chosen in the Upper Zay catchment in 2017, an eastern sub-catchment within the main Sulden stream Valley. Meteorological data were measured by an Automatic Weather Station at 2825 m a.s.l. of the Hydrographic Office (Autonomous Province of Bozen-Bolzano).

Water sampling

Initially, we carried out a monthly sampling of two springs and one stream station as reference draining the rock glaciers in the Upper Sulden catchment from July to October 2015 (Engel *et al.*, 2017a). We resumed the study from June to September 2017 and added the two springs and one stream stations in the Zay sub-catchment. In addition, we sampled potential runoff components such as snowmelt, glacier melt, and precipitation. While all types of melt waters were sampled as grab samples of dripping meltwater from snow patches and the glacier surface, precipitation was

taken from bulk collectors placed in proximity to the rock glaciers.

Water analysis

Electrical conductivity and water temperature were measured by a portable conductivity meter WTW 3410 (WTW GmbH, Germany) with a precision of $\pm 0.1 \mu\text{S cm}^{-1}$ (nonlinearly corrected by temperature compensation at 25 °C). Isotopic analysis was conducted by laser spectroscopy (L2130-i, Picarro Inc., USA) at the Free University of Bozen-Bolzano. Major, minor, and trace elements were analyzed by Inductively Coupled Plasma Mass Spectroscopy (ICP-MS ICAP-Q, Thermo Fischer) at EcoResearch I.t.d. (Bozen).

Results: tracer-based melt water characterization

Results from 2015 show that water from the two springs and the stream in the Upper Sulden catchment fell along the global meteoric water line, indicating Atlantic water vapor as water source. Melt water from rock glaciers showed typical ice melt isotopic signatures ($\delta^2\text{H}$: -91 to -105‰) and relatively high EC (380 to $611 \mu\text{S cm}^{-1}$). Preliminary results indicate that EC, Sr, As and K concentration could be used to discriminate rock glacier melt waters from stream waters for the Sulden sub-catchments in 2015. The important role of EC, Sr, and As as indicators was confirmed in 2017 for spring waters from both sub-catchments. Notably, As concentrations exceeded thresholds for drinking water both in the Sulden and Zay springs from summer to autumn.

Conclusions

The multi-tracer approach based on stable water isotopes, EC, and major, minor, and trace elements proved to be useful to initially characterize rock glacier melt waters in the study area. While isotopic data revealed that all different water types in the catchment derived from Atlantic origin, some hydrochemical parameters (EC, Sr, and As) showed distinct characteristics when comparing rock glacier fed-spring water and reference stream waters (*i.e.* not fed by permafrost). Similarly, these element concentrations also characterized high-elevation spring water in the Matsch Valley, a neighbouring valley of the study area (Engel *et al.*, 2017b). Further work is needed to fully elaborate the tracer dataset obtained and to carry out additional water sampling during the following years, corroborating the present findings.

Acknowledgments

This research is part of the GLACIALRUN project and funded by the foundation of the Free University of Bozen-Bolzano, and part of an Erasmus Mundus Joint Doctorate Program SMART funded by the Education,

Audiovisual and Culture Executive Agency (EACEA) of the European Commission. We thank Werner Tirlir and Giulio Voto at EcoResearch I.t.d. (Bozen/Bolzano) for the element analysis.

References

- Boeckli, L., Brenning, A., Gruber, S., Noetzli, J., 2012. A statistical approach to modelling permafrost distribution in the European Alps or similar mountain ranges. *The Cryosphere* 6: 125-140.
- Carturan, L., Zuecco, G., Seppi, R., Zanoner, T., Borga, M., Carton, A., Dalla Fontana, G., 2016. Catchment-Scale Permafrost Mapping using Spring Water Characteristics. *Permafrost and Periglacial Processes* 27: 253–270.
- Engel, M., Penna, D., Tirlir, W., Comiti, F., 2017a. Tracer-based identification of rock glacier thawing in a glacierized Alpine catchment. *Geophysical Research Abstracts European Geosciences Union*, Vienna, Austria, 23-28 April.
- Engel, M., Penna, D., Tirlir, W., Comiti, F., 2017b. Multi-Parameter-Analyse zur Charakterisierung von Landschaftsmerkmalen innerhalb eines experimentellen Messnetzes im Hochgebirge. *In: M. Casper et al. (Eds.): Den Wandel Messen – Proceedings Tag der Hydrologie 2017, Forum für Hydrologie und Wasserbewirtschaftung* 38: 293-299.
- Kräiner, K., Bressan, D., Dietre, B., Haas, J. N., Hajdas, I., Lang, K., Mair, V., Nickus, U., Reidl, D., Thies, H., Tonidandel, D., 2015. A 10,300-year-old permafrost core from the active rock glacier Lazaun, southern Ötztal Alps (South Tyrol, northern Italy). *Quaternary Research* 83: 324-335.
- Mair, V., Nocker, C., Tropper, P., 2007. Das Ortler-Campo Kristallin in Südtirol. *Mitteilungen der Österreichischen Mineralogischen Gesellschaft* 153: 219-240.
- Mair, V., Zischg, A., Lang, K., Tonidandel, D., Kräiner, K., Kellerer-Pirklbauer, A., Deline, P., Schoeneich, P., Cremonese, E., Pogliotti, P., Gruber, S., Böckli, L., 2011. *PermaNET - Permafrost Long-term Monitoring Network. Synthesis report*. INTERPRAEVENT Journal series 1, Report 3. Klagenfurt.
- Thies, H., Nickus, U., Mair, V., Tessadri, R., Tait, D., Thaler, B., Psenner, R., 2007. Unexpected response of high Alpine lake waters to climate warming. *Environmental Science & Technology* 41: 7424-7429.



Variability of the hydrology of the Middle Lena River (Siberia) since 1937

Emmanuele Gautier¹, François Costard², Alexander Fedorov³
Thomas Depret¹, Delphine Grancher¹, Clément Virmoux¹ and Daniel Brunstein¹

¹LGP, Université Paris 1, Meudon, France, emmanuele.gautier@lgp.cnrs.fr

²GEOPS, Geosciences Paris Sud, Université Paris Saclay, Orsay, France,

³Permafrost Institut, Russian Academy of Science, Yakutsk, Russia

Abstract

The main aim of this study is to determine the hydrologic and morphodynamic response of the Lena River in Eastern Siberia to ongoing climate change. The hydrologic variability of the Middle Lena River indicates a net hydrologic change with an increase in the intensity and duration of floods in the two decades ending in 2012. The recent occurrence of storms in summer and the early autumn is probably the main cause of the “multi-peak” hydrograph we identified in the decade preceding 2012. Both erosion of the banks and the thickness of deposits were correlated with the duration of flooding

Keywords: permafrost, Siberia, flood, Lena, climatic change

Introduction

Recent observations indicate that over the last decades, climate change has increasingly influenced the frequency, intensity and duration of extreme climatic and hydrologic events. In Eastern Siberia, permafrost temperature already underwent an increase up to 1 °C over the course of the 20th century (Fedorov and Konstantinov, 2003) and an increase in warming has been observed since the beginning of the 21st century (Fedorov et al., 2014). The fluvial regime of the Arctic rivers is immoderate with very low flow during winter and a spring flood characterized by a steep rising limb and a peak discharge that can exceed by ten times the winter discharge. The frozen islands in the Lena River are much more sensitive to thermal erosion than the channel banks (Are 1983, Gautier et al., 2008). During floods, the combination of the increase of discharge and the increase of the temperature of the stream, explains the rapid bank retreat (Costard et al., 2003 and 2007).

The main aim of this study is to determine the hydrologic and morphodynamic response of the Lena River in Eastern Siberia to ongoing climate change. We examine the influence of the different parameters of hydrologic functioning on erosion and sedimentation. To this end, we also analyze the morphological and sedimentary response of the river using data from instrumented sites that were surveyed from 2008 to 2012.

Study area

The study area (61° 4'N and 129° 3'E) is located upstream of Yakutsk city near the the Tabaga gauging site. In the middle valley, upstream of Yakutsk city, the

Lena floodplain is 25 km wide. In that area, the Lena floodplain consists of a large number of shallow and wide channels that are between several hundred meters and three kilometers in width

From October to the end of April, the river Lena goes through a long low water stage, and is covered by ice between 200 and 250 days. The great majority of flood peaks occurs in May and June, associated with the flood wave coming from the upper basin and with the local break-up. Secondary peaks may be registered in summer, mostly due to rainstorms.

Data and methods

We used monthly and daily hydrologic data for 76 years at Tabaga gauging site for the 1937-2012 period. First, we calculated the mean monthly discharge, particularly for the spring and summer seasons (May-September) and we calculate high water level and the flooding period. The thermo-buttons were installed on different trees, at 0.5 m intervals from the soil surface to a height of 4 m; the temperature was recorded at 3 hourly intervals from the end of April until October. We estimated the effect of hydrologic events on erosion and sedimentation with high resolution analysis on different islands.

Results

Mean monthly discharges have increased significantly in recent decades. Winter discharges (November-April) were characterized by a significant increase after the late 1980s. Positive anomalies were recorded for monthly discharge in May; except 2003 & 2004. The recent hydrologic change is also reflected in the increased frequency of positive anomalies.

Two periods were characterized by frequent high floods. First, the 1957-1966 period was an active period. Second, after the 1980s, the frequency of floods greater than 40 000 m³s⁻¹ increased progressively (Fig. 1).

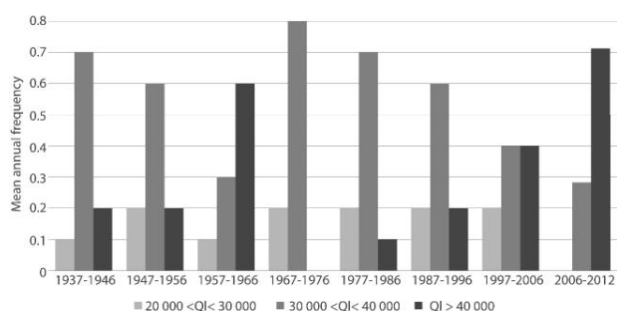


Figure 1: Mean annual frequency of maximum water discharge (per decade between 1937 and 2012).

Hydrologic changes can also be detected by analyzing the duration of the different classes of discharge. Discharges higher than 40 000 m³s⁻¹ rarely exceeded a few days. After 2004, longer durations became more frequent: 9 days in 2004, a historic maximum of 21 days in 2006, and 8 days in 2012.

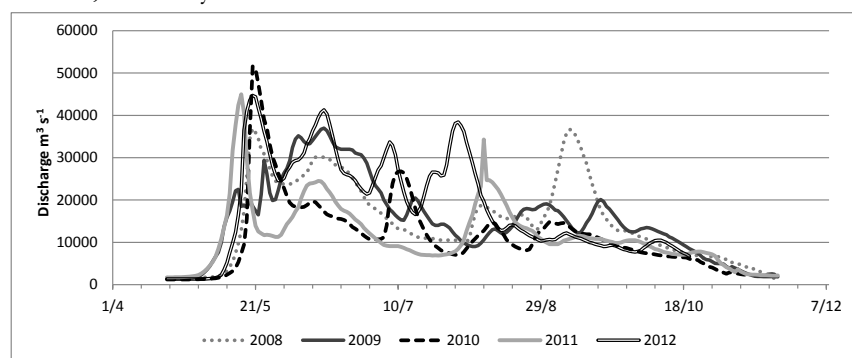


Figure 2: Recent floods with secondary peaks

Erosion and sedimentation were also measured on different river islands in the hydrologic years 2008-2012. Both erosion of the banks and the thickness of deposits were correlated with the duration of flooding and the period of flooding also influenced the bank retreat.

Conclusion

Spring monthly discharge has undergone a net increase caused by longer bar-full and bank-full water levels. Flood peaks are also more frequent. The hydrologic change is not only expressed by the flood intensity but also -and mainly- by the increasing duration of the discharges. The efficiency of the water discharges is reinforced by the increase in water temperature: later and longer hydrologic processes are combined with much warmer stream temperatures. Thus, the mobility of the channels and islands threatens numerous activities: navigation, and river infrastructure are destabilized

Examination of discharge between 1936 and 2012 confirmed that high variability is an intrinsic feature of the hydrologic functioning of the Lena River. The Central Yakutia was hardly affected by Arctic warming (1935-1945). An increase in the thawing index was evidenced from 1988 to 1995, and the increase was much more pronounced after 2005 (Fedorov et al., 2013).

The recent occurrence of storms in summer and the early autumn is probably the main cause of the “multi-peak” hydrograph we identified in the decade preceding 2012 (Fig. 2). At Tabaga, there is no clear correlation between the occurrence of a secondary flood peak in August or September and the precipitation. Thus the great majority of the secondary summer peaks mainly corresponds to a flood wave coming from the upper basin. In those areas, rainfall events can create a secondary flood in the summer (August or September) with a water discharge a little above 20 000 m³s⁻¹. These events are more frequent from the beginning of the 21st century.

Acknowledgments

Financial support from Agence Nationale de la Recherche ANR-07-VULN- (002 CLIMAFU), the GDR 3062 “Mutations Polaires.

References

- Are F. 1983. Thermal abrasion on coasts, Proceedings, *Fourth International Conference on Permafrost*, 24-28.
- Costard et al. 2007. Impact of the global warming on the fluvial thermal erosion over the Lena river in Central Siberia. *Geophys. Res. Lett.*, 34, (14).
- Gautier et al., 2008. Proceedings *9th International Permafrost Conference*. 493-498.
- Fedorov and Konstantinov, 2003. *Proceedings of International Permafrost Conference, Zurich*, 239-243.
- Gautier et al. 2018. Hydrologic response of Middle Lena River reach (Siberia) to the climate variability and change. *J. of Hydrology*, in press.



Identification of patterns in hydrological conditions governing flow in an unregulated river basin in the Northwest Territories, and implications for downstream hydroelectric power generation

Jennifer Hickman¹

Michael English²

Phil Marsh²

¹*Wilfrid Laurier University, Global Water Futures, jhickman@wlu.ca*

²*Wilfrid Laurier University, Cold Regions Research Centre*

Abstract

Located in the discontinuous permafrost zone of the Northwest Territories, Canada, the Snare River hydroelectric power system supplies power to the Territory's capital city, Yellowknife, and surrounding communities. Recent low water levels in the Snare River have intermittently reduced and/or eliminated the possibility of generating hydroelectric power, resulting in significant expenditure by NTPC on diesel fueled generators as an alternative power source. Of significant concern is whether low-flow conditions will become more frequent in the future, and result in a potentially non-sustainable expense. The objective of this study is to understand how antecedent climatic and hydrological conditions in an unregulated basin influence flow patterns, specifically the conditions that result in low discharge contributions to hydroelectric reservoirs. By identifying patterns among the various controls on flow, it may be possible to provide a predictive capacity for stakeholders of the Snare River hydroelectric system to aide in decision-making surrounding the generation of power.

Keywords: hydrology; subarctic; hydroelectric power; antecedent conditions

Study site and methods

The Snare River, located in the Northwest Territories, Canada, is used for generating hydroelectric power for the Territory's capital city of Yellowknife and several smaller communities. Low river flow during the last two decades, and most recently between 2013-2015, has intermittently reduced and/or eliminated the possibility of generating hydroelectric power, resulting in the expenditure of approximately \$30 million on diesel fuel as an alternative power source. Of significant concern to stakeholders is whether low flow and drought conditions will become more frequent in the future, resulting in a potentially non-sustainable expense.

The objective of this study is to understand how antecedent climatic and hydrological conditions in a large unregulated portion of the Snare basin influences flow patterns, specifically identifying those conditions that result in low recharge contributions to hydroelectric reservoirs. Identifying patterns among the variables controlling flow may provide a predictive capacity for stakeholders of the Snare River hydroelectric system, which may aide in decision-making regarding the future of power generation in the NWT.

As with many isolated northern river basins there is very little climatic or hydrological data available, and little research is undertaken upon which to base any predictive capacity. In the Snare watershed, aside from river flow data from Water Survey of Canada, very little usable data exists. Consequently, numerous extrapolation techniques using data external to, but within reasonable proximity to the basin, are utilized to quantify an annual hydrological mass balance. This includes employing remote sensing platforms for estimating snowpack water equivalent, and methods for estimating rainfall and evapotranspiration with storage solved as the residual in the mass balance equation. These calculations are complicated by the size and physical nature of the watershed, comprised of a dense network of interconnected lake catchments with shallow till underlain by widespread discontinuous permafrost. These terrain characteristics coupled with the large number of lake reservoirs complicates our understanding of storage.

For this study, a 17-year period, 1999-2015, was selected, providing us with a suitable range of hydrological and climatic conditions appropriate for ascertaining how antecedent conditions may play a role in subsequent years basin hydrology. It has become clear

that particular combinations of watershed conditions heavily influence the total outflow, and thus the ability to generate hydroelectric power downstream. In particular, this work highlights the common misconception that high water inputs from snow and rain will result in high water output at the basin outlet.

Results and discussion

The relationship between water inputs and outputs from this system are significantly governed by the timing and intensity of the most significant annual hydrological event; the spring freshet. By examining the slope of the cumulative flow curve during the thaw season, it is possible to identify which years experienced the most intense snowmelt (Fig. 1). Comparing these slope values to the overall basin efficiency confirms the importance of a rapid snowmelt (Fig. 2). For example, 2006 experienced a rapid snowmelt period, as indicated by the steep cumulative flow curve (Fig. 1), which resulted in a high basin efficiency (Fig. 2) and ultimately high river discharge at the basin outlet.

It is possible that a prolonged melt that occurs later in the thaw season is susceptible to higher losses to storage, as then the active layer has thawed to a greater depth in turn influencing storage potential. It is the combination of conditions like these that govern flow at the basin outlet, and ultimately determines the extent to which hydroelectric reservoirs will be filled.

While examining relationships among mass balance variables provides us with year to year insight into what potentially controls discharge from the unregulated portions of the Snare basin, it is also of interest to see if larger scale climatic events play a role in the future hydrological patterns in the Snare system. To do this we examined the long-term pattern of Arctic Oscillations (AO) and related this to annual peak snowpack water equivalent in the basin as determined from Globsnow. The AO record extends from 1949 to the present time. Over this period of time there is a slow but significant change from a dominance of negative AO to a positive AO, most pronounced over the past two decades (Fig.3). A somewhat weak but statistically significant positive relationship between AO index and SWE also exists (Fig.4). As we shift towards winters dominated by positive AO there is a tendency for increasing SWE.

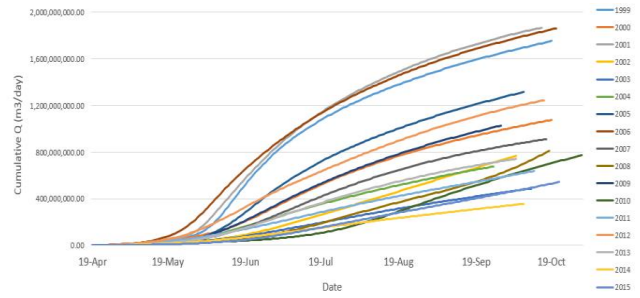


Figure 1. Thaw season cumulative Q 1999-2015

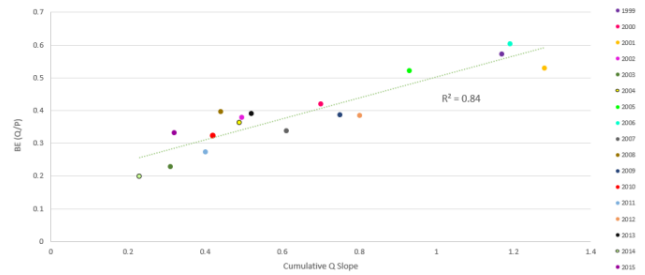


Figure 2. Cumulative Q slope vs. basin efficiency

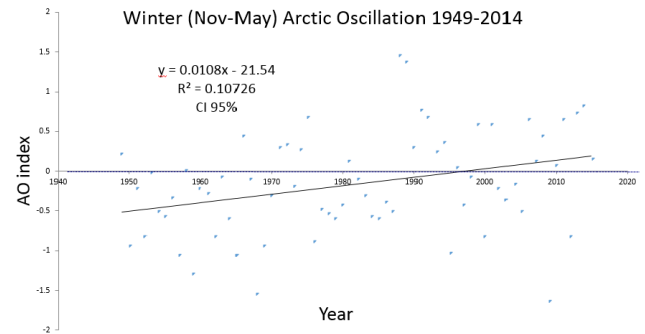


Figure 3. AO index change over time

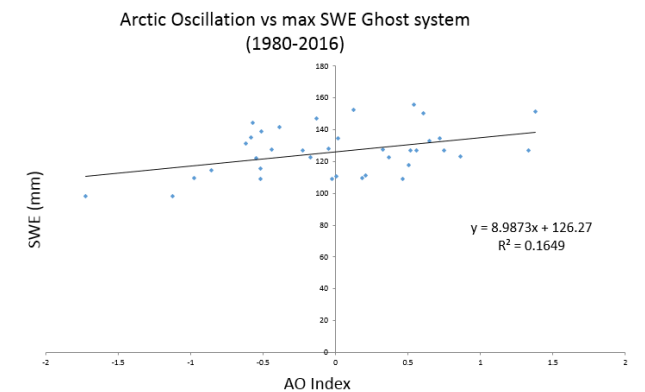


Figure 4. AO index vs. SWE

Using Snowmelt Peak Flows Drivers to Estimate Peak Flows on Alaska's North Slope

Alexa Marion Hinzman¹
Ype van der Velde²
Svetlana Stuefer³

¹*Vrije Universiteit Amsterdam, a.m.b.hinzman@vu.nl*

²*Vrije Universiteit Amsterdam*

³*University of Alaska Fairbanks*

Abstract

Historic drivers of peak flows can be used to predict future peak flows with the help of linear regression. Using historic data from four watersheds on the North Slope of Alaska, linear regression equations were created for individual watersheds and combined watersheds to identify independent physiographic and climatic variables that statistically predict future peak flows accurately. Snow water equivalent and antecedent soil moisture storage was determined to be strongest correlated variables in individual watersheds while area of the watershed was found to be the highest correlated variable when all watersheds were combined.

Keywords: Alaska; Snowmelt; Soil moisture; Peak flows.

Introduction

Snowmelt peak discharges in Alaska can cause flooding of roads and structures and millions of dollars of damage every year. Underestimating peak flows lead to more cases of flooding and more damage to infrastructure and the inability to reach remote locations. With a fast changing Arctic climate, to understand changes in peak flows it is important to identify the controlling factors.

Peak discharges on the North Slope of Alaska are accurately predicted through linear regression equations with independent meteorological and physiographic variables collected from four watersheds, verified through recorded snowmelt peaks. Terrestrial Environmental Observation Network (TEON) was initiated to monitor the North Slope of Alaska and continue historic data collection.

Study area

Each of the watersheds used in the study are somewhat unique. The Putuligayuk River watershed is located on the coastal plain of Alaska. The Upper Kuparuk River is the upper headwaters of the Kuparuk Watershed. Imnavait Creek abuts the Upper Kuparuk and has the longest historic data collection. Roche Moutonnée Creek is the most southern watershed and has the greatest slope. It has had peak flows collected

since 1976, however climatic data collection by TEON researchers was started in 2015.

Table 1. Watershed Comparisons.

Name of Watershed	Area (km ²)	Slope (km/km)	Record Length (years)	Storage Data Available?
Putuligayuk River	471	0.0015	17	Yes
Upper Kuparuk River	142	0.045	21	No
Imnavait Creek	2.2	0.027	31	Yes*
Roche Moutonnée Creek	84	0.164	25	No

*Partial Record

Methods

This paper compares frequently used flood frequency analysis techniques, and produces linear regression equations to predict peak flows for each watershed as well as all watersheds combined. Bulletin 17B was utilized as the first flood frequency analysis technique (U.S. Interagency Advisory Committee on Water Data, 1982). U.S. Geological Survey used a least square regression approach to create regional sets of equations to predict peak flows (Curran *et al.*, 2016). This method was also compared to the linear regression equations.

Discussion

From five linear regression equations created, three found snow water equivalent (SWE) to be the most significant predictor of peak flows. The first attempt to estimate peak flows for all watersheds used area and had a high R^2 value of 0.72. The second equation for all watersheds included area and SWE as the meteorological independent variable. It was interesting to note the soil moisture storage was not indicative of peak flow magnitudes for each individual watershed.

Conclusion

While the evidence presented is quite promising that modeling can be useful in estimating peak flows in ungauged arctic watersheds, the limitations of using only four watersheds to determine the equations call for further analysis and verification. More validation studies are needed to demonstrate that viable equations may be applied to all watersheds on the North Slope of Alaska or to other regions.

Acknowledgments

This study was funded by Arctic Landscape Conservation Cooperative (ALCC) through Terrestrial Environmental Observation Network (TEON).

I thank Janet Curran and the USGS Alaska Science Office, as well as the USGS researchers who helped collect historic peak flow data for the Putuligayuk River and Roche Moutonnée Creek.

I thank the WERC faculty, staff and students at the University of Alaska Fairbanks for collecting and processing data over the years, specifically Rob Gieck, Emily Youcha, and other researchers who collected the historic data. I also thank the professors, Svetlana Stuefer, Chris Arp and David Barnes.

References

- Curran, Janet H, Nancy A Barth, Andrea G Veilleux & Robert T Ourso., 2016. Estimating Flood Magnitude and Frequency at Gaged and Ungaged Sites on Streams in Alaska and Conterminous Basins in Canada, Based on Data through Water Year 2012. *Scientific Investigations Report*: 1-47.
- U.S. Interagency Advisory Committee on Water Data. 1982. *Guidelines for Determining Flood Flow Frequency*, Bulletin 17B of the Hydrology Subcommittee. Edited by U.S. Geological Survey. Reston, Virginia: Office of Water Data Coordination, 183pp.



Hydrologic connectivity is a key control on the impacts of permafrost disturbance on fluvial fluxes

Melissa J. Lafreniere¹

Scott F. Lamoureux²

¹*Department of Geography and Planning, Queen's University, Kingston, ON, Canada, Melissa.lafreniere@queensu.ca*

²*Department of Geography and Planning, Queen's University, Kingston, ON, Canada*

Abstract

This study reviews research on the impacts of changing permafrost conditions on the fluvial exports in a High Arctic permafrost setting. This body of research highlights the importance of hydrological connectivity in regulating the response of watershed biogeochemical fluxes to physical and thermal disturbance of permafrost. The research identifies that the impacts of permafrost disturbances on fluvial biogeochemical fluxes are the result of hydrologic connectivity between affected landscapes and streams, which is primarily a function of i) the surface exposure of excess ice and solute-rich permafrost, and ii) late summer rainfall. An improved understanding of biogeochemical flux response of watersheds to permafrost disturbances requires better knowledge of the key characteristics and processes that establish hydrological connectivity in permafrost watersheds, such as the distribution of ice in the upper permafrost, and the physical characteristics of the active layer that control infiltration and runoff generation.

Keywords: permafrost disturbance, permafrost hydrology, fluvial fluxes, hydrologic connectivity

Introduction

Climate change is simultaneously altering permafrost conditions and hydrological regimes in Arctic watersheds (AMAP, 2017). Deep thaw and permafrost disturbances, including active layer detachments (ALDs), thermo-erosion features, and retrogressive thaw slumps generate important downstream hydrological and biogeochemical responses (Abbott *et al.*, 2015; Lafrenière *et al.*, 2017; Roberts *et al.*, 2017).

This paper examines the magnitude and persistence of the impact of permafrost change on the fluvial export of material (including particulates, inorganic ions, nutrients and dissolved organic matter (DOM)) as reported in research conducted at the Cape Bounty Arctic Watershed Observatory (CBAWO). Specifically, this synthesis examines how the impacts of permafrost perturbations (e.g. deep thaw and physical disturbance) on the fluxes of important water quality components are related to processes that establish hydrological connectivity between the landscape and streams.

Permafrost disturbances

We identify two dominant mechanisms of permafrost perturbation that impact fluvial exports: physical disturbance and thermal perturbations (Lafrenière & Lamoureux, 2013). Physical disturbances result in the fracture, displacement and/or complete removal of the organic rich surface soil horizon, and the exposure of previously buried mineral soils. These disturbances are

spatially constrained, but can have pronounced impacts on the surface morphology of the landscape, and thus influence the storage and surface water flow pathways.

Thermal perturbation occurs when thaw extends beyond the usual depth of the active layer, into the transition zone, or shallow permafrost. Increasing the depth of thaw increases potential soil water storage, introduces new flow pathways, and liberates previously frozen mobile solutes and nutrients (Lamhonwah *et al.*, 2017). These thermal perturbations do not have visible geomorphic impacts, yet they are spatially extensive, affecting the active layer across the entire catchment.

Flux Response and Hydrologic connectivity

Impacts of disturbance type on flux response

Various studies from CBAWO demonstrate that the physical disturbance, in the form of ALDs, enhance the fluvial fluxes of sediment (Lamoureux *et al.*, 2014), inorganic solutes and nitrogen (Lamhonwah *et al.*, 2017; Lafrenière *et al.*, 2017), and decrease the flux of DOM (Fouché *et al.*, 2017). These changes in fluxes were not related to the extent of the disturbed area, but rather to the degree of channelization of the disturbances, which is a measure of hydrologic connectivity. (Lafrenière & Lamoureux, 2013; Lamoureux *et al.* 2014). The impacts on fluxes were both more prominent and more persistent in watersheds where incised channels, and/or continued disturbance, exposed fresh sediment (Lamoureux *et al.*, 2014). Hence, the magnitude and

persistence of disturbance impacts on fluxes are a function of the degree to which freshly exposed or disturbed material is flushed and/or eroded.

Thermal perturbations have also been shown to substantially increase solute fluxes, even in absence of physical disturbance (Lafrenière & Lamoureux, 2013). The composition of water stable isotopes and ions in permafrost cores support that the thawing of the ice rich and ion rich transition zone was the likely the source of the water and ions during these periods of deep thaw (Lamhonwah *et al.*, 2017). These findings demonstrate that deep thaw can hydrologically connect this subsurface ice and solute-rich zone to the channel system. This hydrological connection involves a limited extent of the active layer, and minimal flow volumes, however, the impacts can be important as thaw can conceivably hydrologically- connect the entire catchment.

Water inputs are also key to establishing hydrologic connectivity. Until recently, snow was considered the most important water input, and the extensive hydrologic connectivity established during snowmelt was considered the primary control on fluvial fluxes in permafrost watersheds. However, recent studies at CBAWO documents that late summer rainfall, especially in combination with deep thaw and physical disturbances, can provide a larger flux of solute and sediment than the nival runoff period (Lewis *et al.*, 2012; Lafrenière & Lamoureux, 2013). The significant impact of summer rainfall on material fluxes is likely because rainfall establishes spatially extensive hydrologic connectivity at a time when sediment and solutes at the surface of disturbances or deep in the active layer are readily mobilized.

Conclusions

This body of research indicates that the impacts of permafrost disturbances on fluvial biogeochemical fluxes are the result of hydrologic connectivity between affected landscapes and streams, which is primarily a function of i) the thaw and disturbance of unconsolidated ice rich material, and ii) late summer rainfall.

Our findings support that an improved understanding of biogeochemical response and recovery of watersheds to permafrost disturbances requires better knowledge of i) the distribution of ice in the upper permafrost, ii) physical characteristics of the active layer that control infiltration and generation of subsurface flow and rainfall runoff, and iii) the processes controlling the stabilization of disturbances. Knowledge of these parameters would facilitate the development of metrics that can be used do model the hydrological connectivity,

and thus biogeochemical response of watersheds to permafrost and climate change.

Acknowledgments

We acknowledge the efforts of all the students and postdoctoral fellows who have contributed to research at CBAWO. Research funding has been provided by NSERC, ArcticNet, the Government of Canada International Polar Year program, and Environment and Climate Change Canada. The Polar Continental Shelf Programme has supported our field logistics.

References

- Abbott, B.W., Jones, J.B., Godsey, S.E., Larouche, J.R. & Bowden, W.B. 2015. Patterns and persistence of hydrologic carbon and nitrogen export from collapsing upland permafrost. *Biogeosciences* 12: 3725-3740.
- AMAP 2017. *Snow, Water, Ice and Permafrost in the Arctic (SWIPA) 2017*, Arctic Monitoring and Assessment Programme (AMAP), Oslo, Norway, 269 pp.
- Fouché, J., Lafrenière, M.J., Rutherford, K. & Lamoureux, S.F., 2017. Seasonal hydrology and permafrost disturbance impacts on dissolved organic matter composition in High Arctic headwater catchments. *Arctic Science* 3(2): 378-405.
- Lafrenière, M.J. & Lamoureux, S.F., 2013. Thermal perturbation and rainfall runoff have greater impact on seasonal solute loads than physical disturbance of the active layer. *Permafrost and Periglacial Processes* 24, 241-251.
- Lafrenière, M.J., Louiseize, N.L. & Lamoureux, S.F., 2017. Active layer slope disturbances affect seasonality and composition of dissolved nitrogen export from High Arctic headwater catchments. *Arctic Science* 3(2): 429-450.
- Lamhonwah, D., Lafrenière, M.J., Lamoureux, S.F. & Wolfe, B.B. (2017) Multi-year impacts of permafrost disturbance and thermal perturbation on High Arctic stream chemistry. *Arctic Science* 3(2), 254-276.
- Lamoureux, S.F., Lafrenière, M.J. & Favaro, E., 2014. Erosion dynamics following localized permafrost slope disturbances. *Geophysical Res. Lett.*41: 2014GL060677R.
- Lewis, T., Lafrenière, M.J. & Lamoureux, S.F., 2012. Hydrochemical and sedimentary responses of paired High Arctic watersheds to unusual climate and permafrost disturbance, Cape Bounty, Melville Island, Canada. *Hydrological Processes* 26(13):2003-2018.
- Roberts, K.E., Lamoureux, S.F., Kyser, T.K., Muir, D.C.G., Lafrenière, M.J., Iqaluk, D., Pieńkowski, A.J. & Normandeau, A., 2017. Climate and permafrost effects on the chemistry and ecosystems of High Arctic Lakes. *Scientific Reports* 7(1), 13292.



Distribution of suprapermafrost taliks in the Shestakovka River catchment, continuous permafrost zone

Liudmila Lebedeva
Ivan Khristoforov
Kirill Bazhin

Melnikov Permafrost Institute Siberian Branch Russian Academy of Sciences, Yakutsk, Russia, lyudmilaslebedeva@gmail.com

Abstract

GPR and ERT measurements at sandy slopes covered by sparse pine forest within the Shestakovka river catchment (Central Yakutia, Russia) showed that there are water-saturated suprapermafrost taliks at eight profiles out of fifteen. Pine forest covers 47% of the watershed area. We conclude that 20-25% of the watershed area could be occupied by taliks in continuous permafrost environment. It suggests possible importance of groundwater pathways for the runoff generation even for the small rivers that do not have any channel flow during the cold season.

Keywords: talik; suprapermafrost groundwater; permafrost; Electrical resistivity tomography; Ground Penetrating Radar.

Introduction

In hydrology, continuous permafrost is usually considered as impermeable frozen ground. Surface flow and flow in the shallow seasonally thawing layer are often main sources of river flow in permafrost river catchments. Suprapermafrost taliks are known in Eastern Siberia in the Lena and Vilyuy rivers terraces. They are usually found on the well-drained gentle sandy slopes covered by sparse pine forests. Although existence of taliks is acknowledged, their distribution, genesis, evolution and role in surface-subsurface water interactions remain unresolved issues.

Geophysical techniques could provide spatially and vertically distributed information about permafrost, taliks and groundwater that cannot be obtained from drilling data alone. The study aims at estimation of talik distribution in the Shestakovka research watershed by combination of Electrical Resistivity Tomography (ERT) and Ground Penetrating Radar (GPR) techniques.

Study site

The Shestakovka River watershed with area 170 km² is located in 20 km to south-west of Yakutsk within the erosion-denudational slope of the ancient accumulative plain with absolute elevation of 150-280 m. The permafrost thickness is 200-400 m. The upper 40 m of the section are represented by quartz-feldspar sands with rare inclusions of silty sandy loam and loam. The climate is cold and dry with mean annual air temperature -9.5°C,

precipitation 240 mm/year (1950-2015). Mean annual river flow depth is 24 mm/year (1951-2015). Dominant landscapes are pine (47% of the watershed area) and larch (38%) forests. Mires and bogs cover rest of the watershed. Active layer (AL) thickness in the pine forest could reach 3-4 m. Larch forests are characterized by cold permafrost with AL thickness up to 1 m.

Methods

Overall approach

Boitcov (2011) revealed that in Central Yakutia taliks could be found when three factors meet: i) bare soil or soil sparsely covered with organic layer ii) sandy deposits iii) hilly relief. Fifteen key sites within the Shestakovka catchment were chosen that meet the above-mentioned criteria. 300 m-long GPR profiles were measured at every key site in early May 2017. Six profiles were selected for more time-consuming ERT measurements that were performed in later May and September 2017. There are boreholes at two key sites that allow verification of geophysical results.

Electrical Resistivity Tomography

16-channel ERT and IP instrument SibER-64 produced by "Siber-instruments" (Novosibirsk, Russia) was used for ERT measurements. Two cables consisting of 32 copper wires were employed. Ground connection was performed by means of steel rods 300 mm long.

Unit electrode spacing varied from 1 to 5 m depending on required level of detail and studied depth. Dipole-dipole array, gradient array and Schlumberger array with four electrodes were used for measurements. Data processing and interpretation were performed using RiPPP and ZondRes2d software packages.

Ground Penetrating Radar

GPR measurements were made with an OKO-2 georadar system (from the company *Logis-GEOTECH Ltd.*) with an antenna block with central frequencies of 150 and 250 MHz. The measurements were conducted with transmitter and receiver in contact with the frozen ground in profiling mode with scan duration of 200 ns.

Results

GPR measurements showed that there are water-saturated suprapermafrost taliks at eight profiles out of fifteen. Landscape scheme, “talik” and “non-talik” profiles are shown at the Figure 1. Typical talik thickness is from 2 to 10 m. Talik extent varies from 30-40 to more than 500 m. If assume that selected key site are representative for pine forest of the watershed we conclude that 20-25% of the watershed area could be occupied by taliks. The high fraction of taliks containing suprapermafrost groundwater suggests possible importance of groundwater pathways for the river runoff generation even for the small watershed in continuous permafrost zone.

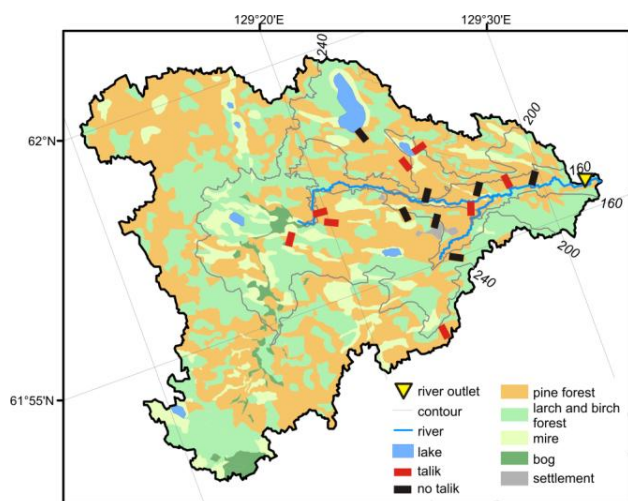


Figure 1 Landscape scheme of the Shestakovka catchment and results of the geophysical survey

Six profiles (five with taliks and one without) were selected for more time-consuming ERT measurements.

ERT results confirmed talik presence at five profiles and absence at one.

Good agreement between GPR and ERT measurements increase reliability of the interpretation of geophysical data. Borehole drilling is planned for the spring 2018.

Conclusions

GPR and ERT measurements showed that 2-10 m deep suprapermafrost taliks are abundant phenomena at sandy gentle slopes covered by pine forests in continuous permafrost environment in Central Yakutia, Russia. 20-25% of the Shestakovka watershed area could be occupied by taliks. The high fraction of taliks containing suprapermafrost groundwater suggests possible importance of groundwater pathways for the river runoff generation even for the small watershed in continuous permafrost zone. Understanding of groundwater storages could advance concepts of runoff generation that underlay hydrological, hydrogeological and permafrost modelling strategies and future projections.

Acknowledgments

The study is partially supported by the Russian Foundation for Basic Research, grants № 17-05-00926 and № 16-31-60082_mol_a_dk.

References

Boitcov A.V. 2011. *Geocryology and underground water of the cryolithozone*. Tyumen: Tyumen State Oil and Gas University Press, 177 pp.

Hydraulic behaviour of a liquid through thawing soil in a geotechnical centrifuge

Patrick Nadeau¹
Ryley Beddoe¹
Sarah Creber¹

¹Royal Military College of Canada, Kingston, Ontario

Abstract

Understanding how hydrology in cold regions is affected by long-term seasonal freeze-thaw cycles can be a challenge, especially on a large scale. Remoteness and logistical challenges make long-term research of in-situ hydrology in these regions an expensive endeavour. In this study, a geotechnical centrifuge was used to examine soil-water interactions during a thawing cycle, by taking advantage of centrifuge scaling laws that allow one to simulate this cycle within a few days or even hours. The dimension scale effect allows us to simulate the behaviour of large prototype areas using benchtop sized models. This study presents the development of an in-flight climate chamber, allowing for thawing of the sample. The ability to simulate a freeze-thaw cycle in the centrifuge can provide us with the means of creating physical models for frost heave, thaw settlement, hydrogeology and contaminant transport in cold regions, such as Canada's Arctic.

Keywords: Freeze-thaw; geotechnical centrifuge; contaminant transport.

Introduction

Centrifuge

Geotechnical centrifuge modelling can be used to understand and solve complex engineering problems. The basic concept of geotechnical centrifuge modelling is to enhance the gravitational field of a 1/N scaled model to replicate the stresses at prototype or field conditions (e.g. Mudabhushi, 2015). A 1.5m diameter Broadbent geotechnical centrifuge (Fig. 1), recently acquired by the Royal Military College of Canada, was used for these simulations. In the centrifuge, the scaling law for seepage velocity is: Model/Prototype = N. The scaling law for time is 1/N, since these tests were dynamic in nature (Madhabushi, 2015).



Figure 1. Broadbent geotechnical centrifuge.

Goal

The goal of this research is to establish the methodology to best replicate, in the centrifuge, the annual freeze-thaw cycles to which Canada's Arctic is subject. However, there are several challenges associated with conducting freeze-thaw processes in a geotechnical

centrifuge, and as such there have been limitations on this technique being widely used by the permafrost and cold regions research communities. In these preliminary tests, a climate chamber was used to establish environmental conditions within the centrifuge cradle. The hydraulic boundary conditions for different particle-sized soils were then observed while it thawed during flight.

Methodology

Test 1

The first test (Fig. 2) consisted of a frozen layer of saturated Kaolin clay. The thickness of the model was 60 mm which represents a 1.8 m thick soil layer. Ice pucks were placed at the top of the sample to simulate the leaching of an initially frozen contaminant in the spring. The puck on the left was mixed with black food dye while the other was mixed with potassium permanganate. The sample was subject to 30g acceleration for 95 minutes. In order to promote thawing, room-temperature air was blown across the air surface above the soil layer throughout the test.

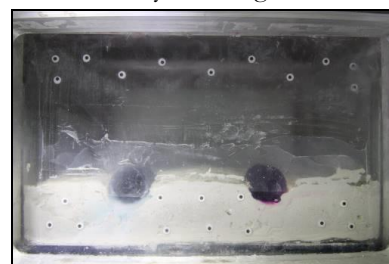


Figure 2. Initial conditions for Test 1.

Test 2

The second test (Fig. 3) consisted of a frozen 60 mm layer of saturated Aqua Quartz #20 pool filter sand superposed by a frozen 30 mm layer of dry sand of the same type which would represent 1.8 m and 0.9 m layers respectively. Three frozen pucks of water and potassium permanganate were placed in a line in the middle of the sample. After 10 minutes, two pucks were moved to new locations. The sample was subject to 30g acceleration for 60 minutes.



Figure 3. Initial conditions for Test 2.

Results

Test 1

This test simulated the movement of dyed water through saturated Kaolin clay over a 48 hour period. It was observed that the water dyed with potassium permanganate was more easily visualized, which is why it was used exclusively for Test 2. The dyed water moved vertically through the clay and even moved laterally when it encountered large voids filled with water (Fig. 4). The consolidation and subsequent drainage of the clay throughout thawing was also observed.

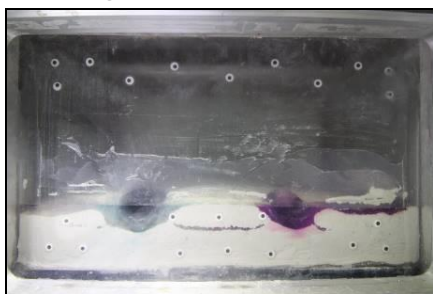


Figure 4. Movement of dyed water through clay.

Test 2

This test was a simulation of the movement of dyed water through a layer of unsaturated sand and a layer of saturated sand over a 30 hour period. Interestingly, the water table dropped approximately 1 cm when the centrifuge started rotating. As expected, the dyed water moved through the sand faster than it did in the clay.

Once the water reached the water table, it dispersed laterally throughout the saturated layer of sand (Fig. 5). It appears that there is a hydraulic gradient towards the small exit port at the bottom left of the cradle.

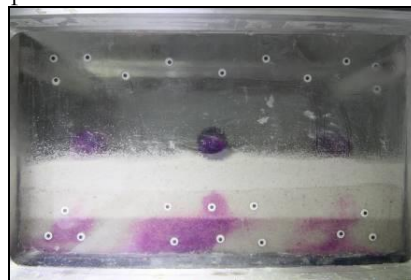


Figure 5. Movement of dyed water through sand.

Conclusion

With these tests, it has been shown that it is possible to simulate thawing soil in the centrifuge and to observe the hydraulic behaviour of an initially frozen liquid during the thawing process. Eventually, the goal is to simulate several freeze-thaw cycles in a single test by building a climate controlled cradle, which would use vortex tubes and insulation (e.g. Stone *et al.*, 1995; Clark & Phillips, 2003), as well as the means to monitor temperature throughout the sample while in flight. Another goal is to monitor the movement of different contaminants through soil undergoing freeze-thaw cycles. In that case, the water in the soil could not act as a conduit for diffusion (Biggar *et al.*, 1998), which might slow the vertical movement and eliminate the lateral movement through the soil.

References

- Biggar, K.W., Nahir, N., Haidar, S., 1998. Migration of petroleum contaminants into permafrost. *Proceedings of the Seventh International Conference on Permafrost*, Yellowknife, Canada, 23-27 June: 43-49.
- Clark, J.I. & Phillips, R. 2003. Centrifuge modelling of frost heave of arctic gas pipelines. *Proceedings of the Eighth International Conference on Permafrost*, Zürich, Switzerland, 21-25 July: 151-156.
- Madabhushi, G., 2015. *Centrifuge Modelling for Civil Engineers*. CRC Press, 292 pp.
- Stone, K.J.L., Smith, C.C. & Schofield, A.N., 1995. Technical Report No: CUED/D-SOILS/TR296. A Thermally controlled test chamber for centrifuge and laboratory experiments. *Cambridge University Engineering Department*.

Assessment of aufeis role in hydrological regime of the North-Eastern Russia

Natalia Nesterova^{1,2}

Olga Makarieva^{1,3,4}

Andrey Ostashov¹

Andrey Shikhov⁵

¹St. Petersburg State University, St. Petersburg, Russia, nnesterova1994@gmail.com

²State Hydrological Institute, St. Petersburg, Russia

³Gidrotehproekt Ltd, St. Petersburg, Russia

⁴Melnikov Permafrost Institute, Yakutsk, Russia

⁵Perm State University, Perm, Russia

Abstract

The goal of the research is the development and verification of mathematical modelling methods for assessing and predicting the role of aufeis in hydrological regime of the rivers of the North-East of Russia in current and future climate. Three catchments with available historical data on the location and characteristics of the aufeis and runoff observations with basin areas from 400 to 8290 km² and aufeis share from 6 to 113 km² in mountainous area of North-East are chosen for the study. The method of Sokolov was adapted to the Hydrograph model for calculating aufeis runoff. Historical information on aufeis locations and their features from the Aufeis Cadaster (1958) was corrected with the use of topographic maps and satellite images. The values of the aufeis flow vary from 9 to 13 % of the average annual river flow for the Suntar and Charky rivers accordingly, which puts aufeis on the one level with the glaciers in the sense of their impact on hydrological regime in studied region.

Keywords: aufeis; river runoff; hydrological modelling; Hydrograph model; the North-East of Russia.

Introduction

Hydrological processes occur in specific conditions in the mountains of the North-Eastern Siberia. The aufeis are the indicators of the complex interconnection of river and groundwater in permafrost environment (Sokolov, 1975) and play an important hydrological role in that region. In winter, they reduce the river and underground runoff, and in warm season melted aufeis waters form additional source of rivers flow. Under the changing climate conditions, understanding the role of aufeis in runoff formation processes is an important task. In most cases, the share of the aufeis component of annual river runoff is about 3-7% (Reedyk *et al.*, 1995; Sokolov, 1975). At the same time, water consumption from melting aufeis (based on the data from Alaska and Canada) can be 1.5-4 times higher than the water discharge of groundwater forming it (McEven & Marsily, 1991). Most significant flow from melting aufeis is observed in May-June. In some river basins with exceptionally large aufeis, the proportion of this runoff can reach 25-30% (Sokolov, 1975).

Approach

Up to this point, there are no hydrological models that take into account the role of aufeis in rivers flow formation in an explicit form. In this study we aimed to update the Hydrograph model with such additional algorithm.

The Hydrograph model (Vinogradov *et al.*, 2011) describes hydrological processes in different permafrost environments including the dynamics of ground thaw/freeze. In this model the processes have a physical basis and certain strategic conceptual simplifications. The level of model complexity is suitable for a remote, sparsely gauged region such as Arctic domain as it allows for a priori assessment of the model parameters (Semenova *et al.*, 2013).

The method of Sokolov (1975) to estimate the aufeis flow was adapted for modelling aufeis input to river runoff in the Hydrograph model. The method makes it possible to calculate the hydrograph of aufeis-runoff for a long period and specific years, at basin scale and for an individual aufeis. The method requires following data:

daily air temperature at aufeis, maximum area of aufeis before spring melt; the altitude of individual or grouped aufeis. The other conceptual parameters that for example account for share of aufeis destruction due to air temperature, solar radiation and thermal erosion by river flow were estimated by Sokolov (1975) based on the field data obtained in 1960s.

By Sokolov (1975) the ice volume in aufeis is calculated depending on the area (1):

$$W=0,96F^{1,094} \quad (1)$$

where W – ice volume of aufeis, thousand km^3 ; F – area of aufeis, thousand km^2 .

Initial information on aufeis locations and their characteristics within the catchments was taken from the Cadaster of the aufeis of the North East Siberia of the USSR (1958) and corrected by topographic maps and satellite images. Satellite imagery were used also to assess the inter-annual and seasonal dynamics of aufeis within the period of 1999 to 2017 in chosen catchments.

The correction of the input meteorological information according to the climatic change trends would allow assessment of changes of the aufeis share runoff in total river flow in the future.

Study objects

Three catchments with available historical data on the location and characteristics of the aufeis and runoff observations were chosen for the study: the Charky river (03474), the Suntar river (03499) and the Anmangynda river (01604) belonging to the Yana, Indigirka and Kolyma Rivers basins correspondingly (Table 1, Fig.1).

Preliminary comparison of the Cadaster and satellite data at the Charky river basin has shown that some large aufeis are absent in the Cadaster and some historical aufeis are absent at modern satellite images. This may indicate the dynamics of aufeis processes in this region, which will be studied together with climate data.

Table. 1 Study objects

River (gauge code)	Period	Area, km^2	Aufeis area, km^2 (%)	Annual river runoff, mm	Calculated aufeis runoff, mm (%)
03474	1949-2007	8290	113 (1.4)	239	32 (13)
03499	1959-2015	7680	58 (0.8)	189	17 (9)
01604	1962-1992	400	6 (1.5)	301	24 (8)*

* from Sokolov (1975)

First results

The aufeis flow was estimated for the period 1965-2012 for two rivers using historical meteorological information. It accounted for about 13 % (32 mm) of average annual flow at the Charky river and about 9 %

(17 mm) at the Suntar river. The preliminary results suggest that aufeis flow may be much more significant than one from the glaciers.

The modelling approach, the results of satellite imagery analysis and aufeis flow assessment will be presented.

References

Cadastre to the map of aufeis of the North East Siberia of the USSR. 1958. Scale 1:2000000. Shilnikovskaya Z.G./Central complex thematic expedition of the North-Eastern Geological Administration. Magadan

McEwen, T., & Marsily, G.de. 1991. *The potential significance of permafrost to the behavior of a deep radioactive waste repository* (SKI-TR - 91-8). Sweden

Reedyk, S., Woo, M.K., Prowse T.D. 1995. Contribution of icing ablation to flowflow in a discontinuous permafrost area. *Canadian Journal of Earth Science* 32: 13-20

Semenova, O., Lebedeva, L., Vinogradov Yu. 2013. Simulation of subsurface heat and water dynamics, and runoff generation in mountainous permafrost conditions, in the Upper Kolyma River basin, Russia. *Hydrogeology Journal* 21(1): 107–119 DOI: 10.1007/s10040-012-0936-1

Sokolov B.L. 1975. *Aufeis and river runoff*. Leningrad: Gidrometeoizdat, 190 pp.

Vinogradov, Yu.B., Semenova, O.M., Vinogradova, T.A. 2011. An approach to the scaling problem in hydrological modelling: the deterministic modelling hydrological system. *Hydrological Processes*. 25: 1055–1073, doi:10.1002/hyp.7901.

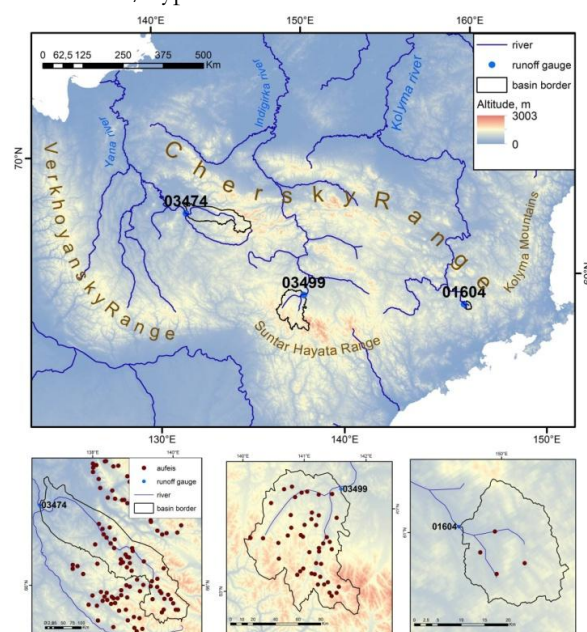


Figure 1. The study basins, red dots are aufeis locations (without scale).

Hydrological change trajectories in the southern Taiga Plains, Canada

William Quinton¹, Michael Braverman¹, Ryan Connon¹, James Craig², Élise Devoie², Kristine Haynes¹

¹Wilfrid Laurier University, Waterloo, Ontario, Canada, wquinton@wlu.ca

²University of Waterloo, Waterloo, Ontario, Canada

Abstract

Climate warming in the southern Taiga Plains ecoregion of northwestern Canada has led to unprecedented rates of permafrost thaw and a myriad of land-cover changes with uncertain impacts on hydrology. Consequently there is growing uncertainty in regards to the future availability of water resources in this region. This paper synthesises key findings of recent hydrological field studies and remote sensing analyses of land-cover change in the southern Taiga Plains. The purpose of this synthesis is to improve the understanding of the trajectory of land-cover change in this region and how this change could influence water flow and storage processes.

Keywords: Permafrost thaw, landcover change, peatlands, Boreal, hydrology.

Introduction

This study is focussed on the southern Taiga Plains ecoregion in northwestern Canada (Figure 1a), and draws mainly from studies conducted at Scotty Creek (61°18' N, 121°18' W), a 152 km² drainage basin 50 km south of Fort Simpson, Northwest Territories (NWT) (Figure 1b). Scotty Creek basin is underlain by discontinuous permafrost and is covered by peatland complexes typical of the 'continental high boreal' wetland region. The peat thickness at Scotty Creek ranges between 2 and 8 m below which lies a thick clay/silt-clay glacial till deposit of low permeability. Most of the Scotty Creek basin is a heterogeneous mosaic of forested peat plateaus underlain by permafrost, and treeless, permafrost-free wetlands (Figure 1c), typical of the southern fringe of discontinuous permafrost (Helbig *et al.*, 2016). Fort Simpson has an average annual air temperature of -2.8° C, and receives 388 mm of precipitation annually, of which 38% is snow. This paper draws on numerous published and unpublished studies involving both hydrometric field observations and aerial/satellite image analysis. Collectively these studies are used to inform conceptualisations of hydrological change.

There are strong indications that permafrost thaw and the resulting land-cover changes have affected basin water balances, as suggested by rising river flows throughout the border region. Most notably, the total annual runoff from all gauged rivers in the lower Liard River valley of the NWT has steadily risen since the mid-1990s (Connon *et al.*, 2014). Rising flows from subarctic rivers are often attributed to 'reactivation' of groundwater systems, but the very low hydraulic

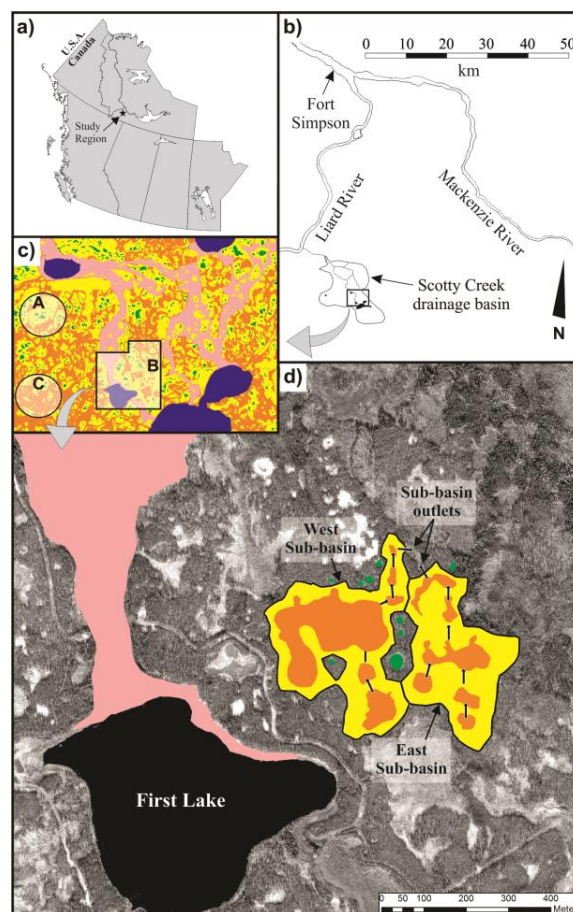


Figure 1: a) study region and b) Scotty Creek; c) peat plateaus (yellow), isolated (green) and connected (orange) bogs, channel fens (pink); d) enlargement of "B" showing cascade bogs.

conductivity of the glacial sediments below the peat, precludes appreciable groundwater input. Permafrost thaw-induced changes to basin flow and storage processes offers a more plausible explanation for rising river flows in this region (Connon *et al.*, 2015).

Field observations and image analyses (suggest that plateaus contain two distinct runoff source areas separated by a break in slope approximately 10 m inland from the fen-plateau edge. Primary runoff drains from the sloped edges of plateaus directly into the basin drainage network (*i.e.* a channel fen). Field measurements suggest that the entire primary area supplies runoff to the fen throughout the thaw season. Secondary runoff drains into the interior of the plateau toward the topographic low often occupied by a bog. If the receiving bog is hydrologically isolated, the runoff it received will remain in storage, evaporate or recharge the underlying aquifer. If the receiving bog is part of a bog cascade, and if its storage capacity is exceeded, then the secondary runoff it receives will be routed toward the channel fen via the down slope bog or bogs. Secondary runoff is therefore, neither direct nor continuous. The rate of secondary runoff is greatest during periods of high moisture supply and minimal ground thaw when the hydrological connection among the bogs of a cascade, and between individual bogs and their contributing “bog-sheds” is maximised. As the active layer thaws and drains, the contributing area shrinks and secondary runoff decreases. Large rain events can temporarily reverse this decrease.

Over a period of decades, the plateaus conducting primary and secondary runoff are transformed by permafrost thaw. Three general stages can be seen from Figure 1c. In chronological sequence, the area indicated by “A” represents an early stage of permafrost thaw where bogs are mostly hydrologically-isolated, and as such, drainage into the fen is supplied only by primary runoff from the margins of the plateaus. “B” represents an intermediate stage of permafrost thaw where primary runoff is augmented by secondary runoff from the ephemeral bog cascades. The activation of secondary runoff arises from the greater hydrological connectivity of land-cover “B” than “A”. As a result, a greater proportion of the snowmelt and rainfall arriving on land-cover “B” is converted to runoff than in the previous stage. Because B is transitional between A and C, some bogs are hydrologically connected (via surface or near surface flow and/or talik flow), while other bogs remain hydrologically isolated. “C” represents an advanced stage, where the shrinking peat plateaus occur as islands within an expansive bog complex. Interestingly, this stage is a near mirror image of “A” where it is the bogs that occur within an extensive plateau complex. By stage “C”, plateau diameters are on

the order of a few tens of metres and as such contain no secondary runoff and no interior bogs.

As the land-cover transitions from the isolated bog (A) to the plateau islands (C) stages, the way in which peat plateaus generate runoff changes dramatically, with direct consequences on their runoff pattern and rate. For each stage, water (snowmelt or rainfall) arriving in the channel fen is conducted directly to the basin outlet. Likewise, water arriving on a plateau but not within a bog catchment (*i.e.* bogshed) is routed directly to the adjacent fen. Water arriving directly into bogs or their bogsheds is prevented from reaching channel fens in stage A, but can reach the latter in stage B depending upon the degree of hydrological connectivity in the bog cascades. Activation of secondary runoff therefore increases the amount of runoff between stages A to B. Primary runoff may also increase between these two stages since the fragmentation of plateaus increase can increase the length of the overall plateau-fen edge. Water arriving onto plateaus in stage C is neither stored nor routed as secondary runoff through bog cascades and as such this stage provides the most direct runoff response. However, stage C has the lowest plateau runoff since it is capable only of generating primary runoff, and this runoff is generated from the relatively small total surface area of the remaining plateaus.

Acknowledgments

We wish to thank the Natural Sciences and Engineering Research Council of Canada (NSERC) and the Dehcho First Nation, Liidlii Kue First Nation and the Jean Marie River First Nation for their continued support of the Scotty Creek Research Station (SCRS).

References

- Connon, R., Quinton, W., Hayashi M. & Craig, J. 2014. The effect of permafrost thaw on rising stream flows in the lower Liard River valley, NWT, Canada. *Hydrological Processes*. pp. 4163–4178. DOI: 10.1002/hyp.10206
- Connon, R., Quinton, W., Craig, J., Hanisch, J., Sonnentag, O. 2015. The hydrology of interconnected bog complexes in discontinuous permafrost terrains. *Hydrological Processes*, DOI: 10.1002/hyp.10604.
- Helbig M., Wischniewski K., Kljun N., Chasmer L., Quinton W., Detto M., Sonnentag, O. 2016. Regional atmospheric cooling and wetting effect of permafrost thaw-induced boreal forest loss. *Global Change Biology*, doi:10.1111/gcb.13348.



First insights in bacteria diversity in headwaters emerging from Alpine rock glaciers.

Monica Tolotti¹
Davide Albanese¹
Leonardo Cerasino¹
Claudio Donati¹
Massimo Pindo¹
Michela Rogora²
Roberto Seppi³

¹ *Edmund Mach Foundation, Via E. Mach 1, S. Michele all'Adige, Italy email: monica.tolotti@fmach.it*

² *CNR Institute of Ecosystem Study (ISE), Largo Tonolli 50, Verbania-Pallanza, Italy*

³ *Department of Earth and Environmental Sciences, University of Pavia, Via Ferrata 1, Pavia, Italy*

Abstract

Global warming exerts particularly pronounced effects on the European Alps. As the thawing rates of mountain permafrost ice is lower than for glacier ice, a shift from glacial/periglacial to paraglacial/periglacial dynamics is predicted for Alpine landscapes during the 21st century in relation to deglaciation. Poor knowledge exists on chemical and biological features of waters emerging from Alpine rock glaciers. A set of glacial- or permafrost-fed headwaters was investigated in the Eastern Italian Alps, aiming at exploring bacterial community composition and diversity in epilithic biofilm and sediments. Bacterial assemblages show significant differences according to water and sample type, and to catchment geology. Rock glacier-fed waters show enhanced conductivity and trace element concentrations, and their highly diverse bacterial assemblages significantly differ only from those of glacial streams. Further research will better outline the role of environmental features in modulating bacterial diversity of Alpine headwaters affected by progressing deglaciation.

Keywords: Alpine permafrost, glaciers, water chemistry, bacterial finger-printing, biofilm, surface sediment.

Introduction and Methods

Glacier retreat is a major effect of current global warming and 80-100% of the Alpine glaciers is predicted to vanish in the next few decades (Zemp *et al.*, 2006). As the thawing rate of permafrost ice is 10-100 times lower than for glacier ice, more subsurface permafrost ice will remain than surface glacier ice, and a shift from “glacial/periglacial to paraglacial/periglacial dynamics” is predicted for mountain landscapes in the next few decades (Haeberli *et al.*, 2017). Although rock glaciers (RG) are a common landform of mountain permafrost, both chemical and biological features of waters emerging from them are still poorly known (Thies *et al.*, 2013).

This work aims at characterizing the bacterial diversity in biofilm and sediments of Alpine headwaters directly affected by active RGs, and at exploring possible differences respect to headwaters of different origin. A headwater set (2027-2900 m a.s.l.) was surveyed in autumn 2016 (during base-flow conditions) in three metamorphic catchments of the Eastern Italian Alps

(EIA, Table 1). The water samples were analyzed for temperature, turbidity, pH, major ions, nutrients, and trace elements. Environmental DNA from epilithic biofilm (EPI), surface and deep sediment (SS: 0-2 cm depth, SD: ~5-10 cm) was extracted and analyzed by high throughput sequencing (MiSEQ Illumina) using the specific variable region V4 of 16S rRNA gene. Bioinformatic analyses were performed using the MICCA pipeline (Albanese *et al.*, 2015).

Table 1. Location, dominant geology, and number of headwaters sampled in the EIA in autumn 2016.

Range	Sub-catchment	Geology	nGL	nREF	nRG
Ortler	SU	Sc, Gn	2	0	2
Cevedale	MR	Gn, Sc	1	2	4
Presanella	AM	Gr	1	1	3

SU, MR, AM: Sulden, la Mare, Amola Valley, resp.: Sc, Gn, Gr: scists, orthogneiss, granite, resp. nGL, nREF, nRG: number of glacier-, rock glacier- and mainly precipitation-fed waters, resp.

Results and Discussion

RG-fed headwaters in MR and SU stand out for their low water temperature ($\leq 1^\circ\text{C}$), low turbidity (< 10 NTU) and higher electrical conductivity ($118\text{--}516 \mu\text{S cm}^{-1}$ 20°C) with respect to GL and REF waters in the same catchments (means 26 and $106 \mu\text{S cm}^{-1}$, respectively). All AM waters show very low conductivity ($11\text{--}19 \mu\text{S cm}^{-1}$) in relation to the granitic bedrock. All waters are poor in reactive P ($2\text{--}5 \mu\text{g L}^{-1}$), while $\text{NO}_3\text{--N}$ and SiO_2 are very low in the GL waters ($< 100 \mu\text{g L}^{-1}$ and $< 1 \text{mg L}^{-1}$, resp.). All GL streams show high levels of total P ($70\text{--}428 \mu\text{g L}^{-1}$) and N (up to $\sim 4 \text{mg L}^{-1}$), and varying levels of Fe ($17\text{--}250 \mu\text{g L}^{-1}$) and Al ($19\text{--}255 \mu\text{g L}^{-1}$). RG waters of MR and SU are enriched in Sr ($82\text{--}315 \mu\text{g L}^{-1}$), Ni ($12\text{--}60 \mu\text{g L}^{-1}$), As ($6\text{--}31 \mu\text{g L}^{-1}$).

The α -diversity of the bacterial assemblages in terms of number of observed OTUs and Shannon index (Fig. 1a-b, respectively) is much higher in both the SD and SS samples of the RG and REF streams. On the contrary, the epilithic samples do not show significant differences in bacterial diversity. The first three principal coordinates (PCo) based on weighted UniFrac distances outline significant differences (Wilcoxon rank-sum test with Bonferroni correction, $p < 0.001$) in 16S bacterial composition according to substrate type (PCo1), water origin (PCo2), and, to less extent, geographical location (PCo3, Fig. 1c).

The GL bacterial peculiarity is due to the co-dominance of Proteobacteria and Actinobacteria, followed by Bacteroidetes. Acidobacteria replace the last two phyla in RG samples. Epilithic samples from all water types show higher abundance in Cyanobacteria, while the geographical separation only produces rearrangements in the abundances of a few ubiquitous major phyla. Preliminary correlation analyses revealed significant relations between the abundance of several bacteria taxa and water turbidity, $\text{NO}_3\text{--N}$, SiO_2 , and metal concentrations.

The absence of significant differences between bacterial assemblages of RG-fed and mainly precipitation-fed REF waters suggests that chemical traits of RG-fed waters are not sufficient to select specific bacterial assemblages. In addition, further environmental variables need to be considered in future investigations of Alpine headwaters affected by permafrost degradation.

Acknowledgments

The research was financially supported by the Edmund Mach Foundation. A special thank goes to

Stefano Brighenti for his precious help during the field work.

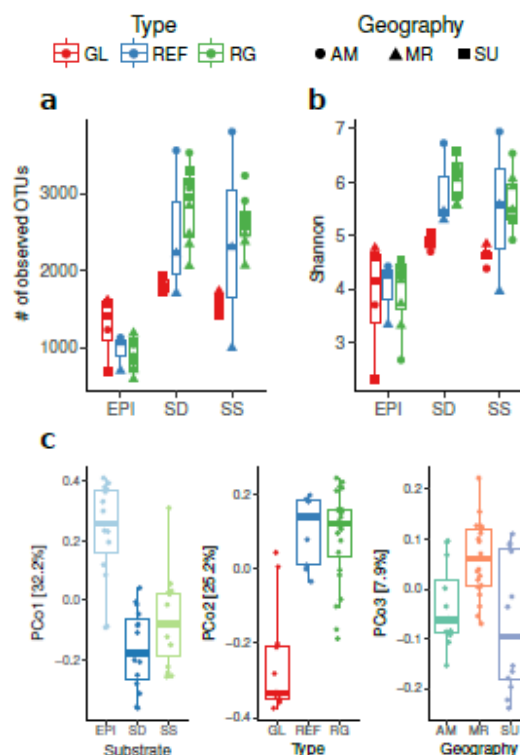


Figure 1. Number of observed bacterial OTUs (a) and Shannon Index values (b) in the sample collected from the headwater studied. (c) The first three principal coordinates (PCo) based on the weighted UniFrac distances outline differences in 16S bacterial composition between different substrates, water types, and sampling sites. Abbreviations as in Table 1.

References

- Albanese, D., Fontana, P., De Filippo, C., Cavalieri, D. & Donati, C., 2015. MICCA: a complete and accurate software for taxonomic profiling of metagenomics data. *Scientific Reports* 5:9743.
- Haeberli, W., Schaub, Y. & Huggel, C., 2017. Increasing risks related to landslides from degrading permafrost into new lakes in de-glaciating mountain ranges. *Geomorphology* 293: 405-417.
- Thies, H., Nickus, U., Tolotti, M., Tessadri, R. & Krainer, K., 2013. Evidence of rock glacier melt impacts on water chemistry and diatoms in high mountain streams. *Cold Regions Science and Technology* 96: 77-85.
- Zemp, M., Haeberli, W., Hoelzle, M. & Paul, F., 2006. Alpine glaciers to disappear within decades? *Geophysical Resources Letters* 33: 1-4.

Author Index

- çiner Attila, 662, 663
łopuch Michał, 575, 576
øverli Eriksen Harald, 414, 415
šmejkalová Tereza, 52, 53
žebre Manja, 662, 663
- Aalberg Arne, 839, 840
Aalstad Kristoffer, 91, 92
Aalto Tuula, 691, 692
Aanderud Zachary, 327, 328
Aas Kjetil, 683, 684, 704
Abbott Benjamin, 271, 272, 317, 318, 327, 328, 784, 785
Abedian Amiri Erfan, 265, 266
Abramov Andrey, 549, 550
Adiya Saruulzaya, 136, 137
Afanasyeva Anna, 751, 752
Afonin Alexey, 289, 290
Agapkin Ivan, 867, 868
Agnan Yannick, 319, 320
Aigner Lukas, 880, 881
Ajo-Franklin Jonathan, 825, 826, 841, 842
Aksnes Jostein, 859, 860
Albanese Davide, 1038, 1039
Alberto Walter, 537, 538
Aleksееva Tatiana, 804, 805
Aleksytina Daria, 800, 801
Aleksyutina Daria, 37, 193, 194, 792, 793
Alexis Marie, 319, 320
Allard Michel, 279, 280, 631, 632
Allen Simon, 922, 923
Alonso-González Esteban, 992, 993
Altena Bas, 91, 92
Alvarado Joaquin, 739
Alvarado Petersen Voltaire, 253, 254
Amann Benjamin, 105, 106, 627, 628
Amanzhurov Ruslan, 37, 97, 98
Amesbury Matthew, 711, 712, 719, 720
Amiri Erfan, 1018, 1019
Amschwand Dominik, 376, 377
Ananyev Vasiliy, 170, 171
Anders Katharina, 38, 39
Anderson Darya, 740, 741
Anderson N.j., 372, 373
Andrés Nuria, 662, 663
Andreeva Varvara, 609, 610
Andreoli Andrea, 269, 270, 501, 502
Angelopoulos Michael, 761, 762
Anschutz Helgard, 882, 883
Antoine Carriot, 845, 846
Ardelean Florina, 593, 594, 863, 864
Arefyev Stanislav, 267, 268
Arenson Lukas, 1002, 1003
Arndt Sandra, 764, 765
Arora Bhavna, 1016, 1017
Arp Christopher, 56, 57, 307, 308, 360, 361
Ashastina Kseniia, 629, 630, 664, 665
Audry Stéphane, 435, 436
Aune Vetle, 378, 379
Avey Colin, 81, 82
Axelsson Pia, 713, 714
- Baatarbileg Nachin, 281, 282
Babkin Evgenii, 685, 686
Babkin Evgeny, 325, 326
Babkina Elena, 283, 284, 551, 552, 685, 686
Badetz Christian, 480, 481
Badoux Vincent, 952, 953
Bai Ruiqiang, 431, 432
Baillet Laurent, 394, 395
Baker Michelle, 317, 318
Balks Megan, 553, 554
Balme Matt, 509, 510
Balme Matthew, 525, 526
Baltzer Agnès, 794, 795
Baltzer Jennifer, 309, 310
Bancheva Alexandra, 742
Baral Prashant, 40, 41
Baranskaya Alisa, 193, 194, 790–793, 861, 862
Barboux Chloé, 380, 381, 392, 393
Baroni Carlo, 408, 409
Barret Maïalen, 695, 696
Barth Johannes, 1012, 1013
Bartsch Annett, 42, 43, 46, 47, 65, 66, 85, 86, 591, 592, 691, 692
Bas Bertan, 233, 234
Basharin Nikolay, 476, 477
Bashkova Ekaterina, 285, 286
Basiliko Nathan, 701, 702
Baumann Sabine, 44, 45
Baumhauer Roland, 89, 90
Bazhin Kirill, 890, 891, 900, 901, 1030, 1031
Bazhina Natalia, 633, 634
Beddoe Ryley, 1032, 1033

Beel Casey, 348, 349, 1004
 Beermann Fabian, 784, 785
 Bek Dina, 170, 171
 Bellehumeur-Genier Olivier, 581, 582
 Belonosov Andrei, 287, 288
 Belova Nataliya, 37, 193, 194, 666, 667, 790–793, 808, 809
 Ben-Yehoshua Daniel, 535, 536
 Bendixen Mette, 802, 803
 Bense Victor, 448, 449, 589, 590
 Berdnikov Nikolay, 565, 566
 Bergstedt Helena, 46, 47
 Bernardo Ivo, 875–877
 Berntsen Terje, 683, 684
 Berthling Ivar, 414, 415
 Bertino Laurent, 91, 92
 Bertoldi Walter, 1008, 1009
 Bertone Aldo, 382, 383
 Bertouille Nathan, 333, 334, 346, 347
 Bertran Pascal, 118, 119
 Beutel Jan, 944, 945, 958, 959
 Beutner Katharina, 839, 840
 Bevington Alexandre, 581, 582
 Bhiry Najat, 503, 504, 687, 688
 Biasi Christina, 691, 692, 784, 785
 Binal Adil, 233, 234
 Binbin He, 452, 453
 Biraud Sébastien, 1016, 1017
 Biskaborn Boris, 579, 580
 Blöthe Jan, 384, 385, 886, 887
 Bloss Benjamin, 896, 897
 Blum Joel, 323, 324
 Bobrik Anna, 342, 343
 Bobrova Olga, 344, 345
 Bodin Xavier, 386, 387, 392, 393, 406, 407, 615, 616, 662, 663, 932, 933, 980, 981
 Boike Julia, 38, 39, 91, 92, 299, 300, 344, 345, 360, 361, 487, 488, 521, 522, 579, 580, 691, 692
 Bolch Tobias, 48, 49
 Bonnaventure Philip, 291, 292, 561, 562, 948, 949
 Bonnefoy-Demongeot Mylène, 615, 616
 Bouchard Frédéric, 474, 475, 743, 744
 Bouley Sylvain, 725, 726
 Bouquety Axel, 725, 726
 Bourriquen Marine, 794, 795
 Bowden William, 327, 328
 Boyko Alexey, 816
 Bröder Lisa, 321, 322, 335, 336
 Brardinoni Francesco, 120, 121, 388, 389
 Bratsch Jennifer, 806, 807
 Braverman Michael, 1005–1007, 1036, 1037
 Brenguier Ombeline, 406, 407
 Brenning Alexander, 392, 393
 Brighenti Stefano, 1008, 1009, 1020, 1021
 Brovkin Victor, 764, 765
 Brown Dana, 896, 897
 Brown Kristina, 751, 752
 Brun Jean-Jacques, 853, 854
 Bruno Maria Cristina, 1008, 1009, 1020, 1021
 Brushkov Anatoly, 142, 143
 Brynjólfsson Sveinn, 77, 78
 Brynjólfsson Skafti, 77, 78
 Budantseva Nadine, 130–133, 666, 667, 689, 690
 Bukhanov Boris, 418, 419, 480, 481
 Buldovich Sergey, 97, 98, 800, 801
 Bullard J.e., 372, 373
 Burn Christopher, 555, 556
 Burn Chritopher, 138, 139
 Busey Robert, 54, 55
 Busmann Ingeborg, 325, 326
 Butcher Frances, 525, 526
 Buter Anuschka, 269, 270
 Buzard Richard, 796, 797
 Bychkov Andrey, 97, 98
 Bykova Svetlana, 358, 359
 Côté Jean, 437, 438, 859, 860
 Cabrol Léa, 695, 696
 Caduff Rafael, 380, 381
 Callegari Mattia, 382, 383
 Calmels Fabrice, 138, 139, 172, 173, 637, 638, 753, 754
 Cannone Nicoletta, 670
 Carey Sean, 1010, 1011
 Carshalton Annette, 553, 554
 Carton Alberto, 408, 409
 Carturan Luca, 408, 409
 Cassis Team And The, 735, 736
 Castaings William, 980, 981
 Castrec-Rouelle Maryse, 319, 320
 Castro Miguel, 52, 53
 Cerasino Leonardo, 1038, 1039
 Chadburn Sarah, 275, 276, 691, 692
 Changyang Zhang, 443, 444
 Charman Dan, 719, 720
 Chen Jie, 50, 51
 Chen Leiyi, 271, 272
 Chen Lin, 621, 622
 Cherbunina Maria, 97, 98
 Cherepanov Artem, 184, 185, 869, 870
 Chesnokova Irina, 140, 141, 605, 606

Chetverova Antonina, 344, 345
 Chi Guangqing, 221, 222
 Chiarle Marta, 527, 528, 922, 923, 938, 939
 Chiasson Alexandre, 631, 632
 Chizhova Julia, 689, 690
 Choler Philippe, 857, 858
 Choy Emily, 751, 752
 Christensen Jens, 766, 767
 Christiansen Casper, 693, 694
 Christiansen Hanne, 79, 80, 261, 262, 356, 357, 468, 469
 Christiansen Hanne Hvidtfeldt, 241, 242, 456, 457
 Christl Marcus, 376, 377
 Christoph Müller, 295, 296
 Christophe Grenier, 595, 596
 Chuvilin Evgenii, 287, 288
 Chuvilin Evgeny, 97, 98, 418, 419, 480, 481
 Chwatal Werner, 906, 907, 978, 979
 Cicoira Alessandro, 390, 391
 Cleall Peter, 69, 70
 Coch Caroline, 249, 250, 360, 361
 Cochand Marion, 420, 421, 1012, 1013
 Cohen Denis, 99, 100
 Cola Giuseppe, 120, 121
 Coles Anna, 1014, 1015
 Colucci Renato, 662, 663
 Comiti Francesco, 269, 270, 398, 399, 501, 502, 1008, 1009, 1020, 1021
 Comyn-Platt Edward, 691, 692
 Cong Ding, 235
 Conley Daniel, 346, 347
 Cannon Ryan, 1014, 1015, 1018, 1019, 1036, 1037
 Conway Susan, 509, 510, 525, 526, 535, 536, 727, 728
 Coon Ethan, 717, 718
 Coppa Graziano, 527, 528, 831, 832
 Corner Geoffrey, 414, 415
 Costa Stéphane, 794, 795
 Costard François, 424, 425
 Costard Francois, 474, 475, 493, 494, 545, 546, 725, 726, 731, 732, 1022, 1023
 Cottingham Samuel, 317, 318
 Coviello Velio, 501, 502
 Craig James, 265, 266, 1018, 1019, 1036, 1037
 Creber Sarah, 1032, 1033
 Cremonese Edoardo, 940, 941
 Cremonese Gabriele, 735, 736
 Croft Peppi, 207, 208
 Cuzzo Giovanni, 382, 383
 Czekirda Justyna, 950, 951
 Daanen Ronnie, 896, 897
 Dabbs Austin, 557, 558
 Dafflon Baptiste, 1016, 1017
 Dagenais Sophie, 420, 421
 Dalban Canassy Pierre, 952, 953
 Danilov Kencheeri, 890, 891, 900, 901
 Darrow Margaret, 207, 208
 Dashtseren Avirmed, 281, 282
 Davlitschina Dinara, 418, 419
 Davydova Anya, 321, 322
 De Pablo Miguel Angel, 597, 598
 Dean Joshua, 317, 318
 Debolskiy Matvey, 559, 560
 Decaulne Armelle, 493, 494, 503, 504
 Decaunle Armelle, 535, 536
 Delaloye Reynald, 380, 381, 392, 393, 412, 413, 462, 463, 511, 512, 517, 518, 543, 544, 966, 967
 Deline Philip, 940, 941, 958, 959
 Dematteis Niccolò, 382, 383
 Denis-Didier Rousseau, 113–115
 Dereviagin Alexander, 656, 657
 Dergacheva Mariya, 633, 634
 Desyatkin Alexey, 476, 477
 Desyatkin Roman, 476, 477
 Devoie Elise, 265, 266, 1018, 1019, 1036, 1037
 Dierking Wolfgang, 89, 90
 Dixon Gavin, 211, 212
 Dobiński Wojciech, 954, 955
 Dobrynin Dmitriy, 489, 490
 Dolman Han, 691, 692
 Donati Claudio, 1038, 1039
 Dongqing Li, 422, 423
 Doré Guy, 138, 139, 172, 173, 182, 183, 859, 860
 Dou Shan, 825, 826
 Douglas Thomas, 309, 310, 323, 324
 Draebing Daniel, 505–508
 Drage Jeremiah, 207, 208
 Drevon Joseph, 845, 846
 Drozdov Dmitry, 142, 143, 565, 566
 Dubrovin Vladimir, 142, 143
 Dudarev Oleg, 654, 655, 770, 771
 Dugarjav Chultem, 705, 706
 Duguay Maxime, 581, 582
 Dunning Stuart, 523, 524
 Dupeyrat Laure, 424, 425, 545, 546
 Duvillard Pierre-Allain, 871, 872, 934, 935, 940, 941
 Dvornikov Yury, 42, 43, 61, 62, 283, 284, 325, 326, 360, 361, 658, 659, 685, 686

Ebel Brian, 445, 896, 897
 Echelard Thomas, 386, 387
 Education And Outreach Committee Members,
 261, 262, 757, 758
 Egholm David, 988, 989
 Eglinton Timothy, 321, 322, 335, 336
 Egorov Igor, 817, 818
 Eichel Jana, 507, 508
 Eiken Trond, 378, 379
 Eingel Michael, 501, 502
 Ekblaw Ian, 825, 826
 Ekici Altug, 176, 177, 273, 274
 Elashvili Mikheil, 942, 943
 Eleanor Burke, 275, 276, 691, 692
 Elger Kirsten, 65, 66
 Eling Christian, 507, 508
 Emerich Souza Priscila, 802, 803
 Emmert Adrian, 873, 874
 Emond Abraham, 896, 897
 Engel Michael, 1008, 1009, 1020, 1021
 Engel Zbynek, 878, 879
 Erikson Li, 798, 799
 Ermokhina Ksenia, 42, 43
 Etzelmüller Bernd, 91, 92, 378, 379, 460, 461,
 466, 467, 704, 713, 714, 926, 927, 950,
 951, 974, 975
 Etzelmuller Bernd, 458, 459
 Eulenburg Antje, 344, 345
 Evgrafova Alevtina, 751, 752
 Evgrafova Svetlana, 277, 278
 Evlanov Dmitri, 144, 145
 Ewertowski Marek, 101, 102, 539, 540
 Ewing Stephanie, 317, 318

 Fage Alexey, 912, 913
 Faillettaz Jérôme, 944, 945
 Faillettaz Jerome, 390, 391
 Fan Yuanchao, 176, 177, 691, 692
 Farinotti Daniel, 404, 405
 Farnsworth Wesley, 468, 469
 Farquharson Louise, 221, 222, 796, 797
 Farzamian Mohammad, 875–877
 Fedorov Alexander, 476, 477, 493, 494, 545,
 546, 595, 596, 900, 901, 1022, 1023
 Fedorova Irina, 344, 345
 Feldman Mor, 356, 357
 Fernández Hans, 255, 256
 Fernández Jesús, 635, 636
 Fernández Susana, 670
 Fernandes Marcelo, 635, 636, 652, 653
 Fernandez Navarro Hans, 253, 254, 986, 987
 Fiddes Joel, 91, 92, 956, 957
 Filip Hrbacek, 301, 302, 878, 879
 Finance François, 615, 616
 Fischer Urs, 99, 100
 Fitzsimmons Kathryn, 113–115
 Flavien Vernier, 980, 981
 Flores-Orozco Adrian, 880, 881, 906, 907, 978,
 979
 Fochesatto Javier, 821, 822
 Foged Niels, 156, 157
 Ford James, 740, 741
 Fortier Daniel, 474, 475, 637, 638
 Fortier Richard, 420, 421, 426, 427, 1012, 1013
 Fournier Jérôme, 794, 795
 Franceschi Michel, 118, 119
 Frankl Amaury, 511, 512
 Frappier Roxanne, 639, 640
 Fraser Rob, 339, 340
 Frauenfelder Regula, 882, 883
 Frehner Marcel, 376, 377
 Frei Rebecca, 327, 328
 Frey Holger, 922, 923
 Friborg Thomas, 691, 692
 Fritz Michael, 329, 330, 341, 360, 361, 366, 367,
 679, 680
 Froese Duane, 637, 638
 Frolov Denis, 563, 564
 Fuchs Matthias, 485, 486, 569, 570, 774–777,
 780, 781, 784, 785
 Fujun Niu, 225, 226

 Günther Frank, 50, 51, 478, 479, 495, 496, 569,
 570
 Gómez-Lende Manuel, 992, 993
 Głowacki Tadeusz, 575, 576
 Gachev Emil, 593, 594
 Gagnon Samuel, 279, 280
 Galeeva Elmira, 146, 147
 Gallego-Sala Angela, 719, 720
 Gandois Laure, 362, 363, 695, 696
 Gansukh Tsogt-Erdene, 136, 137
 Gao Jianqiang, 431, 432
 Gao Yao, 691, 692
 Gaochen Sun, 235
 García-Hernández Cristina, 641, 642, 662, 663,
 670
 Garcia Juan Luis, 986, 987
 Garibaldi Madeleine, 561, 562
 Garneau Michelle, 711, 712
 Gautier Emmanuele, 424, 425, 1022, 1023
 Gedney Nicola, 691, 692
 Geertsema Marten, 922, 923
 Gelvin Arthur, 825, 826, 841, 842

Gerardo Nieto Oscar Alexandro, 695, 696
 Giaccone Elisa, 960, 961
 Gibbs Ann, 798, 799
 Gibson Carolyn, 309, 310
 Gilbert Graham, 468, 469
 Gisnås Kjersti Gleditsch, 882, 883
 Glushkova Nadezhda, 495, 496
 Goeckede Mathias, 352, 353
 Goetz Jason, 932, 933
 Golubev Vladimir, 563, 564
 Gonçalves-Araujo Rafael, 329, 330
 Goncharova Olga, 342, 343, 715, 716
 González-García María, 992, 993
 Gordiychuk Vladimir, 144, 145, 148, 149
 Gordon Richard, 751, 752
 Goreyavcheva Anastasya, 884, 885
 Gorshkov Evgeny, 97, 98
 Gosse John, 926, 927
 Gosselin Gabriel, 699, 700
 Gotsiridze George, 942, 943
 Goyanes Gabriel, 599, 600
 Grandmont Katherine, 753, 754
 Gravis Andrey, 342, 343, 565, 566
 Grebenets Valery, 160–163, 213, 214, 243, 244,
 259, 260, 285, 286, 567, 568, 573, 574
 Grebenkin Sergey, 418, 419
 Green Eric, 174, 175
 Green Erik, 480, 481
 Grenier Christophe, 331, 332, 426–429, 435, 436,
 474, 475, 493, 494, 900, 901
 Gribovskii Gleb, 144, 145, 150, 151
 Grigorevskaya Alina, 912, 913
 Grigoriev Mikhail, 579, 580, 761–763
 Grimm Robert, 908, 909
 Grootjans Ab, 705, 706
 Grosse Guido, 50, 51, 56, 57, 65, 66, 299, 300,
 346, 347, 360, 361, 478, 479, 485–488,
 495, 496, 569, 570, 761, 762, 774–777,
 780, 781, 784, 785
 Gruber Stephan, 908, 909, 996, 997
 Gubin Stanislav, 358, 359, 804, 805
 Guggenberger Georg, 277, 278
 Guglielmin Mauro, 662, 663, 670, 831, 832
 Guillaso Stéphane, 83, 84
 Guillemot Antoine, 394, 395
 Guillet Grégoire, 940, 941, 958, 959
 Gunar Aleksey, 97, 98
 Guo Ming, 621, 622
 Guoyu Li, 225, 226
 Gustafsson örjan, 654, 655, 770, 771
 Haas Antonie, 65, 66
 Habeck Joachim Otto, 751, 752
 Haberkorn Anna, 962, 963
 Hadhri Hela, 980, 981
 Haeberli Wilfried, 99, 100, 466, 467, 922–925
 Haghipour Negar, 321, 322, 335, 336
 Hagin Christian, 380, 381
 Hales Tristram, 69, 70
 Halla Christian, 384, 385, 886, 887, 994, 995
 Halvorsen Kathleen, 221, 222
 Hancock Bronwyn, 753, 754
 Hanson Teresa, 745, 746
 Haq M. Anul, 40, 41
 Harada Koichiro, 245, 246
 Harlavan Yehudit, 356, 357
 Harrington Jordan, 964, 965, 1002, 1003
 Harris Stuart, 847, 848
 Hartl Lea, 392, 393
 Hartmann Jörg, 63, 64, 441, 442
 Hatté Christine, 331, 332, 474, 475, 695, 696
 Hauber Ernst, 729, 730
 Hauck Christian, 466, 467, 875–877, 886–889,
 898, 899, 966, 967, 984, 985, 998, 999
 Hayashi Masaki, 964, 965
 Hayman Garry, 691, 692
 Haynes Kristine, 1036, 1037
 Heckmann Tobias, 269, 270
 Heim Birgit, 65, 66, 325, 326, 329, 330, 344,
 345
 Heimann Martin, 352, 353
 Heinrich Georg, 906, 907
 Helbig Manuel, 699, 700
 Helgason Jón Kristinn, 509, 510, 525, 526
 Helm Veit, 38, 39
 Helmstetter Agnès, 394, 395
 Hendrickx Hanne, 511, 512
 Henning Theresa, 478, 479
 Hermanns Reginald, 926, 927, 974, 975
 Hermanutz Luise, 291, 292
 Herzsuh Ulrike, 360, 361
 Hess Joseph, 211, 212
 Hickman Jennifer, 1024, 1025
 Hilbich Christin, 462, 463, 466, 467, 880, 881,
 888, 889, 898, 899, 966, 967
 Hildebrandt Anke, 352, 353
 Hilger Paula, 926, 927, 974, 975
 Hillier John, 525, 526
 Hindberg Heidi, 414, 415
 Hinzman Alexa, 1026, 1027
 Hirmand M. Reza, 265, 266
 Hirst Catherine, 333, 334, 346, 347
 Hoefle Bernhard, 38, 39

Hoelzle Martin, 404, 405, 462, 463, 466, 467, 962, 963
 Hoff Inge, 437, 438, 859, 860
 Holland Kira, 666, 667
 Holloway Jean, 309, 310, 697, 698
 Holmes Robert, 317, 318
 Holmlund Per, 460, 461
 Homma Shota, 152, 153
 Horn Marcus, 784, 785
 Hoyt Alison, 695, 696
 Hrbáček Filip, 519, 520, 670
 Hsieh Entzu, 154, 155
 Hu Yan, 392, 393, 513, 514
 Huang Yadong, 430
 Hubbard Susan, 1016, 1017
 Huc Stéphanie, 849, 850
 Hugelius Gustaf, 691, 692
 Huggel Christian, 922, 923
 Hughes Philip, 662, 663
 Huissteden Ko J., 87
 Hurault Benoit, 424, 425

 Iannuci Frances, 327, 328
 Iijima Yoshihiro, 281, 282
 Ikeda Atsushi, 392, 393
 Ilyashuk Boris, 643–646
 Ilyashuk Elena, 643–646
 Ingólfsson Ólafur, 535, 536
 Ingeman-Nielsen Thomas, 156, 157, 910, 911
 Instanes Arne, 191, 192
 Iqulak Debbie, 348, 349
 Irrgang Anna, 533, 534
 Isaev Oleg, 158, 159
 Isaev Vladislav, 247, 248, 800, 801
 Isakov Vladimir, 160–163
 Isakova Daria, 162, 163
 Isaksen Ketil, 414, 415, 458–461, 464–467, 974, 975
 Ishikawa Mamoru, 281, 282
 Istomin Vladimir, 480, 481
 Istratov Vyacheslav, 184, 185
 Ivanov Yuri, 918, 919
 Ivy-Ochs Susan, 376, 377
 Iwahana Go, 54, 55, 245, 246
 Iwamoto Taichi, 164, 165

 Jóhannesson Tómas, 950, 951
 Jónsson Arni, 882, 883
 Jacobi Stephan, 58, 59, 305, 306, 521, 522
 Jacobs Benjamin, 505, 506, 928, 929
 Jakobsson Martin, 654, 655
 Jambaljav Yamkhin, 281, 282, 705, 706
 James Stephanie, 825, 826
 Jamie Woodward, 662, 663
 Jammet Mathilde, 691, 692
 Jan Ahmad, 717, 718
 Jansson Peter, 460, 461
 Jaskólski Marek, 810, 811
 Jewell Richard, 215, 216
 Ji Duoying, 968, 969
 Jiang Huiru, 571, 572
 Jianguo Lu, 219, 220
 Jianming Zhang, 235
 Jichun Wu, 452, 453
 Jiménez Juan Javier, 597, 598
 Jin Huijun, 589, 590, 972, 973
 Jing Luo, 189, 190
 Joß Hanna, 770, 771
 Jones Benjamin, 56, 57, 221, 222, 360, 361, 485–488, 569, 570, 774, 775, 796–799
 Jong Dirk, 335, 336
 Jongejans Loeka, 774–777
 Jordan Colm, 525, 526
 Jorgenson Torre, 647–649
 Juhls Bennet, 63, 64, 761–763
 Julien Fouché, 368, 369, 699, 700

 Kääb Andreas, 591, 592
 Kňažková Michaela, 301, 302, 519, 520
 Křížek Marek, 103, 104, 128, 129
 Kaiser Soraya, 58, 59, 305, 306, 521, 522
 Kalinicheva Svetlana, 60
 Kalinin Pavel, 804, 805
 Kamnev Yaroslav, 573, 574
 Kampova Barbora, 301, 302
 Kanevskiy Mikhail, 207, 208, 647–649
 Kanie Shunji, 152, 153, 164, 165, 203, 204, 231, 232
 Kapralova Veronika, 482–484
 Kasprzak Leszek, 101, 102
 Kasprzak Marek, 575, 576, 810, 811
 Kass Andy, 896, 897
 Kasymuskaya Maria, 819, 820
 Kattenborn Teja, 507, 508
 Kaufmann Viktor, 392, 393
 Kavan Jan, 878, 879
 Kaverin Dmitry, 577, 578
 Keim Dawn, 619, 620
 Kellerer-Pirklbauer Andreas, 392, 393, 396, 397
 Kenner Robert, 962, 963, 970, 971
 Kerimov Aligoushad, 160, 161, 567, 568
 Kerimov Aligyushad, 166, 167
 Keskitalo Kirsi, 337, 338
 Keuschnig Markus, 833, 834

Khairedinova Aleksandra, 243, 244, 251, 252
 Khairullin Rustam, 685, 686
 Khilimonyuk Vanda, 97, 98
 Khimenkov Alexander, 168, 169
 Kholodov Alexander, 557, 558, 609, 610, 745, 746, 821, 822
 Khomutov Artem, 42, 43, 61, 62, 267, 268, 283, 284, 325, 326, 551, 552, 658, 659, 685, 686
 Khristoforov Ivan, 890, 891, 900, 901, 1030, 1031
 Kienast Frank, 629, 630, 650, 651
 Kijowski Andrzej, 101, 102
 Kirk Jane, 348, 349
 Kirkwood Adam, 701, 702
 Kiro Yael, 356, 357
 Kizyakov Alexander, 61, 62, 251, 252, 325, 326, 478, 479, 658, 659
 Kjellman Sofia, 713, 714
 Klene Anna, 607, 608, 837, 838
 Klingbeil Lasse, 507, 508
 Klukin Yuri, 835, 836
 Knazkova Michaela, 878, 879
 Kneier Fabian, 579, 580
 Kneisel Christof, 89, 90, 851, 852, 873, 874, 892, 893
 Knoblauch Christian, 786, 787
 Kofler Christian, 398, 399
 Kohnert Katrin, 63, 64, 249, 250, 441, 442
 Koinig Karin, 643–646
 Kokelj Shawne, 1014, 1015
 Kokelj Steve, 81, 82, 339, 340
 Kokelj Steven, 309, 310, 364, 365, 587, 588
 Kokin Osip, 193, 194
 Kokoszka Justin, 81, 82, 339, 340
 Kolehmainen Jaana, 317, 318
 Komarov Ilya, 170, 171
 Komarov Oleg, 247, 248
 Kong Xiangbing, 172, 173
 Konstantinov Pavel, 476, 477, 595, 596, 900, 901
 Kooi Henk, 356, 357
 Kormshchikov Denis, 439, 440
 Korneeva Yana, 747, 748
 Korostelev Yury, 583, 584
 Kortelainen Pirkko, 317, 318
 Koshurnikov Andrey, 247, 248, 800, 801, 867, 868
 Kostenkov Nikita, 285, 286
 Kostina Anastasiya, 195, 196
 Kotov Pavel, 97, 98, 174, 175, 839, 840, 867, 868
 Kou Dan, 295, 296, 313, 314
 Kraev Gleb, 287, 288, 585, 586
 Krainer Karl, 382, 383
 Krause David, 103, 104, 128, 129
 Kraushaar Sabine, 823, 824
 Krautblatter Michael, 515, 516, 833, 834, 904, 905, 922, 923, 928–931
 Kristiansen Håvard, 703
 Krivov Denis, 819, 820
 Kroisleitner Christine, 46, 47
 Kronig Olivia, 376, 377
 Kroon Aart, 802, 803
 Krotkov Vasiliy, 251, 252
 Krys Dennis, 817, 818
 Krzewinski Thomas, 211, 212
 Kudryavtsev Anton, 287, 288
 Kuhry Peter, 333, 334, 346, 347
 Kull Isabelle, 942, 943
 Kummert Mario, 517, 518
 Kumpula Timo, 42, 43
 Kunz Julius, 892, 893
 Kurbanov Redzhep, 675, 676
 Kurbatov Aleksey, 213, 214
 Kurbatova Lyubov, 804, 805
 Kurchatova Anna N., 778, 779
 Kuzmina Svetlana, 629, 630
 Kuznetcov Taras, 178, 179
 Kuznetcova Anna, 289, 290
 Kuznetsova Elena, 751, 752
 Kvon Dina, 894, 895, 916, 917
 Kyser Kurt, 105, 106
 L'hérault Emmanuel, 631, 632
 Léger Emmanuel, 1016, 1017
 López-Martínez Jerónimo, 83, 84, 670
 López-Moreno Juan, 992, 993
 La Farge Catherine, 105, 106
 Laboor Sebastian, 65, 66
 Lacelle Denis, 339, 340, 668, 669
 Lachniet Matthew, 666, 667
 Lacroix Pascal, 386, 387
 Lafrenière Melissa, 368, 369
 Lafreniere Melissa, 1028, 1029
 Lai Yuanming, 223, 224, 431–434
 Laio Francesco, 938, 939
 Lambert Fabrice, 986, 987
 Lambiel Christophe, 380, 381, 392, 393, 400, 401, 412, 413, 462, 463, 960, 961
 Lamoureux Scott, 105, 106, 339, 340, 348, 349, 368, 369, 561, 562, 627, 628, 829, 830, 1004, 1028, 1029
 Lang Kathrin, 388, 389

Langer Moritz, 58, 59, 91, 92, 176, 177, 299,
 300, 305, 306, 521, 522, 579, 580
 Lantuit Hugues, 329, 330, 335, 336, 341, 366,
 367, 533, 534, 679, 680, 749, 750, 763
 Lantz Trevor, 81, 82, 339, 340
 Lapalme Caitlin, 291, 292
 Lapka Stephanie, 806, 807
 Lara Mark, 309, 310
 Larose éric, 394, 395
 Larsen Amy, 360, 361
 Larsen Yngvar, 79, 80, 414, 415
 Lashchinskiy Nikolay, 67, 68
 Lauknes Tom, 414, 415
 Lauknes Tom Rune, 79, 80
 Laurent Cyrielle, 753, 754
 Laurent Jean-Paul, 857, 858
 Lavielle Bernard, 118, 119
 Lavoie Martin, 687, 688
 Lawrence David, 273, 274
 Lazizi Laetitia, 857, 858
 Lebedeva Liudmila, 890, 891, 1030, 1031
 Lee Hanna, 176, 177, 273, 274, 691–694
 Lee-Cullin Joseph, 317, 318
 Lefebvre Béatrice, 333, 334, 346, 347
 Lehning Michael, 404, 405, 962, 963
 Leibman Marina, 42, 43, 61, 62, 267, 268, 283,
 284, 293, 294, 325, 326, 551, 552, 658,
 659
 Leinauer Johannes, 928, 929
 Lemieux Chantal, 172, 173
 Lemieux Jean-Michel, 420, 421, 426, 427, 1012,
 1013
 Lenz Josefine, 485, 486, 751, 752, 774–777
 Levin Lev, 195, 196, 835, 836
 Lewkowicz Antoni, 291, 292, 309, 310, 581, 582,
 617, 618, 697, 698, 948, 949
 Li Shuangyang, 223, 224
 Li Xin, 601, 602
 Liebner Susanne, 485, 486, 784, 785
 Lijun Yang, 443, 444
 Likhacheva Emma, 140, 141
 Lilleøren Karianne, 378, 379
 Lillie Karoline, 699, 700
 Lim Michael, 810, 811
 Lin Hui, 50, 51
 Lin Zhanju, 189, 190
 Lindsey Nate, 825, 826
 Lindsey Nathaniel, 841, 842
 Linsbauer Andreas, 924, 925
 Littlefair Cara, 364, 365
 Liu Futing, 271, 272, 317, 318
 Liu Lin, 50, 51, 392, 393, 513, 514
 Liu Minghao, 189, 190
 Liu Weibo, 621, 622
 Liu Yongzhi, 236, 237
 Lohila Annalea, 691, 692
 Loibl David, 521, 522
 Lopes Luís, 635, 636
 Lopes Luis Filipe, 652, 653
 Loranger Benoit, 859, 860
 Loranty Michael, 821, 822
 Lorensen Thomas, 75, 76
 Losert Franziska, 851, 852
 Losiak Ania, 731, 732
 Lu Jianguo, 433, 434
 Lu Yan, 93, 94
 Lubbad Raed, 182, 183
 Lubnina Natalia, 97, 98
 Lucianaz Claudio, 410, 411, 940, 941
 Ludwig Sarah, 609, 610
 Lugovoy Nikolay, 861, 862
 Luino Fabio, 938, 939
 Luo Dongliang, 972, 973
 Lupachev Alexey, 358, 359, 804, 805
 Lussana Cristian, 974, 975
 Lysdahl Asgeir, 882, 883
 Maßmann Jobst, 124, 125
 Machiya Hirokazu, 116, 117
 Madrigal Victor, 535, 536
 Magaly Koch, 83, 84
 Magnin Florence, 924–927, 940, 941, 974, 975
 Magori Brigitte, 593, 594, 863, 864, 976, 977
 Maierhofer Theresa, 880, 881, 906, 907, 978,
 979
 Maio Christopher, 485, 486
 Mair Volkmar, 120, 121, 388, 389, 398, 399
 Makarieva Olga, 1034, 1035
 Makarov Dmitry, 894, 895
 Makarycheva Elizaveta, 178, 179
 Makshaev Radik, 107, 108
 Maksimov Georgii, 609, 610
 Maleeva Anna, 180, 181
 Malenfant-Lepage Julie, 182, 183
 Malet Emmanuel, 980, 981
 Malkova Galina, 583, 584, 613, 614, 902, 903
 Mamot Philipp, 930, 931
 Mangelsdorf Kai, 776, 777
 Mann Daniel, 796, 797
 Mann Paul, 317, 318
 Mao Chao, 295, 296
 Marcer Marco, 392, 393, 406, 407, 845, 846,
 932–935
 Marchenko Mikhail, 916, 917

Marchenko Sergey, 603, 604, 766, 767
 Marchenko Yulia, 918, 919
 Marciniac Kacper, 575, 576
 Mariéthoz Grégoire, 960, 961
 Marin Carlo, 382, 383
 Markov Aleksey, 827, 828
 Marlin Christelle, 474, 475
 Marmo Chiara, 424, 425, 545, 546
 Marquardt Carlos, 986, 987
 Marsh Philip, 81, 82, 619, 620
 Marsy Guilhem, 934, 935, 980, 981
 Marszałek Henryk, 575, 576
 Martín-Moreno Raúl, 992, 993
 Martens Jannik, 654, 655
 Martin Léo, 704
 Martin Leo, 299, 300, 683, 684
 Martinez Cruz Karla, 695, 696
 Marushchak Maija, 691, 692
 Marx Sabrina, 38, 39
 Maschenko Evgeny, 650, 651
 Maslakov Alexey, 259, 260, 585, 586
 Matyshak George, 342, 343, 707, 708
 Matyshak Georgy, 709, 710
 Mauclet Elisabeth, 346, 347, 780, 781
 Maximov Georgi, 761, 762
 Mccoll Samuel, 505, 506
 Mckee Alex, 523, 524
 Mclaughlin Jim, 701, 702
 Mcwade Taylor, 587, 588
 Melchert Jan, 370, 371
 Melnichuk Evgeniy, 577, 578
 Melnikov Vladimir, 122, 123, 142, 143, 673, 674
 Melyutin Mark, 819, 820
 Menzel Lucas, 982, 983
 Mercier Denis, 794, 795
 Merlone Andrea, 527, 528, 831, 832
 Meteleva Maria, 277, 278
 Metzger Stefan, 63, 64, 441, 442
 Meyer Hanno, 656, 657, 664, 665
 Meyer Matthias, 944, 945
 Meynier Simon, 845, 846, 853, 854
 Michaelis Rune, 671, 672
 Migoń Piotr, 810, 811
 Milanovskiy Svet, 184, 185
 Miller Holly, 1002, 1003
 Minayeva Tatiana, 705, 706
 Ming Feng, 422, 423
 Mingyi Zhang, 219, 220
 Minions Christina, 609, 610
 Minsley Burke, 445, 896, 897
 Misaylov Ivan, 623, 624
 Mithan Huw, 69, 70
 Miyazaki Shin, 281, 282
 Modin Igor, 894, 895, 916, 917
 Modzel Piotr, 810, 811
 Moine Olivier, 113–115
 Molina Antonio, 597, 598
 Mollaret Coline, 466, 467, 888, 889, 898, 899,
 966, 967, 984, 985
 Mollenhauer Gesine, 329, 330
 Molson John, 420, 421, 426, 427, 1012, 1013
 Mommertz Richard, 58, 59
 Monhonval Arthur, 346, 347, 780, 781
 Monteiro Santos Fernando, 875–877
 Moore Tim, 699, 700
 Moorman Brian, 806, 807
 Mora Carla, 662, 663
 Morard Sarah, 888, 889
 Morgenstern Anne, 344, 345, 360, 361, 533, 534
 Morin Samuel, 857, 858
 Morin Thomas, 857, 858
 Morino Costanza, 509, 510, 525, 526, 535, 536
 Morozova Aleksandra, 140, 141
 Morra Di Cella Umberto, 940, 941
 Morse Peter, 81, 82, 587, 588
 Mortara Gianni, 537, 538
 Moskalenko Fiodor, 986, 987
 Moskovchenko Mikhail, 71, 72
 Motenko Rimma, 97, 98
 Motta Elena, 940, 941
 Mourey Jacques, 934, 935
 Mueller Carsten, 301, 302, 350, 351
 Muir Derik, 348, 349
 Mullanurov Damir, 551, 552
 Munkhjargal Munkhdavaa, 982, 983
 Murton Julian, 664, 665
 Musacchio Chiara, 527, 528, 831, 832
 Muschitiello Francesco, 654, 655
 Muskett Reginald, 54, 55, 73, 74, 559, 560, 603,
 604
 Muster Sina, 63–66, 249, 250
 Myhra Kristin, 926–929
 Myhra Kristin Sæterdal, 936, 937
 Mylnikov Alexander, 358, 359
 Myshkovski Sergey, 186
 Nývlt Daniel, 301, 302, 519, 520, 670
 Nadeau Patrick, 1032, 1033
 Naidenko Aleksandra, 251, 252
 Natali Susan, 609, 610, 821, 822
 Nazarov Alexander, 187, 188
 Neefjes Annabelle, 589, 590
 Nekrasov Dmitry, 658, 659
 Nekrasova Olga, 633, 634

Nelson Frederick, 297, 298, 529–532, 607, 608
 Nesterova Nataliia, 1034, 1035
 Nicolsky Dmitry, 559, 560, 603, 604, 766, 767, 782, 783
 Nielsen Lars, 802, 803
 Nielsen Steffen, 406, 407
 Nieto Ana, 83, 84
 Nieuwendam Alexandre, 660, 661
 Niggli Laura, 966, 967
 Nigrelli Guido, 527, 528, 938, 939
 Nitzbon Jan, 249, 250, 299, 300, 305, 306
 Nitze Ingmar, 56, 57, 65, 66, 487, 488, 495, 496, 569, 570, 774, 775
 Niu Fujun, 189, 190
 Noetzli Jeannette, 462, 463, 611, 612
 Nofre Jordi, 662, 663
 Norén Gabriel, 370, 371
 Notarnicola Claudia, 382, 383
 Novikov Oleg, 277, 278
 Novikova Anna, 37, 790–793, 808, 809
 Nybo Marte, 191, 192
 Nyland Kelsey, 297, 298, 529–532
 Nyssen Jan, 511, 512

 O'donnell Jonathan, 317, 318
 O'neill Tanya, 553, 554
 O'regan Matt, 654, 655
 Oberle Ferdinand, 75, 76
 Oblogov Gleb, 109, 110, 812, 813
 Obu Jaroslav, 91, 92, 591, 592
 Ochiai Ryo, 152, 153
 Oedegaard Rune Strand, 460, 461, 464, 465
 Ogawa Masaya, 152, 153
 Ogneva Olga, 707, 708
 Ogorodov Stanislav, 37, 193, 194, 792, 793, 808, 809
 Ohno Hiroshi, 54, 55
 Ojha Csp, 996, 997
 Olefeldt David, 309, 310, 721, 722
 Olenchenko Vladimir, 884, 885
 Oliva Marc, 635, 636, 641, 642, 652, 653, 662, 663, 670
 Omelon Christopher, 105, 106
 Onaca Alexandru, 593, 594, 863, 864
 Opel Thomas, 656, 657, 664–667
 Opfergelt Sophie, 333, 334, 346, 347, 780, 781
 Orgogozo Laurent, 435, 436
 Orlov Timofey, 489, 490
 Orwin John, 1004
 Ospennikov Evgeniy, 97, 98
 Ostashov Andrey, 1034, 1035
 Overbeck Jacquelyn, 796, 797
 Overduin Paul, 344, 345, 521, 522, 579, 580, 761, 762, 890, 891
 Overduin Pier, 341, 763

 Pérez Augusto, 641, 642
 Pérez-Alberti Augusto, 662, 663
 Pablo Miguel, 875–877
 Packalen Maara, 701, 702
 Paillex Nicolas, 380, 381
 Painter Scott, 717, 718
 Palacios David, 662, 663
 Palazzo Francesco, 52, 53
 Palma Pedro, 635, 636, 652, 653
 Palmtag Juri, 333, 334
 Pan Baolin, 111, 112
 Pan Yue, 855, 856
 Panchenko Evgeny, 162, 163
 Panda Santosh, 559, 560, 745, 746
 Pandya Santosh, 603, 604
 Panteleev Ivan, 195, 196
 Papenmeier Svenja, 671, 672
 Paquette Michel, 829, 830
 Paranunzio Roberta, 938, 939
 Parmentier Frans-Jan W., 691, 692
 Paro Luca, 831, 832, 940, 941
 Pascale Roy-Léveillée, 701, 702
 Pastick Neal, 896, 897
 Pastukhov Alexander, 577, 578
 Pautler Brent, 105, 106
 Pawłowski lukasz, 810, 811
 Paz Maria Catarina, 875–877
 Pedersen Gro, 535, 536
 Pei Wansheng, 229, 230
 Pelayo Marta, 83, 84
 Pellet Cécile, 466, 467, 888, 889, 984, 985
 Pendin Vadim, 142, 143
 Peng Yunfeng, 721, 722
 Pereira Benoit, 346, 347
 Pereira Paulo, 635, 636, 652, 653
 Peter Maria, 91, 92
 Peterse Francien, 776, 777
 Peterson John, 1016, 1017
 Petrov Dmitriy, 342, 343
 Petrov Dmitriy, 709, 710
 Petrunin Aleksey, 184, 185
 Petrzhih Nataliia, 342, 343, 709, 710
 Pfalz Gregor, 329, 330
 Pfeiler Stefan, 906, 907
 Philippe Schoeneich, 845, 846
 Phillips Marcia, 404, 405, 462, 463, 962, 963
 Pienkowski Anna, 105, 106
 Piilo Sanna, 711, 712, 719, 720

Pinay Gilles, 317, 318
 Pindo Massimo, 1038, 1039
 Pino Catalina, 402, 403
 Piqueux Sylvain, 733, 734
 Pisabarro Alfonso, 992, 993
 Pläsken Regina, 833, 834
 Plekhov Oleg, 195, 196, 835, 836
 Podchasov Oleg, 205, 206
 Pogliotti Paolo, 940, 941
 Pohl Eric, 493, 494, 595, 596, 900, 901
 Pokrovsky Oleg, 435, 436
 Pollard Wayne, 541, 542, 668, 669
 Pommerol Antoine, 735, 736
 Ponomareva Olga, 565, 566
 Pope Michael, 348, 349
 Porter Trevor, 666, 667
 Potapova Olga, 650, 651
 Prantl Hannah, 77, 78
 Prater Isabel, 301, 302, 350, 351
 Pravkin Sergey, 671, 672
 Prokopyuk Igor, 819, 820
 Prokushkin Anatoly, 362, 363, 435, 436
 Protopopov Albert, 650, 651
 Prud'homme Charlotte, 113–115
 Pruessner Luisa, 404, 405
 Psenner Roland, 643–646
 Pugin Aleksei, 835, 836
 Puglini Matteo, 764, 765

 Qi Youzheng, 871, 872
 Qihao Yu, 855, 856
 Queen Clayton, 529–532
 Quintard Michel, 435, 436
 Quinton William, 265, 266, 699, 700, 1014, 1015,
 1036, 1037
 Quinton William. L., 1018, 1019

 Raab Sandra, 352, 353
 Rabatel Antoine, 934, 935
 Rachlewicz Grzegorz, 810, 811
 Radosavljevic Boris, 354, 355
 Ramage Justine, 533, 534
 Ramanouski Yury, 150, 151, 186, 197, 198
 Ramos Miguel, 597, 598, 875–877
 Ramos Sara, 599, 600
 Ramsden Guy, 466, 467
 Ran Youhua, 601, 602
 Ravanel Ludovic, 871, 872, 934, 935, 940, 941,
 958, 959
 Rebeix Romain, 118, 119
 Rethemeyer Janet, 344, 345, 370, 371, 679, 680,
 786, 787

 Revil Andre, 871, 872
 Rey David, 896, 897
 Ribeyre Charles, 406, 407
 Ribolini Adriano, 662, 663
 Richmond Bruce, 75, 76, 798, 799
 Rick Brianna, 392, 393, 529, 530, 837, 838
 Rico Ibai, 992, 993
 Riedel Thorsten, 329, 330
 Rieksts Karlis, 437, 438, 859, 860
 Risk Dave, 693, 694
 Ritter Ursula, 952, 953
 Rivkina Elizaveta, 287, 288, 495, 496
 Robert Yves, 1016, 1017
 Robson Benjamin, 176, 177
 Rodehacke Christian, 766, 767
 Rogora Michela, 1038, 1039
 Rogov Victor, 675, 676, 778, 779
 Roloff Victoria, 735, 736
 Roman Matěj, 670
 Romanenko Fedor, 861, 862
 Romanovsky Vladimir, 142, 143, 221, 222, 487,
 488, 557–560, 603, 604, 766, 767, 782,
 783, 821, 822, 1016, 1017
 Rotem Dotan, 356, 357
 Roth Gabriel, 952, 953
 Rouyet Line, 79, 80, 414, 415
 Roy Cameron, 668, 669
 Roy Louis-Philippe, 138, 139, 751–754
 Roy-Leveillee Pascale, 491, 492
 Rudaya Natalia, 629, 630, 650, 651
 Rudy Ashley, 81, 82, 339, 340, 829, 830
 Ruiz Jesus, 641, 642
 Ruiz Pereira Sebastián, 255, 256
 Ruiz Sebastian, 253, 254, 986, 987
 Ruiz-Fernández Jesus, 652, 653, 662, 663, 670
 Ryzhova Irina, 342, 343

 Séjourné Antoine, 474, 475, 493, 494, 545, 546,
 595, 596, 725, 726, 731, 732, 900, 901
 Sîrbu Flavius, 593, 594
 Sæmundsson Þorsteinn, 509, 510, 525, 526, 535,
 536
 Sachs Torsten, 63, 64, 366, 367, 441, 442, 691,
 692
 Sadurtdinov Marat, 583, 584, 613, 614, 902, 903
 Sailer Rudolf, 77, 78, 388, 389
 Saintenoy Albane, 595, 596, 900, 901
 Saito Kazuyuki, 54, 55, 116, 117
 Saltel Marc, 118, 119
 Salvatore Maria Cristina, 408, 409
 Sander Lasse, 671, 672
 Sanders Tina, 784, 785

Sanna Francesca, 831, 832
 Sannel Britta, 713, 714, 717, 718
 Sansoulet Julie, 743, 744
 Sarıkaya M. Akif, 662, 663
 Sasaki Yuutarou, 231, 232
 Savikko Brenton, 211, 212
 Sawada Yuki, 245, 246
 Schäfer-Neth Christian, 65, 66
 Schöner Wolfgang, 978, 979
 Schaedel Christina, 88, 303, 304
 Schauer Linus, 352, 353
 Scheibz Jürgen, 882, 883
 Scherler Dirk, 988, 989
 Scherler Martin, 466, 467, 990, 991
 Schirrmeister Lutz, 780, 781, 784, 785
 Schmid Thomas, 83, 84
 Schneider Von Deimling Thomas, 58, 59, 305, 306, 521, 522, 763, 784, 785
 Schneiderbauer Stefan, 398, 399
 Schoeneich Philippe, 406, 407, 857, 858, 932, 933
 Schröder Tanja, 904, 905
 Schrott Lothar, 384, 385, 886, 887
 Schuur Ted, 88
 Schwalbe Ellen, 384, 385
 Scibilia Elena, 437, 438, 859, 860
 Scorpio Vittoria, 501, 502
 Scott Neal, 368, 369
 Scotti Ricardo, 120, 121, 388, 389
 Scotti Riccardo, 392, 393
 Sedov Sergey, 122, 123
 Sefilian Anna, 342, 343, 715, 716
 Semiletov Igor, 654, 655, 770, 771
 Semin Mikhail, 439, 440
 Senn Johannes, 507, 508
 Seppi Roberto, 382, 383, 408, 409, 1038, 1039
 Sepulveda-Jauregui Armando, 695, 696
 Serafimovich Andrei, 63, 64, 441, 442
 Sergeev Dmitrii, 605, 606
 Sergeev Dmitry, 168, 169, 247, 248
 Sergeeva Daria, 480, 481
 Serikov Sergey, 623, 624
 Serrano Charlie, 932, 933
 Serrano Enrique, 662, 663, 992, 993
 Seybold Cathy, 553, 554
 Shabanova Natalia, 792, 793, 861, 862
 Shakhova Natalia, 768–771
 Shakil Sarah, 317, 318, 339, 340, 364, 365
 Sharkov Aleksey, 819, 820
 Shatilla Nadine, 1010, 1011
 Shatilovich Anastasia, 358, 359
 Sheinkman Vladimir, 122, 123, 673, 674
 Shestakova Alyona, 199, 200
 Shesternev Dmitrii, 201, 202
 Shevnin Vladimir, 894, 895, 916, 917
 Shikhov Andrey, 1034, 1035
 Shiklomanov Nikolay, 209, 210, 243, 244, 577, 578, 607, 608, 837, 838
 Shilovtseva Olga, 861, 862
 Shiratori Ryoko, 203, 204
 Shuangyang Li, 219, 220
 Shur Yuri, 637, 638, 647–649
 Shurpali Narasinha, 691, 692
 Sibiryakova Aleksandra, 205, 206
 Siegwart Collier Laura, 291, 292
 Sigsgaard Charlotte, 802, 803
 Silvestri Paolo, 527, 528
 Simpson Myrna, 105, 106
 Sinitsky Anton, 573, 574
 Sinitsyn Anatoly, 839, 840
 Sirbu Flavius, 863, 864
 Sirin Andrey, 705, 706
 Sjöberg Ylva, 717, 718, 749, 750
 Sköld Martin, 654, 655
 Skobelev Aleksey, 894, 895, 916, 917
 Skorospekhova Tatyana, 344, 345
 Skvortsov Andrei, 613, 614
 Skvortsov Andrey, 583, 584, 902, 903
 Slogoda Elena, 289, 290, 677, 678
 Sliger Michel, 637, 638
 Smith Sharon, 581, 582
 Smolikova Jana, 878, 879
 Sobiech-Wolf Jennifer, 89, 90
 Sokolov Ivan, 215, 216
 Sone Toshio, 245, 246
 Sonnentag Oliver, 699, 700
 Sonyushkin Anton, 61, 62
 Soueid-Ahmed Abdellahi, 871, 872
 Spehs Thomas, 705, 706
 Spektor Valentin, 609, 610
 Spektor Vladimir, 199, 200
 Spencer Rob, 317, 318
 Springman Sarah, 462, 463
 St. Louis Vincent, 364, 365
 St. Pierre Kyra, 364, 365
 Stötter Johann, 77, 78
 Stanilovskaya Julia, 168, 169, 245, 246
 Stanilovskaya Yulia, 174, 175, 480, 481
 Stark Lena, 124, 125
 Staub Benno, 611, 612
 Steger Stefan, 398, 399
 Steiner Matthias, 906, 907, 978, 979
 Stendel Martin, 766, 767
 Stephani Eva, 207, 208

Stevens Christopher, 806, 807
 Stillman David, 908, 909
 Stocker-Mittaz Catherine, 466, 467
 Stolpmann Lydia, 344, 345, 360, 361
 Stoof-Leichsenring Kathleen, 360, 361
 Strand Sarah, 468, 469
 Strauss Jens, 346, 347, 485, 486, 637, 638, 761, 762, 774–777, 780, 781, 784, 785
 Strel Alexandra, 48, 49
 Streletskaya Irina, 109, 110, 126, 127, 257, 258, 325, 326, 658, 659, 675, 676, 812, 813
 Streletskiy Dmitriy, 243, 244, 567, 568
 Streletskiy Dmitry, 209, 210, 607, 608
 Strozzi Tazio, 85, 86, 380, 381, 386, 387
 Strzelecki Mateusz, 810, 811
 Stuefer Svetlana, 1026, 1027
 Stumm Dorothea, 996, 997
 Su Zhongbo, 446, 447
 Sudakova Maria, 613, 614, 902, 903
 Sultenfuls Jurgen, 356, 357
 Sun Binxiang, 443, 444
 Sun Tiecheng, 227, 228
 Sun Wenbin, 968, 969
 Sun Youhong, 827, 828
 Sun Zhizhong, 236, 237
 Surikov Vitaly, 178, 179
 Suter Luis, 209, 210, 243, 244
 Suvorov Gennady, 705, 706
 Svitoch Aleksandr, 107, 108
 Swarzenski Peter, 75, 76
 Swenson Sean, 273, 274
 Swirad Zuzanna, 731, 732, 810, 811
 Sysoyev Mikhail, 827, 828
 Szuman Izabela, 101, 102

 Tábořík Petr, 575, 576
 Takadema Hideyuki, 392, 393
 Talalay Pavel, 827, 828
 Tamburini Andrea, 537, 538
 Tananaev Nikita, 362, 363, 695, 696
 Tanarro Luis M., 470, 471
 Tang Weigang, 1010, 1011
 Tank Suzanne, 317, 318, 339, 340, 364, 365
 Tanski George, 329, 330, 335, 336, 366, 367
 Tape Ken, 56, 57
 Tapia Carla, 255, 256, 886, 887, 994, 995
 Taratunina Natalia, 675, 676
 Tarbeeva Anna, 307, 308
 Tarkhov Matvey, 342, 343
 Teisserenc Roman, 362, 363, 695, 696
 Teshebaeva Kanayim, 87
 Tesi Tommaso, 654, 655, 770, 771

 Tessadri Richard, 643–646
 Textor Sadie, 317, 318
 Thalasso Frederic, 695, 696
 Thayyen Renoj, 996, 997
 The 'frozen-Ground Cartoons' Team And, 743, 744
 Theresa Henning, 285, 286
 Therrien René, 420, 421, 1012, 1013
 Thibert Emmanuel, 615, 616
 Thiel Christian, 38, 39
 Thiel Gillian, 368, 369
 Thomas Bertrand, 118, 119
 Thomas Nicolas, 735, 736
 Thornley John, 211, 212
 Tikhonravova Yana, 289, 290, 677, 678
 Timofeeva Marija, 342, 343
 Tobler Daniel, 942, 943, 952, 953
 Tolmanov Vasily, 160, 161, 213, 214, 243, 244, 259, 260, 285, 286, 567, 568
 Tolotti Monica, 1008, 1009, 1020, 1021, 1038, 1039
 Tomaškovičová Soňa, 156, 157
 Tomaskovicova Sonia, 910, 911
 Tomczyk Aleksandra, 101, 102, 539, 540
 Toninandel David, 388, 389
 Torgovkin Yaroslav, 199, 200
 Tran Anh Phuong, 1016, 1017
 Trant Andrew, 291, 292
 Trapeznikova Olga, 489, 490
 Tregubov Oleg, 585, 586
 Trochim Erin, 88
 Troilo Fabrizio, 410, 411, 940, 941
 Trombotto Dario, 384, 385, 392, 393
 Trombotto Liaudat Dario, 255, 256, 994, 995
 Trouvé Emmanuel, 980, 981
 Tsarapov Michail, 174, 175
 Tsarev Andrey, 583, 584, 613, 614, 902, 903
 Tsibizov Leonid, 912, 913
 Tsogt-Erdene Gansukh, 705, 706
 Tumskoy Vladimir, 770, 771
 Tunnicliffe Jon, 339, 340
 Turconi Laura, 938, 939
 Turetsky Merritt, 309, 310

 Uchaev Anton, 633, 634
 Uchida Masao, 54, 55
 Ullmann Tobias, 89, 90
 Ulrich Craig, 1016, 1017
 Ulrich Mathias, 569, 570
 Undrakhtsetseg Tsogtbaatar, 705, 706
 Urdea Petru, 593, 594, 662, 663, 863, 864, 976, 977

Uxa Tomáš, 103, 104, 128, 129
 Väiliranta Minna, 711, 712, 719, 720
 Valcárcel Marcos, 662, 663
 Van Der Ploeg Martine, 448, 449
 Van Der Sluijs Jurjen, 81, 82, 339, 340
 Van Geldern Robert, 1012, 1013
 Van Huissteden Jacobus, 287, 288, 691, 692
 Van Soest Maud, 372, 373
 Van Winden Elise, 448, 449
 Vandeuren Aubry, 346, 347
 Vasil'chuk Alla, 130–133
 Vasil'chuk Jessica, 130–133
 Vasil'chuk Yuriy, 130–133, 689, 690
 Vasiliev Alexander, 109, 110, 311, 312, 812, 813
 Velde Ype, 1026, 1027
 Velikin Sergei, 914, 915, 918, 919
 Velikin Sergey, 184, 185
 Veremeeva Alexandra, 495, 496
 Vergun Alexey, 755, 756, 808, 809
 Victorov Alexey, 489, 490, 497, 498
 Vieira Gonçalo, 597–600, 662, 663, 875–877
 Vieli Andreas, 390, 391, 462, 463, 944, 945
 Viers Jérôme, 435, 436
 Vignoli Gianluca, 501, 502
 Viitanen Leena-Kaisa, 341
 Vivero Sebastian, 392, 393, 400, 401, 412, 413
 Vlasov Alexander, 168, 169
 Vohradský Lukáš, 103, 104
 Voiculescu Mircea, 593, 594
 Volkov Nikolay, 215, 216
 Volkov-Bogorodsky Dmitry, 168, 169
 Vonder Mühl Daniel, 466, 467
 Vonk Jorien, 317, 318, 321, 322, 335, 336, 352, 353
 Vorobyev Sergey, 97, 98
 Voss Clifford, 445
 Voytenko Alina, 217, 218

 Wagner Anna, 825, 826, 841, 842
 Wagner Dirk, 277, 278, 366, 367
 Wagner Florian, 898, 899
 Wainstein Pablo, 1002, 1003
 Wainwright Haruko, 1016, 1017
 Walker Donald, 774, 775
 Walter Anthony Katey, 360, 361, 485, 486
 Walvoord Michelle, 445, 896, 897
 Wang Chong, 223, 224
 Wang Honglei, 236, 237
 Wang Rusheng, 827, 828
 Wang Tianliang, 227, 228
 Wang Xiaowen, 513, 514

 Wani John, 996, 997
 Wansheng Pei, 219, 220
 Ward Jones Melissa, 541, 542
 Waroszewski Jarosław, 575, 576
 Way Robert, 291, 292, 617, 618, 751, 752, 948, 949
 Weber Samuel, 930, 931, 944, 945
 Wee Julie, 543, 544
 Wegmüller Urs, 85, 86
 Wei Cao, 452, 453
 Wei Ma, 225, 226
 Wei Mingjian, 111, 112
 Weinstein Yishai, 356, 357
 Wen Zhi, 450, 451
 Westermann Sebastian, 91, 92, 176, 177, 299, 300, 458, 459, 521, 522, 591, 592, 683, 684, 693, 694, 704, 713, 714, 763, 950, 951, 974, 975
 Westoby Matt, 523, 524
 Wetterich Sebastian, 679, 680
 Wever Nander, 962, 963
 Whitaker Darroch, 291, 292
 Wickland Kimberly, 317, 318
 Wicky Jonas, 998, 999
 Widhalm Barbara, 42, 43
 Wieland Markus, 507, 508
 Wilcox Evan, 619, 620
 Wild Birgit, 654, 655, 770, 771
 Wiltshire Karen, 671, 672
 Winkel Matthias, 485, 486, 784, 785
 Winkler Stefan, 400, 401
 Winterberger Maria, 380, 381, 392, 393
 Wischhoefer Philipp, 370, 371, 786, 787
 Wolfe Stephen, 587, 588
 Wologo Ethan, 317, 318
 Wolter Juliane, 679, 680
 Wotte Anja, 370, 371, 786, 787
 Wuttig Frank, 207, 208
 Wylie Bruce, 896, 897

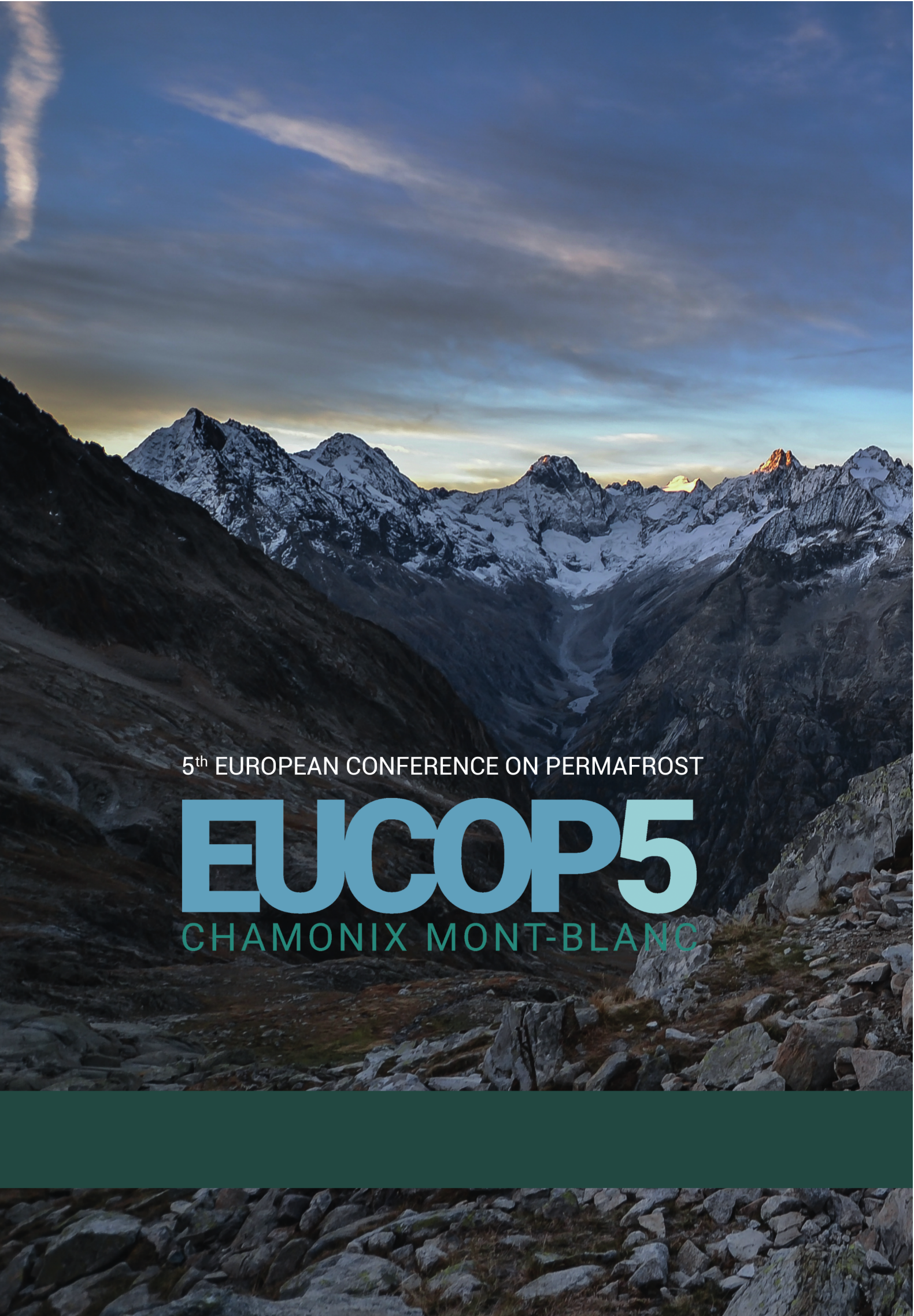
 Xiao Ming, 221, 222
 Xiaoying Hu, 452, 453
 Xinbing Wang, 855, 856
 Xiyan Zhang, 452, 453

 Yıldırım Cengiz, 662, 663
 Yadamsuren Gansukh, 136, 137, 982, 983
 Yaghoobi Tabar Borhan, 875–877
 Yakimov Artem, 918, 919
 Yaling Chou, 452, 453
 Yamkhin Jambaljav, 136, 137
 Yamkin Jambaljav, 982, 983

Yan Zhongrui, 229, 230
 Yang Guibiao, 721, 722
 Yang Kun, 571, 572
 Yang Yuanhe, 271, 272, 295, 296, 313, 314, 317,
 318, 721, 722
 Yanhu Mu, 225, 226, 855, 856
 Yanina Tamara, 675, 676
 Yechieli Yoseph, 356, 357
 Yi Yonghong, 571, 572
 Yin Guoan, 189, 190
 Yin Zhenhua, 238
 Yingbing Huang, 219, 220
 Yingsheng Dang, 235
 Yokohata Tokuta, 54, 55
 Yoldi Zurine, 735, 736
 Yongzhi Liu, 225, 226
 Yoshikawa Kenji, 245, 246, 261, 262, 757, 758
 You Zhemin, 223, 224
 Yu Lianyu, 446, 447
 Yu Sheng, 452, 453, 589, 590
 Yu Wenbing, 621, 622
 Yue Zurun, 227, 228
 Yurov Fyodor, 259, 260

 Zadorozhnaia Nataliia, 812, 813
 Zadorozhnaya Natalia, 109, 110
 Zamolodchikov Dmitrii, 287, 288
 Zamolodchikov Dmitry, 585, 586
 Zanoner Thomas, 408, 409
 Zarnetske Jay, 317, 318, 327, 328
 Zebisch Marc, 398, 399
 Zeng Yijian, 446, 447
 Zerkal Evgeny, 894, 895, 916, 917
 Zhang Hui, 711, 712, 719, 720
 Zhang Mingli, 450, 451
 Zhang Mingyi, 229, 230, 431–434
 Zhang Rudolf, 918, 919
 Zhang Shujuan, 236, 237
 Zhang Wenjiang, 571, 572
 Zhang Xiyin, 433, 434
 Zheleznyak Mikhail, 623, 624
 Zhelnin Maxim, 439, 440
 Zheng Hao, 152, 153, 164, 165, 203, 204, 231,
 232
 Zhirkov Aleksandr, 623, 624
 Zhou Jiazuo, 422, 423
 Zimin Mikhail, 61, 62
 Zimmerman Christian, 56, 57
 Zimov Nikita, 321, 322
 Zolkos Scott, 317, 318, 339, 340, 364, 365, 751,
 752
 Zona Donatella, 441, 442

 Zoor Lena, 350, 351
 Zubrzycki Sebastian, 350, 351, 784, 785
 Zucca Francesco, 382, 383
 Zumiani Matteo, 408, 409
 Zverev Andrey, 489, 490
 Zwanenburg Natalie, 309, 310
 Zwieback Simon, 521, 522
 Zwinger Thomas, 99, 100



5th EUROPEAN CONFERENCE ON PERMAFROST

EUCOP5

CHAMONIX MONT-BLANC